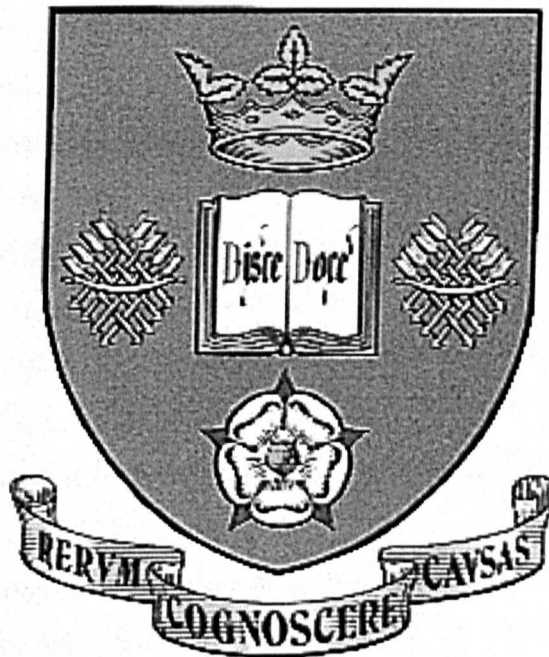


# **Effect of Changes in Pipe Direction across Surcharged Manholes on Dispersion and Head Loss**



**Chanwit Saiyudthong**

**Thesis submitted in partial fulfilment of the requirements for the  
Degree of Doctor of Philosophy**

**University of Sheffield**

**Department of Civil and Structural Engineering**

**August 2003**

# IMAGING SERVICES NORTH

Boston Spa, Wetherby  
West Yorkshire, LS23 7BQ  
[www.bl.uk](http://www.bl.uk)

# THESIS CONTAINS

# CD

## ABSTRACT

From the water quality perspective, looking at a sewer system as a reactor whose effluent should be regulated in terms of water quality, solute tracer studies need to be undertaken to define the retention and spread of temporally varying concentrations. Focussing on a manhole, its aspects such as shape, ratio of pipe and manhole diameter, and pipe direction all affect the transport of the solute through the sewer system.

The aim of this study is to quantify the magnitude and changes in dispersive fraction ( $\gamma$ ) used in the ADZ technique, and head loss coefficient ( $K$ ) due to changes in pipe direction across a manhole. Under surcharge conditions, solute transport along plane angles such as  $0^\circ$ ,  $30^\circ$ ,  $60^\circ$  and  $90^\circ$ , of an inlet and an outlet pipes with/without benching was investigated for a range of surcharge and discharge. Additionally, the head losses due to such an angle were also measured. From data analysis, both the dispersive fraction and the head loss coefficient were properties of each plane angle. For example, at the angle of  $30^\circ$ -unbenched, the dispersive fraction was constant at approximately 0.7 and the head loss coefficient was constant at about 2.22.

Moreover, these comprehensive processed data were beneficial to basic knowledge of solute mixing. First, the square root of the ratio of head loss and residence time, represented by energy dissipation, was found to be linear to flow rate. Hence, it might be used as a conversion of a head loss to residence time. Second, two cell ADZ technique was developed to enhance the travel time prediction of a downstream concentration profile. The two cell technique was able to predict the concentration profile very well, but due to difficulty in application, a single cell ADZ technique was more useful in general.

## “Education is growth”

This thesis was dedicated to my mother, who planted an educational seed in me.



## **Acknowledgements**

Without the kindness of these people, the PhD thesis could not be finished. I would like to thank Dr Ian Guymer, who has not only supervised my PhD, but also taught me some of the English language. Besides, I really appreciate all the help from my colleagues in Room D106 as well as I am so appreciative of every thing, technicians in the Department of Civil and Structural Engineering did for me.

I am deeply grateful to my parents, brothers and sisters, who support me in many ways while I live in the UK. Finally, I would like to say “Thank you very much” to my lovely wife, who has been my friend along the PhD study.

Chanwit Saiyudthong

---

**Contents**

Abstract	i
Dedication	ii
Acknowledgement	iii
Contents	iv
List of figures	vii
List of tables	xi
Notation	xii
1 Introduction	1
1.1 Background	1
1.2 Regulations	2
1.3 Aims of thesis	4
1.4 Contents of thesis	6
2 Literature review	8
2.1 Sewer system	8
2.1.1 Flow design	9
2.1.2 Flow equation	9
2.1.3 Flow routing in surcharge conditions	12
2.2 Sewer network and Real Time Control (RTC)	14
2.3 Sewer tracing studies	15
2.4 Manholes	17
2.5 Estimation of head loss due to a manhole	18
2.6 Coefficient of head losses	19
2.7 Solute dispersion	26
2.7.1 Advection	28
2.7.2 Fick's first and second laws for molecular diffusion	28
2.7.3 Molecular diffusion in fluid movement	31
2.7.4 Solute transport in one-dimensional turbulent flow	32
2.8 Advection Dispersion Equation (ADE)	34
2.9 Aggregated Dead Zone (ADZ)	38

---

2.10 Parameter estimation/optimisation	46
2.11 Previous work on longitudinal dispersion and its relationships	49
2.12 Reactor mixing	53
2.13 Computational Fluid Dynamics (CFD)	54
2.13.1 Governing equations	54
2.13.2 Turbulence models	56
2.13.3 Previous work	56
2.14 Summary	59
3 Experimental work	61
3.1 Manhole configurations	62
3.2 Fluorometers	64
3.3 30° V-notch weir	67
3.4 Water level follower	68
3.5 Manometers	69
3.6 Data collection	69
3.7 Data analysis	73
3.7.1 Head loss coefficient	73
3.7.2 ADE/ADZ analysis	74
4 Experimental results	76
4.1 Models to analyse data	77
4.2 Head losses	79
4.3 Travel time	83
4.4 Reach time delay	86
4.5 Residence time	89
4.6 Dispersive fraction	89
5 CFD simulation	93
5.1 Simulated energy losses	94
5.1.1 Pre-processing	94
5.1.2 Solving	96
5.1.3 Post-processing	97
5.2 Conclusion	100

---

6 Discussion	102
6.1 Head loss coefficient	102
6.1.1 Influence of benching	102
6.1.2 Influence of changes in plane angle	103
6.1.3 Comparison of head loss coefficient to previous work	104
6.1.4 Comparison between experiment and CFD simulation	107
6.2 Travel time	109
6.2.1 Predictive equation using threshold surcharge	109
6.2.2 Predictive equation using multiple regression	119
6.3 Dispersive fraction	121
6.4 Energy dissipation	124
6.5 Cells in ADZ model	126
6.5.1 Two-cell technique	130
6.5.2 Cells in series technique	137
6.5.3 Results from analysis	140
6.5.4 Conclusions for two-cell ADZ technique	144
7 Future work	145
7.1 Multiple inlets	145
7.2 Universal equation for dispersion across manholes	145
7.3 Unsteady flow condition	146
7.4 Field velocity	146
8 Conclusions	147
References	150
Appendix A	CD-ROM

---

**List of Figures**

1.1 Typical sewer system consisting of sewer pipes, manhole, combined sewer overflow and wastewater treatment plant	2
2.1 Partial-full flow in a circular pipe	11
2.2 Transitions between free surface and surcharged flow	13
2.3 Concentration profiles from storm conditions	16
2.4 Concentration profiles from dry weather flow conditions	16
2.5 Typical manholes	17
2.6 Head loss due to a manhole	19
2.7 Submerged jet: Velocity distribution and Diffusion region	22
2.8 Coefficient of water depth, $C_2$	24
2.9 Benching types for floor configuration	27
2.10 Mass balance of the element	29
2.11 Solution of Fick's second law for an instantaneous plane source	31
2.12 Average and fluctuating velocities	32
2.13 ADE routing of several slugs	35
2.14 Influence of advection on the time delay at the onset of the outlet profile of two ideal reactors	38
2.15 Solute mass balance for ADZ	39
2.16 Block diagram of first order transfer function	41
2.17 Serial and parallel connection of first order transfer function models	42
2.18 Block diagram of transfer function decomposition	44
2.19 Residence time for quick and slow flow	45
2.20 Simulated profile, decomposed quick flow and slow flow, and compared to observed profile	45
2.21 Predicted downstream profiles from ADE and ADZ standard from the 60°-unbenched manhole at 2 l/s flow rate and 176 mm surcharge	47
2.22 Predicted downstream profiles from the 60°-unbenched manhole at 2 l/s flow rate and 176 mm surcharge	50
2.23 Relationships between dispersive fraction and head loss coefficient	53

---

2.24 Dispersive fraction describing partial mixing with reference to two theoretical reactors	55
2.25 Plan of pond configurations	57
2.26 Simulated and observed RTD curves	58
2.27 Parameter layout of an around-the end hydraulic flocculator	59
3.1 Laboratory apparatus	62
3.2 Benched manhole configurations	63
3.3 Water level follower to measure surcharge	64
3.4 Fluorometer and adapter	65
3.5 Calibration for upstream and downstream fluorometers	67
3.6 Linear calibration for water level follower	69
3.7 Manometer and point gauge	70
3.8 Comparison on $R_t^2$ of observed manometers for an inlet/outlet pipe	71
3.9 Base line generated from two mean points of 30 s from the onset and end of concentration profile	74
4.1 Concept for reach time delay and travel time	76
4.2 Predicted downstream profiles	78
4.3 $R_t^2$ from ADE and ADZ optimised for the 30°-unbenched manhole	78
4.4 Head loss coefficient (K) against surcharge from benched manholes	80
4.5 Head loss coefficient (K) against surcharge from unbenched manholes	81
4.6 Head loss and head loss coefficient (K)	82
4.7 Travel time from benched manholes	84
4.8 Travel time from unbenched manholes	85
4.9 Reach time delay from benched manholes	87
4.10 Reach time delay from unbenched manholes	88
4.11 Residence time from benched manholes	90
4.12 Residence time from unbenched manholes	91
4.13 Dispersive fraction over surcharge	92
5.1 Meshed model and mesh quality before CFD simulation for the 60°-unbenched with 400 mm surcharge	95
5.2 Convergence of residuals at approximately 1600 iterations	97

---

5.3 Plan of velocity contour along the pipe centre	98
5.4 Velocity contour at front view along the inlet pipe centre	99
5.5 Using a range of a pressure profile to determine the energy loss of the 90°-unbenched manhole with 400 mm surcharge	99
6.1 Observed head loss coefficient based on the plane angles	104
6.2 Coefficient ( $C_3$ and $C_4$ )	105
6.3 Comparison of the head loss coefficient from Young's equations and from the experiment	106
6.4 Comparison of the head loss coefficient from CFD simulation and measurement	108
6.5 Threshold surcharge at approximately 275 mm within the transient zone of the travel time for the 30°-unbenched manhole	110
6.6 Threshold surcharge at approximately 325 mm within the transient zone of the travel time for the 60°-unbenched manhole	110
6.7 Linear relationship between travel time and pre-threshold surcharge of the 60°-unbenched manhole	111
6.8 Correlation between values of the slope and reciprocal flow rate	112
6.9 Correlation between value of the y-intercept and reciprocal flow rate	112
6.10 Comparison between observed travel time from ADZ optimised and predicted travel time from Equation 6.1	113
6.11 For post-threshold surcharge, travel time related to reciprocal flow rate	114
6.12 Longer core zone than manhole diameter	116
6.13 Prediction of travel time for pre-and post-threshold surcharge, in which the threshold is at 0.325 m for the 60°-unbenched manhole	117
6.14 Average flow velocity ( $V$ ) in 0.088 m diameter pipe with distance of 2.7 m	118
6.15 Trend lines from the co-ordinate of reciprocal flow rate and average travel time	118
6.16 $R^2$ of observed travel time against estimated travel time	122
6.17 Provision of benching for circular flow in a manhole	123
6.18 Linear relationships of average energy dissipation and flow rate	126
6.19 Prediction of downstream profile by a single cell ADZ optimised	127
6.20 Relationship between surcharge and $R_t^2$ using an optimised single cell ADZ for the 90°-unbenched manhole	128

---

6.21 Various shapes of downstream concentration profiles	129
6.22 Peak factor to obtain the best parameters of “a” and “b” for Head profile’s prediction	131
6.23 Flowchart of generating Head profile	132
6.24 The best Peak factor obtaining the greatest $R_t^2$ for Head profile	134
6.25 Flowchart of generating Tail profile	135
6.26 Comparison of observed downstream profile and the profile of 2 cells obtained from Head profile plus Tail profile	136
6.27 Comparison of prediction from 2 cells and single cell with observed downstream profile	136
6.28 The 6 <sup>th</sup> order provided the best $R_t^2$ for the Tail profile	138
6.29 The best model order, [6 1], for the prediction of the Tail profile, compared to the 5 <sup>th</sup> and 7 <sup>th</sup> order	138
6.30 Series of sixth-order block diagram	139
6.31 Re-circulation of tracer dye in a manhole	140
6.32 Tracer dye distribution, represented by red, through the 388 mm diameter manhole connected with 88 mm diameter pipe	141
6.33 Residence time form 2-cell technique of the 90°-benched manhole	142
6.34 Residence time from 2-cell technique of the 90°-unbenched manhole	143



---

**List of Tables**

1.1 River quality standards	3
1.2 Coliform bacteria in identified bathing waters	3
1.3 Standard for protecting amenity use	5
2.1 Summary results from tracer data	16
2.2 Relationship between diameter of outlet and chamber	18
2.3 Head loss coefficient	19
2.4 Estimated shape factor from measurements with $D_m/D$ up to 4	21
2.5 Correlation factor for benching	27
2.6 Predicted variation of dispersion parameters from manhole and pipe data	49
2.7 Averaged reach time delay and travel time for stepped manhole	52
2.8 RTD curves for geometry C	57
3.1 Error per mm for level gauge reading	68
3.2 Details of data collection	70
4.1 Surcharge mean and standard deviation of reach time delay	86
5.1 Simulated head loss coefficient	100
5.2 Head loss coefficient from simulation and measurement	101
6.1 Head loss coefficient (K)	103
6.2 Head loss coefficient calculated from the equation (Young et al, 1999)	106
6.3 Comparison of head loss coefficient calculated from Pedersen and Mark, and Young et al (1999)	107
6.4 Equations to predict travel time	114
6.5 Equations to predict travel time from linear function of reciprocal flow rate	119
6.6 Average and standard deviation of energy dissipation along surcharge	125
6.7 Linear equation and $R^2$ for the average energy dissipation against flow rate	125
6.8 Increase in $R_t^2$ by two cell ADZ	137

---

**Notation**

A	Cross section area of the flow
$A_w$	Area of watershed
c	Concentration of a solute substance
C	Instantaneous solute concentration
c'	Fluctuating solute concentration
$C_1$	Coefficient related to relative manhole size
$C_2$	Coefficient related to water depth in a manhole
$C_3$	Coefficient related to lateral flow, lateral angle and plunging flow
$C_4$	Coefficient relates to relative pipe direction
$C_d$	Coefficient of discharge for a weir
$C_r$	Runoff coefficient
D	Pipe diameter
d	Water depth in pipe diameter D
$D_L$	Longitudinal dispersion coefficient
$D_m$	Manhole diameter
$d_{mH}$	Water depth in a manhole
$D_o$	Outlet pipe diameter
$e_m$	Molecular diffusion coefficient
g	Acceleration due to gravity
G	Energy dissipation
$G_H$	Gain for Head profile
$G_T$	Gain for Tail profile
H	Overflow level for a weir
$h_f$	Frictional losses in pipe
$h_L$	Local minor loss
$HMC_i$	Horizontal moment check for pipe I
i	Rainfall intensity
$I_x$	Advective flux in the x direction
$J_m$	Molecular diffusive flux in the x direction
K	Head loss coefficient
k	Turbulent kinetic energy

---

$K_I$	Composite energy loss coefficient
$k_s$	Equivalent sand roughness
$L$	Pipe length
$M$	Tracer mass
$MF$	Mass balance factor
$n$	Coefficient of roughness
$Q_4$	Discharge into the manhole from the inlet
$Q$	Storm flow rate
$Q_1, Q_2, Q_3$	Pipe discharge in inflow pipes 1, 2 and 3, respectively
$Q_{fb}$	Full flow rate
$Q_l$	Lateral flow
$Q_o$	Total discharge in the outlet pipe
$R$	Hydraulic radius
$R_t^2$	Fitting parameter of an observed and predicted temporal downstream profile
$s$	Hydraulic gradient or invert slope
$S$	Surcharge level
$T$	Residence time
$t$	time or temperature
$Tbar$ or $\bar{t}$	Travel time
$U$	Mean velocity
$u'_x$	Fluctuating velocity
$U_x$	Instantaneous velocity
$u_x$	Velocity in the x direction
$V$	velocity
$y$	Water depth in a manhole
$y_k$	Dye concentration downstream
$Z_1, Z_2, Z_3$	Inlet elevation of inflow pipe 1, 2, and 3, respectively
$z^{-i}$	Z transfer function
$\Delta H$	Head losses
$\Delta t$	Time interval
$\varepsilon$	Turbulent energy dissipation rate
$\gamma$	Dispersive fraction

---

$\lambda$	Pipe friction factor
$\mu$	Dynamic viscosity of water
$\nu$	Kinematic viscosity
$\theta$	Plane angle of changes in pipe direction across a manhole
$\rho$	Density of water
$t$	Integration variable on the time axis
$\tau$	Reach time delay
$\omega$	Correlation factor to relative pipe diameter
$\psi$	Angle between the outlet main and an inflow pipe, measured clockwise from the outlet pipe
$\zeta$	Shape factor of a manhole

---

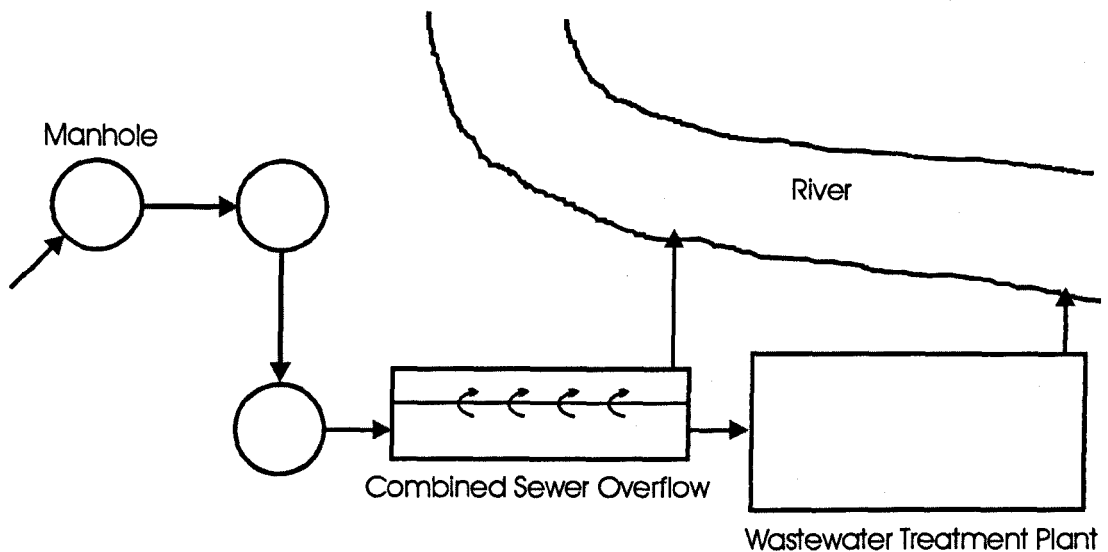
# Chapter 1

# Introduction

## 1.1 Background

The first management of urban drainage took place in England during the industrial revolution in the 19<sup>th</sup> century, according to Brombach (2002). Afterwards, this English development spread to the Continental Europe at the end of the century and around the world later. Originally, the drainage was only to remove the sewage or storm water from the city as fast as possible to the receiving water, without the concern about the quality or environmental problem of the receiving water. In urban drainage systems today, additional units are needed, such as a combined sewer overflow and water treatment plant, to spill the storm water directly to the receiving water and to treat the sewage before discharge, respectively. Figure 1.1 illustrates a typical combined sewer system consisting of sewer pipes, manholes, a combined sewer overflow and a wastewater treatment plant. This sophisticated system, of course, may have to be designed by engineers in order to gain an economical investment, i.e. the system is built with suitable size and saving energy consumption to operate the system.

Currently, engineers have several computational tools, i.e. sewer quantity and quality modelling packages, to design and operate urban drainage systems. Most of the packages just model “plug flow” or advection for mixing mechanism, or together with the longitudinal dispersion coefficient from Advection Dispersion Equation (ADE). However, at structures such as manholes, they assume that there are either no effects of mixing or complete mixing.



**Figure 1.1** Typical sewer system consisting of sewer pipes (straight arrows), manholes, combined sewer overflow and wastewater treatment plant

## 1.2 Regulations

Also, such a sewer system as shown in Figure 1.1 discharges wastewater to the receiving water in wet weather periods. The combined sewer overflow (CSO) will work as a unit to overflow some of the mixing of storm and sanitary flow in wet weather into the receiving water and to allow all dry weather flow (DWF) to the wastewater treatment plant before leaving the treated water to the river. Hence, these 2 point sources of contamination should have some regulations to protect the quality of the surroundings.

To sustain the surface water ecosystems in the United Kingdom, for example, several requirements of the receiving waters follow the concepts of Urban Pollution Management (Foundation for Water Research, 1998). It is issued as to manage sewer and sewage treatment work under wet weather conditions in a cost effective way. In general, the environmental standards for surface water are classified by uses of the water body into 3 main categories: river aquatic life, bathing and general amenity.

***River aquatic life***

For England and Wales, the criteria to define river use classes are based on the percentile of BOD, dissolved oxygen (DO), total ammonia and un-ionised ammonia. Such criteria are to protect the ecosystems, which receive continuous discharges, as illustrated in Table 1.1. It classifies the water quality to 5 ranges from high to low quality.

**Table 1.1** River quality standards (after DoE, 1994)

Class	Dissolved oxygen % saturation 10 percentile	BOD (ATU) mg/l 90 percentile	Total ammonia mg N/l 90 percentile	Un-ionised ammonia mg N/l 95 percentile
RE1	80	2.5	0.25	0.021
RE2	70	4.0	0.6	0.021
RE3	60	6.0	1.3	0.021
RE4	50	8.0	2.5	-
RE5	20	15.0	9.0	-

Note : Additional RE criteria for pH, Hardness, Dissolved Copper and Total Zinc are not illustrated

***Bathing waters***

In the United Kingdom, coliform bacteria are used as one of required criteria to standardise the bathing water as shown in Table 1.2. Its figures may be different from other countries, in terms of the approach to obtain the bacterial parameters. Moreover, the table also illustrates the exceedance period, which is an average period within a bathing season.

**Table 1.2** Coliform bacteria in identified bathing waters (after DETR, 1997)

Parameter	Threshold concentration (No./100 ml)	Total duration for which threshold can be exceeded (% of bathing season)
Faecal coliforms	2000	1.8
Total coliforms	10000	1.8

---

### ***General amenity***

The basic need of this general amenity is mainly concerned with the aesthetic quality of the receiving waters. The causes of the aesthetic problems are likely to come from polluting gross solids, such as faecal solids, toilet tissue, condoms, sanitary towels, plastic release strips and cotton buds. Hence, these could be prevented by setting emission standards at the discharge point of the CSOs. The standards to prevent the aesthetic problems in the waters are summarised and shown in Table 1.3, which includes minimum performance requirements for good engineering designs.

## **1.3 Aims of thesis**

Due to the awareness of the quality of the waters, several regulations are issued as to reach the sustainable ecosystems. However, all of them are to control a number of solid and soluble substances in the sewerage, which may be discharged from outfalls to the surrounding waters. Therefore, it may be worthwhile either to perceive a number of such pollutants travelling along the sewer system or to predict their quantity precisely before being discharged. This reason is a key driver to study the solute pollution, such as BOD, ammonia and faecal bacteria as mentioned in the regulation section, dispersing along the sewers and manholes. Besides, it was also unable to avoid a study of energy losses in the sewer systems, particularly due to manholes, since it enforces the sewage movement to the outfalls. Hence, the objectives of this study regarding changes in pipe direction at a manhole are:

- To improve the understandings of solute mixing behaviour in a manhole
- To quantify the magnitude of dispersive fraction ( $\gamma$ ) used in ADZ technique
- To quantify the magnitude of head loss coefficient (K)
- To find the relationship between solute dispersion and energy loss

These will be investigated over a range of flow rates and surcharge heights.



**Table 1.3** Standards for protecting amenity use (after DETR, 1997)

<b>Amenity use category</b>	<b>Expected frequency of spills</b>	<b>Standard</b>
High Amenity	> 1 spill/year	6 mm solids separation
	<= 1 spill/year	10 mm solids separation
Moderate Amenity	> 30 spills/year	6 mm solids separation
	<= 30 spills/year	10 mm solids separation
Low Amenity & Non-Amenity	-	Good engineering design

**High Amenity**

Area where bathing and water contact sport (immersion), is regularly practised (e.g. wind surfing, sports canoeing).

Watercourse passes through formal public park or beside formal picnic site.

Shellfish waters.

**Moderate Amenity**

Area used for recreation and contact sport (non-immersion e.g. boating).

Popular footpath adjacent to watercourse.

Watercourse passes through housing development of frequently used housing centre area (e.g. bridge, pedestrian area, shopping area).

**Low Amenity**

Basic amenity use only.

Casual riverside access on a limited or infrequent basis, such as a road bridge in a rural area, or footpath adjacent to watercourse.

**Non-Amenity**

Seldom or never used for any amenity purposes.

Remote or inaccessible area.

**6 mm solids separation**

Separation, from the effluent, of a significant quantity of persistent material and faecal/organic solids greater than 6 mm in any two dimensions. This should be applied to at least 80 % of the spilled volume in a typical year, the remainder being subject to 10 mm solids separation. Alternatively, the hydraulic design of the 6 mm solids separation can be based on treating 50 % of the volume discharged in a 1 year return period design event.

**10 mm solids separation**

Separation, from the effluent, of a significant quantity of persistent material and faecal/organic solids giving a performance equivalent to that of a 10 mm bar screen.

**Good engineering design**

Design of combined sewer overflow structures in accordance with the recommendations of FWR report FR0488 (Balmforth et al, 1994).

---

## 1.4 Contents of thesis

This thesis is divided into 5 main chapters, namely literature review, experimental work, experimental results, CFD simulation and discussion. The collection of theories and previous studies concerning both energy losses and solute transport within a sewer system is briefly described in the literature review. The former part presents some constructive equations for flow rate in pipes with/without surcharge conditions. Typical aspects of manholes are also mentioned and energy losses due to a manhole are presented in terms of the head loss coefficient, which varies with physical properties of each manhole. Afterwards, 2 ideal reactors are also described in order to measure partial mixing in a manhole. At the end of the section, general governing equation for Computational Fluid Dynamics (CFD) is briefly described, including some prior work in environmental engineering. Meanwhile, the latter summarises the concepts of solute dispersion with regard to mathematical models, such as Advection Dispersion Equation (ADE) and Aggregated Dead Zone (ADZ).

Chapter 3, experimental work, gives a description of experimental facilities used in the investigation of energy losses and solute movement across a manhole by varying plane angles, surcharge levels and discharge with/without benching. The surcharge levels were measured by means of a water level follower. A 30° V-notch weir was employed for measuring flow rate. 88 mm diameter manometers were also installed to observe the head loss due to a manhole and fluorometers were placed with adapters to measure dye concentration. After that, procedures of data correction and analysis are also explained and presented in Chapter 4 for experimental results.

To investigate the energy losses due to a manhole with changes in pipe direction by simulation, a short description of CFD processes are given in Chapter 5. CFD simulation also helps to visualise flow patterns in the manhole very well, although only a general, basic analysis was performed. But these models may not be adequate to determine the head loss coefficient because the eccentricity of the pipe direction of the manhole may required advanced models in CFD software package to be used.

---

Discussion is the last major chapter of this thesis, which concerns the head loss coefficient, travel time, dispersive fraction, energy dispersion and cells in ADZ model. The loss coefficient from laboratory was compared to the results from the preliminary investigation of CFD simulation. Travel time from each manhole's configuration was presented as a function of flow rate and surcharge. Afterwards, dispersive fraction was used to describe the degree of partial mixing taking place in the manhole. Then, energy dissipation describes a relationship between energy loss due to a manhole and residence time for each plane angle. Finally, to improve predictions of downstream profiles, a single cell ADZ model is grouped together with serial and/or parallel connections.

---

## Chapter 2

# Literature review

This chapter consists of sections describing the sewer system, solute transport and computational fluid dynamics. In the sewer system, the main focus is on manhole head losses and previous work on solute transport. Meanwhile, transport equations are derived from the diffusion law in stagnant fluid, then derived into the solute transport in fluid flow and turbulent flow. Finally, 2 numerical models, namely ADE and ADZ, are described and followed by CFD information.

### 2.1 Sewer system

A sewer system mainly consists of 2 main parts, such as sewer and manholes, to convey waste or storm drain water to a wastewater treatment plant or to receiving waters. In general, there are 3 types of sewer system: sanitary, storm drain and combined sewers (Qasim, 1985). The sanitary sewer receives wastewater from residential, commercial and industrial areas, while the storm sewer is used to drain the surface runoff. When the designed sewer carries both sanitary wastewater and storm water, it is called “combined sewer”. In reality, there will be another amount of infiltration/inflow in each sewer type. For sizing the sewer, not only the flow rate but also the energy losses should be properly considered and selected.

---

### 2.1.1 Flow design

#### *Sanitary flow*

Flow rate for sanitary sewers comes from water supply and infiltration/inflow. The amount of the water supply becoming the wastewater is related to the patterns of land use, commercial growths and population estimates (Qasim, 1985).

#### *Storm drain flow*

Storm flow rate is widely calculated from the Rational method. It is based on the assumption that the maximum storm drainage is the product of the runoff coefficient ( $C_r$ ), the rainfall intensity ( $i$ ) and the area of the watershed ( $A_w$ ). It can be written as the following equation.

$$Q = C_r i A_w$$

#### *Infiltration/Inflow*

Infiltration (Qasim, 1985) is caused by the groundwater entering the sewers via sewer connections, cracked pipes, and defective pipes and manholes. Inflow is the surface runoff which flows into the sewers through manhole cover or illegal connection. Such an amount of infiltration/inflow is a function of the length, the age and the material of the sewers; the level of the groundwater; and the number of the illegal connections. To reduce infiltration/inflow, new sewers should have tight connections. Also, old sewers should have an effective evaluation and rehabilitation because during wet weather, a greater amount of infiltration/inflow might lead to the hydraulic failure of conveying the wastewater and prone to flooding.

### 2.1.2 Flow equation

#### *Flow in pipes and open channels*

In general, there are two equations, namely Colebrook-White and Manning, used to design the velocity ( $V$ ) for the pipe or channel (Reed, 1983).

$$V = -\sqrt{32gRs} \log \left( \frac{k_s}{14800R} + \frac{1.255\nu}{R\sqrt{32gRs}} \right) \quad (2.1)$$

$$V = \frac{1}{n} R^{2/3} s^{1/2} \quad (2.2)$$

where

$k_s$  = equivalent sand roughness, mm

$R$  = hydraulic radius, m

$s$  = hydraulic gradient or invert slope

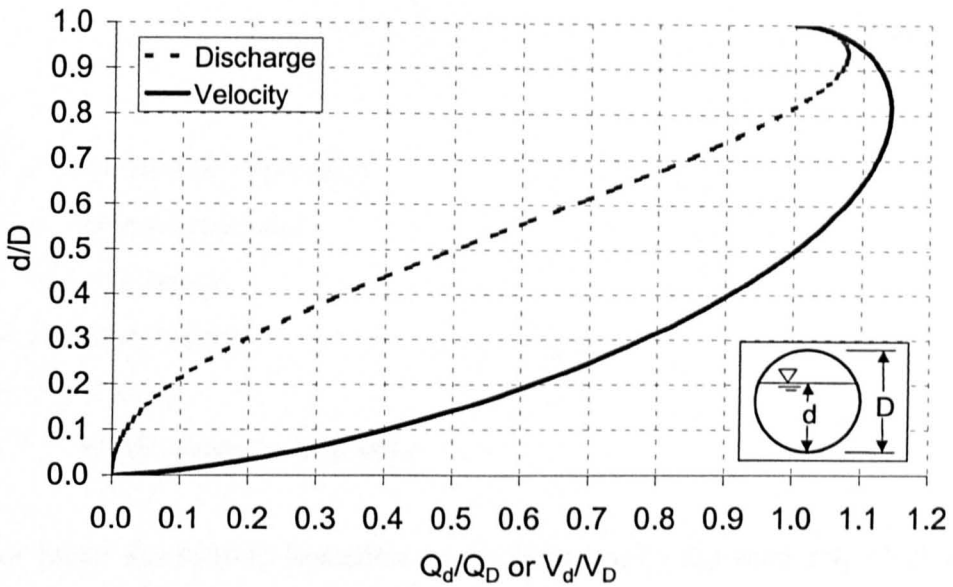
$g$  = acceleration due to gravity,  $m/s^2$

$\nu$  = kinematic viscosity,  $m^2/s$

$n$  = coefficient of roughness

Equation 2.1 and 2.2 are the Colebrook-White equation and Manning equation, respectively. Reed (1983) recommended that the Colebrook-White equation should be applied for storm sewers since it covers the hydraulic behaviour of turbulent flow, while Qasim (1985) and Young et al (1999) introduced only the Manning equation to determine the velocity in pipes and channels.

Either the Colebrook-White or Manning equations can also govern partial-full flow ( $Q_d/Q_D$ ) and partial-full velocity ( $V_d/V_D$ ). At each water depth ( $d$ ) in the pipe diameter ( $D$ ) as shown in Figure 2.1, the greatest discharge and the fastest velocity will take place where the ratio of the flow ( $Q_d/Q_D$ ) or velocity ( $V_d/V_D$ ) is greater than 1 on the x axis. In other words, when  $d/D$  is more than about 0.8, the discharge will be greater than the full flow as well as once  $d/D$  is higher than around 0.5, the velocity will be faster than the velocity at full flow.



**Figure 2.1** Partial-full flow in a circular pipe

### ***Design velocity***

The problems of sedimentation and erosion should be avoided in both sanitary and storm sewers. At the low-flow conditions during dry weather, the deposition of solids in sanitary sewers might be occasionally permitted shortly before self-cleaning flows from peaks will flush them during a day. Qasim (1985) advised the minimum velocity of 0.3 m/s for that and the flushing velocity should be greater than 0.6 m/s to prevent the sediments in the sanitary sewers. Also, to avoid erosion, the maximum velocity is suggested at 3.0 m/s. For urban storm drainage, Reed (1983) suggested that the velocity should be between 0.76 and 3.66 m/s to prevent the sedimentation and damage due to the erosion, respectively.

### ***Major and minor losses***

Major losses are frictional losses while minor losses are caused by momentum transformation in pipes and fittings, respectively. For flow under pressure or under surcharge in the sewer system, the minor losses due to manholes should be included with considering major losses. Chadwick and Morfett (1995) presented the Darcy-Weisbach equation for pressure pipes. The equation governs the velocity head multiplied by another term related to the length, diameter and roughness of the pipe as shown in Equation 2.3.

$$h_f = \frac{\lambda L V^2}{D 2g} \quad (2.3)$$

where

$h_f$  = frictional losses in pipe

$\lambda$  = pipe friction factor

$L$  = pipe length

$D$  = pipe diameter

$V$  = velocity

$g$  = acceleration due to gravity

The minor losses due to eddy formation can be described by Equation 2.4, which is the function of the velocity head and its coefficient.

$$h_L = K \frac{V^2}{2g} \quad (2.4)$$

where

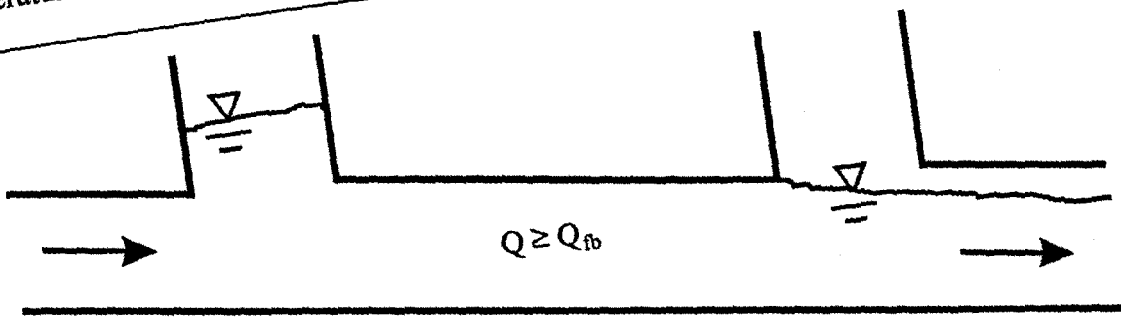
$h_L$  = local minor loss

$K$  = coefficient

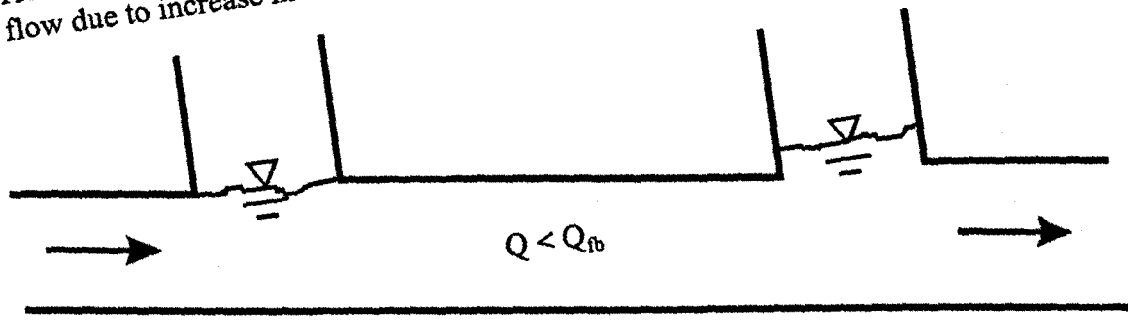
### 2.1.3 Flow routing in surcharge conditions

Sewers are generally designed to carry as much wastewater as the full pipe discharge ( $Q_b$ ) can, but the amount of sewage, especially from storm flow, is always far more than the design flow in urban storm drainage. Surcharged or pressurised flow will occur once either the storm or combined flow is greater than the full pipe capacity designed for free surface condition, or the water level higher than the soffit in the downstream manhole can generate the back water pressure to the upstream manhole. Reed (1983) categorised 4 transitions from free surface to pressurised flow or vice versa. Figure 2.2(a) and (b) illustrates the transition from free surface to surcharged flow because of increases in discharge and in water level at downstream manhole, respectively. Conversely, the transition from surcharged to free surface flow is shown in Figure 2.2 (c) and (d) since discharge and downstream water level reduce, respectively.

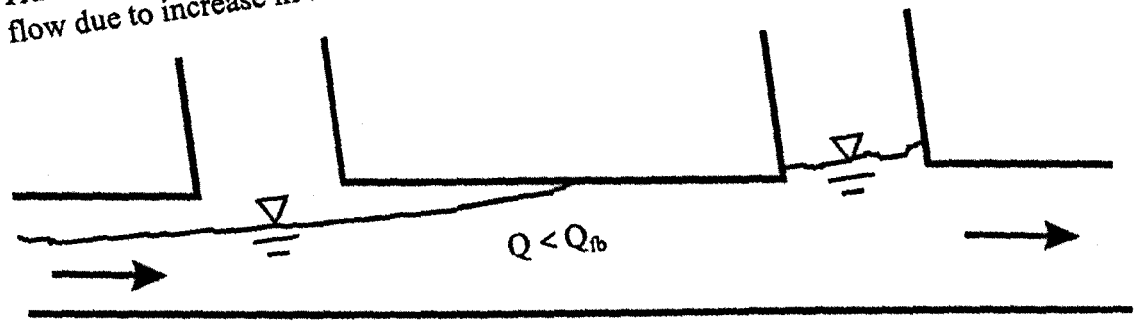




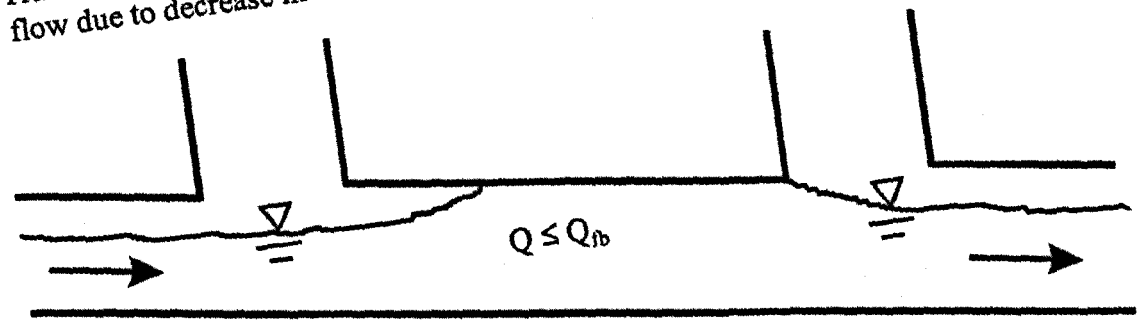
(a) Transition from free surface to pressurised flow due to increase in discharge



(b) Transition from free surface to pressurised flow due to increase in downstream water level



(c) Transition from pressurised to free surface flow due to decrease in discharge



(d) Transition from pressurised to free surface flow due to decrease in downstream water level

Figure 2.2 Transitions between free surface and surcharged flow (after Reed, 1983)

---

## 2.2 Sewer network and Real Time Control (RTC)

In reality, the size and duration of storms are different from the design storm. As a result, the static drainage network cannot efficiently carry the sewage to wastewater treatment plant, combined-sewer-overflows (CSOs) or receiving waters. As an alternative, a dynamic drainage system is provided by installing some devices into the sewer network in order to monitor flow rate and the concentration of pollution as well as a control system to manage these instruments is also desired. Afterwards, these observed data are modelled and simulated by mathematical equations to control an amount of spill from CSO chambers.

The objectives of the modelling are to summarise and understand the system performance in the sewer network. There are three popular models of wastewater quality, namely HydroWorks or InfoWorks at the moment from the UK, MOUSETRAP from Denmark and SWMM from the USA. These models are very useful to simulate temporal concentration distributions for combined-sewer overflows and flow loads for wastewater treatment plant. Consequently, the models can help operators predict precisely when pollutants peak and how much of a peak the pollutant is. Then, the flow rates in sewer system are controlled optimally and discharged to receiving surroundings.

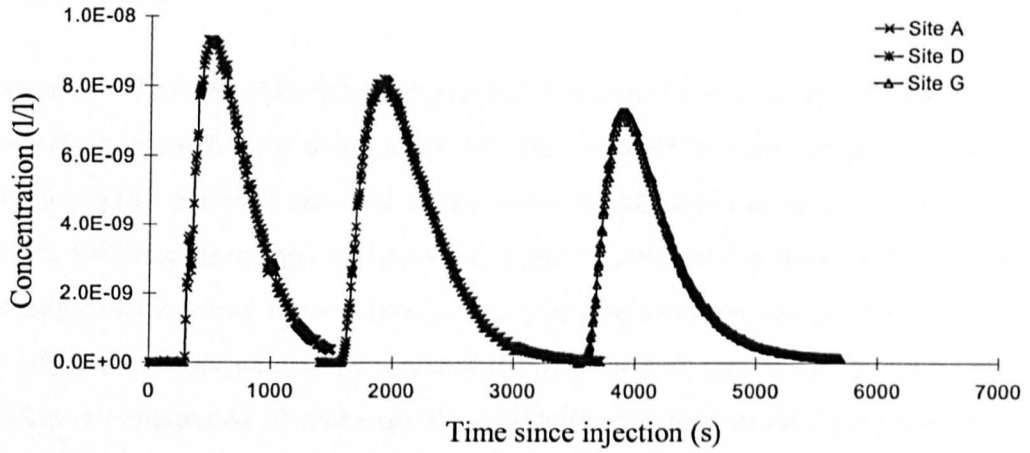
Nevertheless, such models should be verified to predict better pollutant concentration profiles. According to Herath et al (1999), HydroWorks model was considered as a better tool for wastewater quality simulation after it was compared to MOUSETRAP and SWMM. All of these models were used to simulate pollutants in a separate sewer with unsteady flow for sewer routing in Melbourne. Only the advection process for solute transport was employed in HydroWorks and SWMM, while MOUSETRAP determined the transport from advection and dispersion processes. The input data were collected at one hour intervals in dry weather period. Then, the predicted data were compared to the observed data. The highest accuracy of predicting 5-day biochemical oxygen demand (BOD<sub>5</sub>) profile, for example, accounted for 85% of the observed BOD<sub>5</sub> peak concentration and 78% of the observed BOD<sub>5</sub> peak load. This figure might be made higher, if the models obtain more data from laboratory, especially the data of the pollution transport in manholes. But in an opinion of the author, it should be also

compared with the data obtained in wet weather period, rather than only the data in dry weather period. The condition of the flow in dry weather season is mostly open channel, whereas in wet weather period it is flow in pipe under surcharge condition. The latter causes more effects of dispersion in the trapped volume of a manhole and if this dispersion effect is included in a wastewater quality model, it may enhance the prediction of solute concentrations at discharges of CSOs.

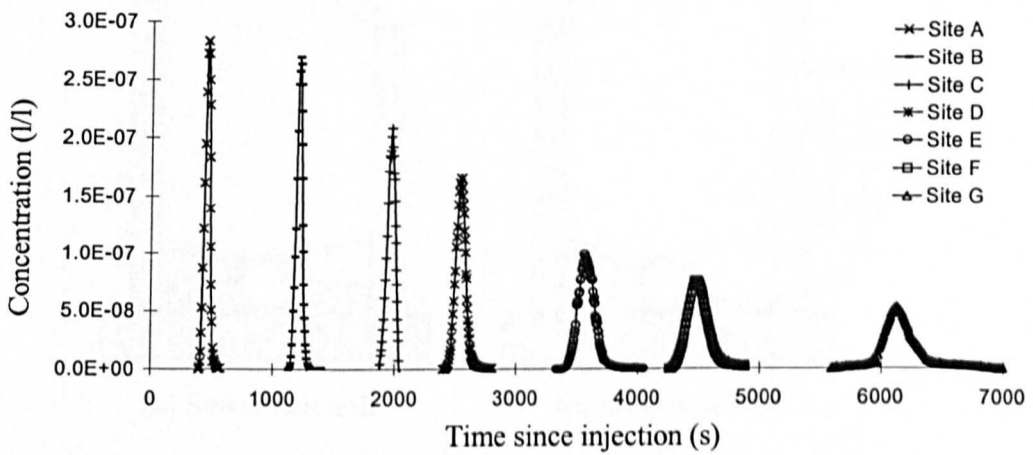
### 2.3 Sewer tracing studies

Boxall et al (2003) utilised tracing techniques to investigate solute transport and dispersion processes in a combined sewer system in the UK. The tracer test had been observed in a 375 mm diameter pipe, approximately 1.5 km long, for both storm and dry weather flow conditions. Within the range of the sewer, 7 sites, namely A, B, C, D, E, F and G, were located at 0, 288, 689, 871, 1093, 1205 and 1468 m respectively to record dye concentration profiles and to take samples of the sewage. The flow rates were approximately 100 l/s and 30 l/s for storm and dry weather flow conditions respectively. Due to difficulties during the storm flows, only 3 concentration profiles from site A, D and G are shown in Figure 2.3. It presented a slight reduction in peak concentration with skewed profiles from site A to G due to surcharged ancillary structures in the sewer system. Besides, Figure 2.4 shows 7 concentration profiles from each site in the dry weather flow condition. It was clear that all the profiles were almost Gaussian distribution, which was similar to idealised pipe mixing theory.

In addition, Boxall et al (2003) also presented values for the mixing parameters of the aggregated dead zone model (ADZ) model as shown in Table 2.1. During the dry weather flow test, manholes were not surcharged, however under the storm conditions surcharges up to 1.5 m were recorded at some sites. The average dispersive fraction from ADZ analysis was displayed at 0.045 and 0.043 for storm and dry weather flow conditions, respectively. Moreover, the average velocities of 0.53 and 0.29 m/s are also presented for the storm and dry weather flow conditions.



**Figure 2.3** Concentration profiles from storm conditions (after Boxall et al, 2003)



**Figure 2.4** Concentration profiles from dry weather flow conditions (after Boxall et al, 2003)

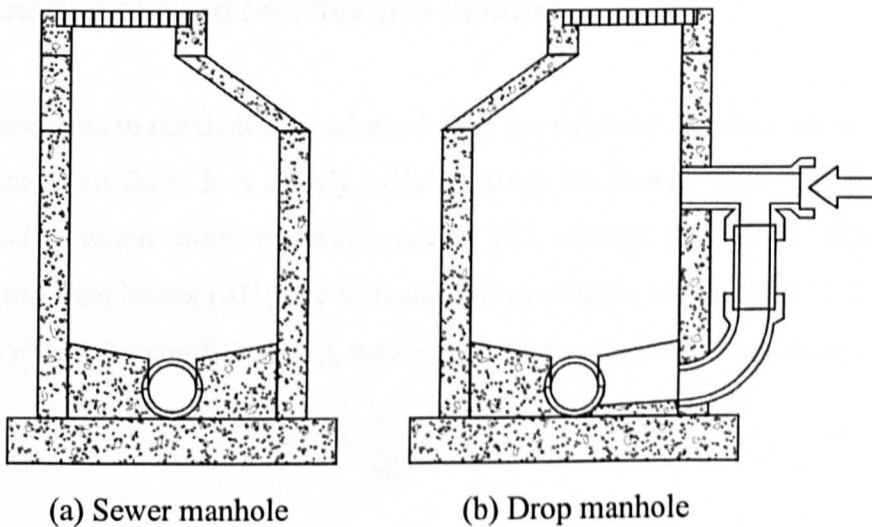
**Table 2.1** Summary results from tracer data (after Boxall et al, 2003)

Conditions		Dispersive fraction	Velocity (m/s)
Storm	Average	0.045	0.53
	SD	0.045	0.08
Dry weather flow	Average	0.043	0.29
	SD	0.021	0.09

Note: SD = standard deviation

## 2.4 Manholes

In general within an urban drainage system, a manhole has only one chamber for both inspecting and cleaning a sewer network. The manhole's walls are probably made of concrete block, pre-cast concrete rings, brick or poured concrete. It functions as a junction for changes in pipe's alignment, grade or size. At the bottom of the manhole, benching is always cast by concrete to be a standing position and guidance for sewage flow. Figure 2.5 presents typical manholes: sewer manhole and drop manhole. The drop manhole is constructed to eliminate the problems of solids or sewage splashed on the wall when the elevation of an outlet is greater than 0.60 m from an inlet.



**Figure 2.5** Typical manholes

To provide easy access and safe working conditions, the criteria for manholes should be designed. Several, different codes are used to specify chamber dimensions, which depend on pipe diameter and the depth of the manhole. For example here only the chamber dimension from Escritt (1984) is shown. Table 2.2 illustrates the relationship between the diameter of the outlet and the diameter of the chamber. However, when the depth of the manhole is less than 0.60 m, the designed diameter may only allow rodding to clean the sewer from ground level.

**Table 2.2** Relationship between diameter of outlet and chamber (after Escritt, 1984)

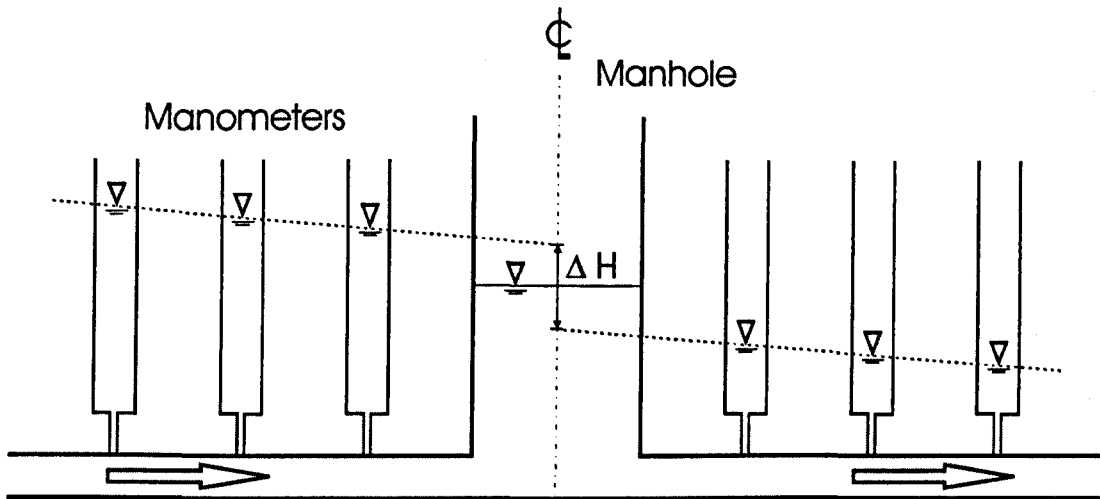
Diameter of outlet (mm)	Diameter of chamber (mm)
150 to 375	900, 1050, 1200, 1350, 1500 and 1800
150 to 525	1050, 1200, 1350, 1500 and 1800
150 to 600	1200, 1350, 1500 and 1800
150 to 675	1350, 1500 and 1800
150 to 990	1500 and 1800
Over 900	1800

## 2.5 Estimation of head loss due to a manhole

Energy losses due to manholes are adopted from the equation of minor losses (Equation 2.4) for pressured flow. It is clearly different from the energy losses for free surface flow, which friction from hydraulic radius ( $R$ ) mainly influences. Equation 2.5 describes the head losses ( $\Delta H$ ) due to manholes as a linear relationship of the velocity head ( $V^2/2g$ ) and the coefficient ( $K$ ), which is particular for each manhole aspect.

$$\Delta H = K \frac{V^2}{2g} \quad (2.5)$$

In practice, Howarth and Saul (1984), Lindvall (1984), Pedersen and Mark (1990), and Kusuda and Arao (1996) estimated the head losses at the centre of the manhole from the different level of upstream and downstream hydraulic gradients. Figure 2.6 illustrates the observed head losses, which was measured from the hydraulic gradients of 3 manometers upstream and downstream. Then, the known head loss and mean flow velocity, determined from the discharge and pipe area, were employed to calculate the coefficient from Equation 2.5.



**Figure 2.6** Head loss due to a manhole

## 2.6 Coefficient of head losses

Archer et al (1978) introduced the effect of surcharge levels on head losses in manholes. Both rectangular and circular manholes were studied with varying deflection angles of the inlet and outlet pipes, such as 0°, 30° and 60°. Their results show that the head loss is proportional to the velocity head. The variation of the head loss coefficient (K) is displayed in Table 2.3. It seems that the coefficient from rectangular manholes is less than that of circular manholes.

**Table 2.3** Head loss coefficient (after Archer et al, 1978)

Type of manhole	0° deflection	30° deflection	60° deflection
Rectangular	0.1	0.4	0.85
Circular	0.15	0.5	0.95

Howarth and Saul (1984) investigated the magnitude of loss coefficients, K, in manholes varying in size and shape with/without benching. From testing with steady and unsteady flow, an oscillation, a sway and a swirling motion were observed in the manhole at some surcharge levels. However, only the swirling motion affected the loss coefficient. For the result of the manhole size variable, it appears that the loss coefficient is increased when the manhole size is expanded. Moreover, from study, it is clear that the loss coefficient of a square manhole is lower than that of a circular

manhole at the same size, which is similar to the results from Archer et al (1978). This may be caused by the stagnant zones in the corners. Also, benching in the manhole chamber influences the loss coefficient. This is because it can reduce the swirling motion at some flow rates and at low surcharge levels.

The head loss coefficient due to a manhole for a straight pipe and a straight main pipe with a 90° lateral were also investigated by Lindvall (1984). The experiment was set up from PVC  $\phi$  0.144 m pipes for both upstream and downstream sides of the manhole. The manhole diameters were 1.7, 2.6 and 4.1 times the main pipe diameter ( $D$ ). Each manhole was also tested with 2 types of benching, i.e. half and full height of the pipe diameter, between 1.1-5.5 $D$  water depth. At the centre of the manhole, the coefficient was observed from the difference of upstream and downstream hydraulic gradients, each of which was a line obtained from 3  $\phi$  14 mm piezometric heads. From the experimental results, the coefficient was significantly high when the water depth ratio ( $y/D$ ) was lower than 2.0 and the loss coefficient almost became constant after the water depth ratio was greater than 2.5 for the result of the half-benched, straight pipe manholes. Lindvall (1984) also claimed that the effect of rotation motion in the manhole caused such high coefficient. Next, for the result from full-benched, straight pipe manholes, it was reported that the coefficient was moderately high between the water depth ratio of 1.1 to 2.0. The last results were presented for both types of benching in the straight pipe manholes with 90° lateral. The loss coefficient for these cases was independent of the water depth ratio or surcharge, excluding the large number of the lateral flow ( $Q_l/Q$ ) and manhole diameter ratio ( $D_m/D$ ). When the lateral pipe had the less velocity than the main pipe, the upstream loss coefficient, determined from the different head of upstream and downstream pipes, was nearly equal to the lateral coefficient obtained from the head loss between the lateral and downstream pipes divided by the velocity head. Also, once the velocity in the lateral pipe increased, the main pipe would have greater losses.

Pedersen and Mark (1990) published energy losses in manholes from experimental results and then compared these to the result of jet theory. The ratio of the manhole diameter to the pipe diameter was considered as the main governing parameter to


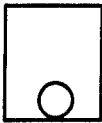
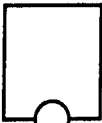
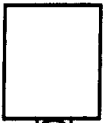


estimate energy losses ( $\Delta H$ ) in each shape of manhole as shown in Table 2.4. The relationship was presented as

$$K = \zeta \left( \frac{D_m}{D} \right) \quad (2.6)$$

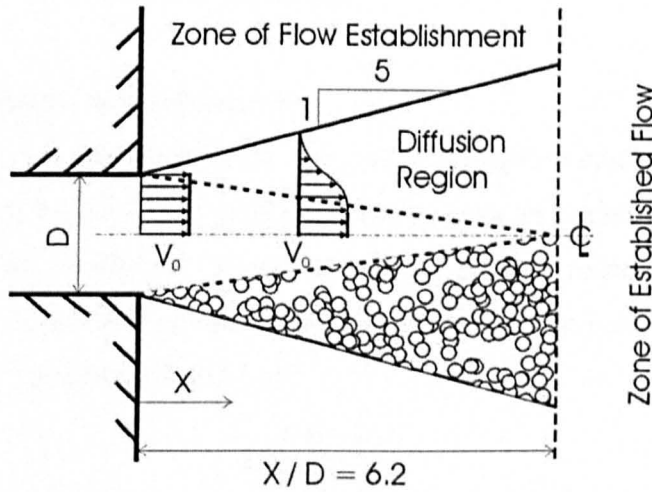
where  $K$  = head loss coefficient;  $\zeta$  = shape factor;  $D_m$  = manhole diameter; and  $D$  = pipe diameter.

**Table 2.4** Estimated shape factor from measurements with  $D_m/D$  up to 4 (after Pedersen and Mark, 1990)

Shape				
$\zeta$	0.24	0.12	0.07	0.025

Furthermore, Pedersen and Mark (1990) also claimed that the coefficient was affected by submerged jet at the entrance of the incoming pipe as shown in Figure 2.7. It shows that the jet comprises a diffusion region and a core region, in which the velocity ( $V_0$ ) is constant in the zone of flow establishment. Such a shape of benching can confine some region of the core and diffusion zones, which directly influences the loss coefficient. For example, when the shape factor is 0.24, nothing confines the submerged jet. But once most of the jet region is confined, the shape factor was reduced to 0.025.

Kusuda and Arao (1996) presented the study of energy losses at circular drop manholes. The drop manhole is the manhole with step height, which is the different level of the upstream and downstream pipes. While the ratio of the step height between the inlet and outlet to the inside diameter of manholes was small, the energy losses in terms of the head loss coefficient increased because of the increase in manhole size. But when the ratio of the step height to the inside diameter manhole ranged from 0.5 to 1.0, the head loss coefficient moderately increased for the increase in such ratio. However, after the ratio was higher than 1, it was independent of the manhole size.



**Figure 2.7** Submerged jet: Velocity distribution and Diffusion region (after Albertson et al, 1950)

Arao and Kusuda (1999) investigated the effects of changes in pipe direction on the relationship of energy losses and circular drop manholes. The result showed that the energy loss coefficient ( $K$ ) at any pipe direction was significantly different when the drop ratio of the inlet and outlet was less than 1. But when the drop ratio was equal to 1, the energy loss coefficient ( $K$ ) was almost similar for each pipe bending angle.

Young et al (1999) introduced some empirical formulae to analyse head losses due to a manhole by hydraulic grade line. The losses are functions of surcharge, inlet and outlet pipes, manhole size, benching type and flow rate. The main equation of energy losses governs the product of the composite energy loss coefficient ( $K_1$ ) and velocity head ( $V_o^2/2g$ ), where  $V_o$  = outlet velocity (m/s) and  $g$  = acceleration due to gravity ( $9.81 \text{ m/s}^2$ ), as shown in Equation 2.7 and 2.8.

$$\Delta E = K_1 \frac{V_o^2}{2g} \quad (2.7)$$

$$K_1 = (C_1 C_2 C_3 + C_{4i}) \omega \quad (2.8)$$

where

$C_1$  = coefficient related to relative manhole size

$C_2$  = coefficient related to water depth in the manhole

$C_3$  = coefficient related to lateral flow, lateral angle and plunging flow

$C_{4i}$  = coefficient related to relative pipe diameters

$\omega$  = correction factor for benching

### ***Coefficient of relative manhole size ( $C_1$ )***

The coefficient was analysed from data of a straight-manhole pipe. The relative manhole diameter is a ratio of a manhole diameter over an outlet pipe diameter,  $D_m/D_o$ . From the data, the coefficient increases with the relative manhole size due to more space and time for the dissipation of the velocity head. The head loss coefficient,  $C_1$ , can be written as Equation 2.9 and 2.10.

$$C_1 = \frac{0.9 \left( \frac{D_m}{D_o} \right)}{\left( 6 + \frac{D_m}{D_o} \right)} \quad \text{for } 2.0 \leq \frac{D_m}{D_o} \leq 4.0 \quad (2.9)$$

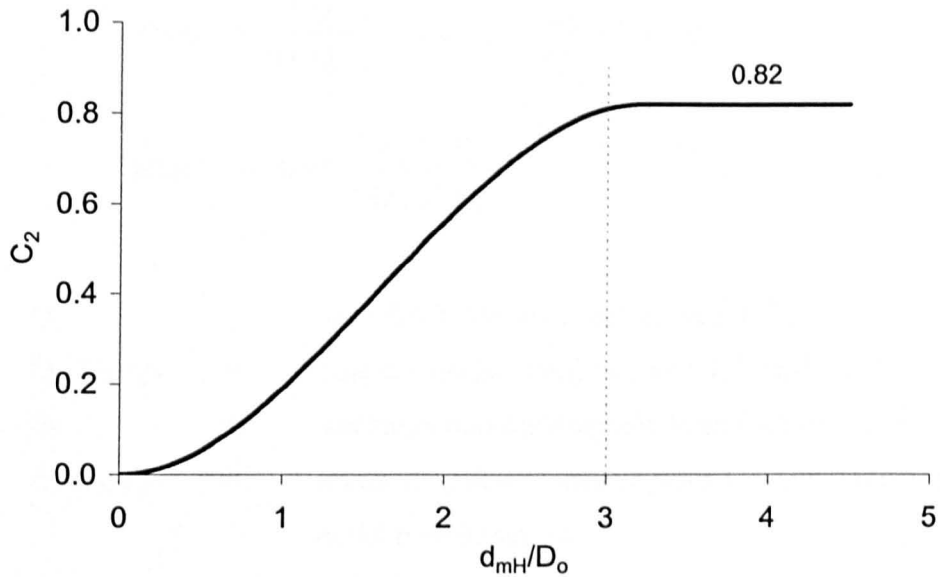
$$C_1 = 0.36 \quad \text{for } \frac{D_m}{D_o} > 4.0 \quad (2.10)$$

### ***Coefficient of water depth in the manhole ( $C_2$ )***

The coefficient of water depth,  $C_2$ , significantly increases with relative water depth,  $d_{mH}/D_o$ , until 2; and the rate of change will decrease while the relative water depth is close to 3 as shown in Figure 2.8. Equation 2.11 and 2.12 present the coefficient at the relative water depth equal to or less than 3.0 and greater than 3.0, respectively.

$$C_2 = 0.24 \left( \frac{d_{mH}}{D_o} \right)^2 - 0.05 \left( \frac{d_{mH}}{D_o} \right)^3 \quad \text{for } \frac{d_{mH}}{D_o} \leq 3.0 \quad (2.11)$$

$$C_2 = 0.82 \quad \text{for } \frac{d_{mH}}{D_o} > 3.0 \quad (2.12)$$



**Figure 2.8** Coefficient of water depth,  $C_2$

### ***Coefficient of multiple inflows ( $C_3$ )***

The coefficient of multiples inflows,  $C_3$ , is an effect of flow rate, angle of the inflow pipe connection, and elevation of the inflows. This is the most complex coefficient in the composite energy coefficient equation and analysed from scattered experimental data due to air entainment and turbulence (Young et al, 1999). Hence, in an opinion of the author, this was a limitation of the equation. Nevertheless,  $C_3$  can be calculated from Equation 2.13.

$$C_3 = \text{Term1} + \text{Term2} + \text{Term3} + \text{Term4} + \text{Term5} \quad (2.13)$$

where

$$\text{Term1} = 1$$

$$\text{Term2} = \sum_{i=1}^4 \left( \frac{Q_i}{Q_0} \right)^{0.75} \left[ 1 + 2 \left( \frac{Z_i - D_{mH}}{D_o} \right)^{0.3} \left( \frac{Z_i}{D_o} \right)^{0.3} \right]$$

$$\text{Term3} = 4 \sum_{i=1}^3 \frac{(\cos \psi_i)(HMC_i)}{\left( \frac{d_{mH}}{D_o} \right)^{0.3}}$$

$$\text{Term4} = 0.8 \left| \frac{Z_A}{D_o} - \frac{Z_B}{D_o} \right|$$

$$\text{Term5} = \left| \left( \frac{Q_A}{Q_o} \right)^{0.75} \sin \psi_A + \left( \frac{Q_B}{Q_o} \right)^{0.75} \sin \psi_B \right|$$

$$\text{HMC}_i = 0.85 - \left( \frac{Z_i}{D_o} \right) \left( \frac{Q_i}{Q_o} \right)^{0.75}$$

and

$Q_o$	=	total discharge in the outlet pipe, m <sup>3</sup> /s
$Q_1, Q_2, Q_3$	=	pipe discharge in inflow pipes 1, 2 and 3, m <sup>3</sup> /s
$Q_4$	=	discharge into the manhole from the inlet, m <sup>3</sup> /s
$Z_1, Z_2, Z_3$	=	invert elevation of inflow pipes 1, 2 and 3 relative to the outlet pipe invert, m
$D_o$	=	outlet pipe diameter, m
$D_m$	=	manhole diameter, m
$d_{mH}$	=	depth in the manhole relative to the outlet pipe invert, m
$\psi_1, \psi_2, \psi_3$	=	angle between the outlet main and inflow pipes 1, 2 and 3 degrees measured clockwise from the outlet pipe
$\text{HMC}_i$	=	horizontal moment check for pipe I
$Q_A, Q_B$	=	pipe discharges for the pair of inflow pipes that produce the largest value for term 4, m <sup>3</sup> /s
$Z_A, Z_B$	=	invert elevation, relative to outlet pipe invert, for the inflow pipes that produce the largest value for term 4, m

Each term in the equation for  $C_3$  is responsible for up to 3 inflows pipes, plunging flow from the inlet and angles between 0° to 360°. For a simple inflows with one inlet and outlet,  $C_3$  will only be term 1 or equal to 1.0. The second term comes from the effect of greater turbulence from flows plunging at a high level. The third term is a result of angles on head losses, which is considered with the horizontal moment check ( $\text{HMC}_i$ ). If  $\text{HMC}_i$  is less than 0, the third term can be negligible. The fourth term will be added when there is more than one inflow pipe on the manhole. Furthermore, if each inflow pipe has  $\text{HMC}_i$  greater than 0, the pipe, which offers the highest value for the fourth term, will be employed to calculate the fourth and fifth terms.

### ***Coefficient of relative pipe diameters ( $C_4$ )***

With respect to conservation of momentum,  $C_4$  is calculated from Equation 2.14, which is for the losses due to entrance from each pipe. The limit of the coefficient is 9.0 for this empirical equation.

$$C_{4i} = 1 + \left[ \left( \frac{Q_i}{Q_o} + 2 \frac{A_i}{A_o} \cos \psi_i \right) \frac{V_i^2}{V_o^2} \right] \quad (2.14)$$

where:

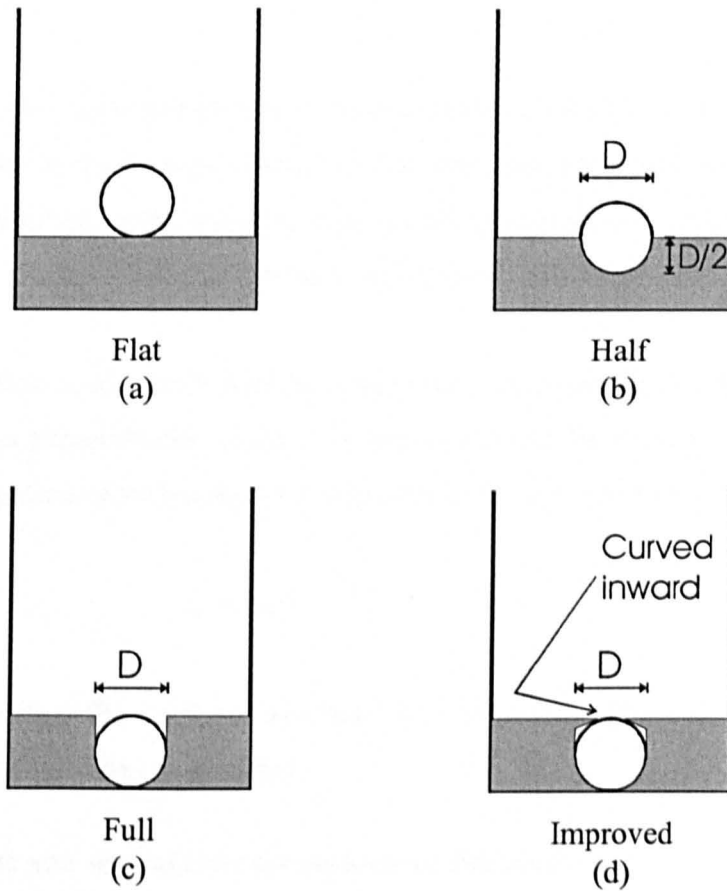
- $A_i, A_o$  = cross-sectional area of inflow and outflow pipes,  $m^2$   
 $\psi_i$  = angle between outflow pipe and inflow pipe I, degrees

### ***Benching configuration ( $\omega$ )***

Because benching affects the reduction of turbulence and smooth flow in the manhole, the head loss coefficient needs correction factors from the floor configuration in the manhole. Figure 2.9 shows 4 types of benching: flat, half, full and improved. The correction factor ( $\omega$ ) for benching is presented in Table 2.5. Figures in the table for all mentioned types of benching are shown in two columns: "Bench Submerged" and "Bench Unsubmerged", which is categorised by the ratio of  $d_{mH}/D_o$ . For the water depth ratio between 3.2 and 1.0 or free surface flow condition, the correction factor ( $\omega$ ) can be obtained from a linear interpolation from "Bench Submerged" column and "Bench Unsubmerged" column.

## **2.7 Solute dispersion**

Due to a great increase in the ability of a personal computer, not only the water quantity in sewer system, but also the water quality are simulated. In the past, just energy losses in the sewer system were investigated in order to model the sewerage for flooding protection. But recently, better environmental quality is of more concern and studied together with the energy losses. Then, one of pollutants flowed to receiving waters can be represented as a solute. Therefore, the study of the solute transport could help to determine how much of a physical, chemical, biological reactor the sewer network is in terms of mixing processes, i.e. advection and diffusion.



**Figure 2.9** Benching types for floor configuration (after Young et al, 1999)

**Table 2.5** Correction factor for benching (after Young et al, 1999)

Floor configuration	Bench submerged*	Bench Unsubmerged**
Flat floor	1.00	1.00
Benched one-half pipe diameter high	0.95	0.15
Benched one pipe diameter high	0.75	0.07
Improved	0.40	0.02

\* pressure flow,  $d_{mH}/D_o > 3.2$

\*\* free-surface flow,  $d_{mH}/D_o < 1.0$

The solute transport concerning molecular movement will be described, in order, by momentum transfer and fluid movement of the media. The explanation is also started with a simple process and developed to other complicated transport. In other words, the serial cases of the description are advection, molecular diffusion, molecular diffusion in fluid movement and molecular diffusion in turbulent flow.

### 2.7.1 Advection

Advection transport is the movement of the molecules of solute or particles in fluid with the same velocity as the average velocity of the fluid. Therefore, no momentum transfer between the molecule or the particles takes place. It can also be called “convection”, which suggests the movement by buoyancy induction (Rutherford, 1994).

The advective flux is that number of the molecules or particles transports per both units of time and area perpendicular to the flow and represents the outcome of the velocity and the concentration of such molecules or particles. It can be written as Equation 2.15.

$$I_x = u_x c \quad (2.15)$$

where  $I_x$  = advective flux in the x direction;  $u_x$  = velocity in the x direction; and  $c$  = concentration of molecules or particles.

### 2.7.2 Fick's first and second laws for molecular diffusion

For a neutrally buoyant solute in stationary fluid, the molecule of the solute diffuses in the fluid by random motion. Such diffusion can be described by the first law of Fick, the German physiologist (Rutherford, 1994). It is that the rate of solute moving is proportional to the concentration gradient. Also, this can be described by Equation 2.16,

$$J_x = -e_m \frac{\partial c}{\partial x} \quad (2.16)$$

where  $J_x$  = molecular diffusive flux in the x direction;  $c$  = solute concentration; and  $e_m$  = molecular diffusion coefficient, in which the sign is negative, since the molecules of the solute diffuse from the part of high concentration to the part of low concentration.

Figure 2.10 shows the mass balance of the element which has volume  $\Delta X \Delta Y \Delta Z$ . Mass conservation is applied to consider the rate of change in molecular diffusive flux per unit of time, referred to as Fick's second law. It can be written as Equation 2.17.



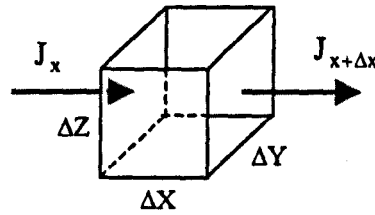


Figure 2.10 Mass balance of the element

$$\frac{M_{t+\Delta t} - M_t}{\Delta t} = (J_x - J_{x+\Delta x}) \Delta Y \Delta Z \quad (2.17)$$

where  $M_t$  and  $M_{t+\Delta t}$  = tracer mass at time  $t$  and  $t+\Delta t$ , respectively;  $J_x$  = diffusive flux (averaged over the time interval  $\Delta t$ ) entering the element;  $J_{x+\Delta x}$  = diffusive flux (averaged over the time interval  $\Delta t$ ) leaving the element;  $\Delta X$ ,  $\Delta Y$ , and  $\Delta Z$  = dimensions of the fluid element.

Meanwhile, the mass balance compared with time is applied by a Taylor's series, ignoring terms greater than second order. That is

$$M_{t+\Delta t} = M_t + \frac{\partial M}{\partial t} \Delta t \quad (2.18)$$

$$J_{x+\Delta x} = J_x + \frac{\partial J}{\partial x} \Delta x \quad (2.19)$$

Then, both Equation 2.18 and Equation 2.19 are replaced in Equation 2.17, and it becomes

$$\frac{\left( M_t + \frac{\partial M}{\partial t} \Delta t \right) - M_t}{\Delta t} = \left( J_x - \left( J_x + \frac{\partial J}{\partial x} \Delta x \right) \right) \Delta Y \Delta Z$$

$$\frac{\partial M}{\partial t} = - \frac{\partial J_x}{\partial x} \Delta x \Delta Y \Delta Z \quad (2.20)$$

When  $c = M/\Delta x \Delta y \Delta z$ , then the equation changes into Equation 2.21.

$$\frac{\partial c}{\partial t} = -\frac{\partial J_x}{\partial x} \quad (2.21)$$

Molecular diffusive flux (Equation 2.16) is substituted into Equation 2.21 and reformed to be

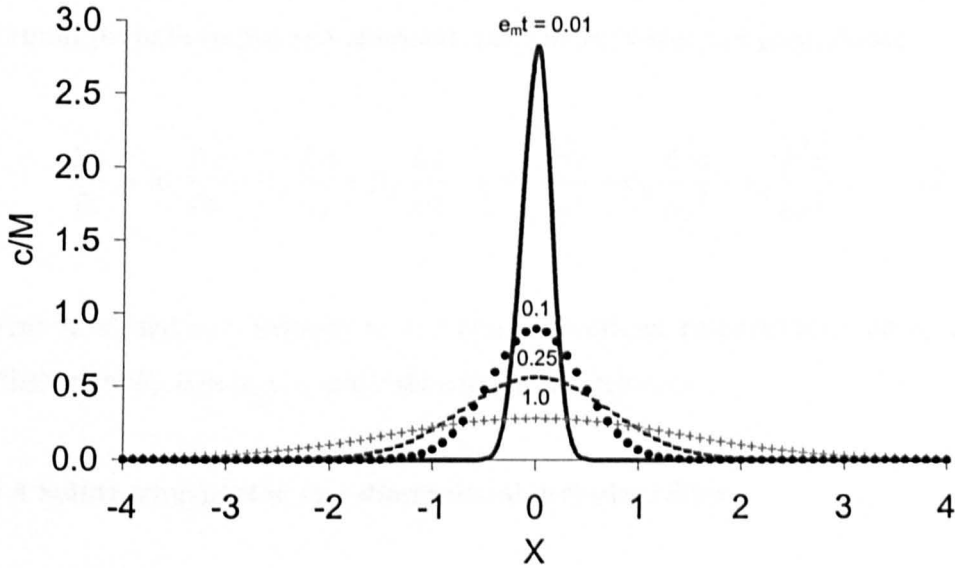
$$\frac{\partial c}{\partial t} = -\frac{\partial \left( -e_m \frac{\partial c}{\partial x} \right)}{\partial x} \quad (2.22)$$

When  $e_m$  is constant, Equation 2.22 becomes

$$\frac{\partial c}{\partial t} = e_m \frac{\partial^2 c}{\partial x^2} \quad (2.23)$$

Equation 2.23 is the **Fick's second law** for one dimensional diffusion in stationary fluid and  $e_m$  is a constant. This equation is used to predict the tracer concentration with respect to the time and distance, rather than only predicted concentration along the distance as the Fick's first law. The solution of the second law was presented by Crank (1979) for an instantaneous plane source. It was one dimensional diffusion, expanding on x direction of an amount of substance M. At  $x = 0$  and  $t = 0$ , M was deposited and its concentration due to diffusion can be calculated from Equation 2.24. For example, Figure 2.11 shows the ratio of  $c/M$  when the product of  $e_m t$  increased with the constant diffusion coefficient ( $e_m$ ).

$$c(x, t) = \frac{M}{2 (\pi e_m t)^{\frac{1}{2}}} \exp \left( -\frac{x^2}{4 e_m t} \right) \quad (2.24)$$



**Figure 2.11** Solution of Fick's second law for an instantaneous plane source

### 2.7.3 Molecular diffusion in fluid movement

Unlike the molecular diffusion in stationary media, fluid movement also transports the molecule by advection process. Thus, molecular diffusive flux ( $J_m$ ) in the  $x$  direction must be combined with the advective flux ( $I$ ) and included in Equation 2.21. Then, its result is shown in Equation 2.25.

$$\frac{\partial c}{\partial t} = -\frac{\partial(I_x + J_m)}{\partial x} \quad (2.25)$$

$$\frac{\partial c}{\partial t} = -\frac{\partial\left(u_x c - e_m \frac{\partial c}{\partial x}\right)}{\partial x}$$

$$\frac{\partial c}{\partial t} + u_x \frac{\partial c}{\partial x} = e_m \frac{\partial^2 c}{\partial x^2} \quad (2.26)$$

Equation 2.26 is known as **Fickian diffusion equation**. It is able to apply not only for one dimensional transport, but also for three dimensions as Equation 2.27 (Rutherford,

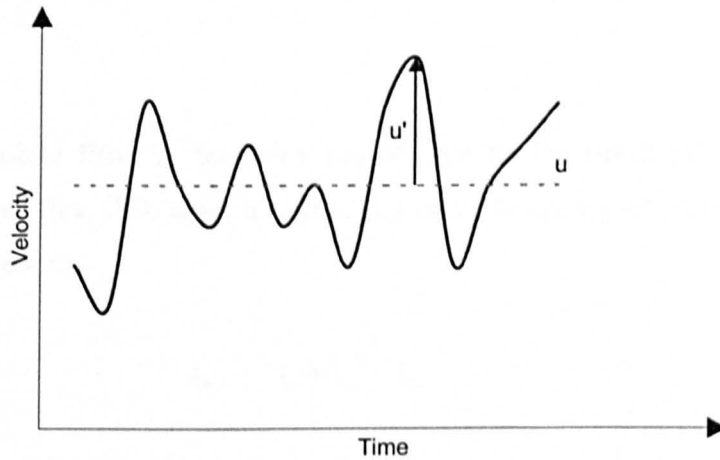
1994). This primary equation is very useful to predict the concentration of mass transport for both spatial and temporal space in air, water and groundwater.

$$\frac{\partial c}{\partial t} + u_x \frac{\partial c}{\partial x} + u_y \frac{\partial c}{\partial y} + u_z \frac{\partial c}{\partial z} = e_x \frac{\partial^2 c}{\partial x^2} + e_y \frac{\partial^2 c}{\partial y^2} + e_z \frac{\partial^2 c}{\partial z^2} \quad (2.27)$$

where  $u_x$ ,  $u_y$  and  $u_z$  = velocity in x, y and z directions, respectively; and  $e_x$ ,  $e_y$  and  $e_z$  = diffusion coefficient in x, y and z directions, respectively.

#### 2.7.4 Solute transport in one-dimensional turbulent flow

In fluid movement, turbulent flow is often encountered for scientific work. Here only one-dimensional solute transport is considered for sewer system.



**Figure 2.12** Average and fluctuating velocities

Figure 2.12 shows the average and fluctuating velocities,  $u$  and  $u'$ , respectively. These velocities are assumed to be the components of instantaneous velocity ( $U$ ). This can be written as

$$U_x = u_x + u_x'$$

Similarly, instantaneous solute concentration is also presented as

$$C = c + c'$$

where  $C$  = instantaneous solute concentration;  $c$  = temporal average solute concentration; and  $c'$  = fluctuating solute concentration. Then, the advective flux due to turbulence is

$$U_x C = (u_x + u'_x)(c + c')$$

$$U_x C = u_x c + u_x c' + u'_x c + u'_x c'$$

The  $u_x c'$  and  $u'_x c$  terms can be ignored due to both summary over the observed time period of fluctuating velocity and concentration, in which their average values will be zero (Rutherford, 1994; Wallis, 1994). So, the equation changes into

$$U_x C = u_x c + u'_x c' = I_x + I'_x \quad (2.28)$$

where  $I_x$  = advective flux in x direction; and  $I'_x$  = fluctuating advective flux in x direction.

However, total solute flux for transport should also be the result of combining the molecular diffusive flux ( $J_m$ ), advective flux ( $I_x$ ) and fluctuating advective flux ( $I'_x$ ) as the following equation.

$$J_x = I_x + I'_x + J_m$$

Again, this flux term can be replaced into Equation 2.21 in Fick's second law and becomes

$$\frac{\partial c}{\partial t} = - \frac{\partial (I_x + I'_x + J_m)}{\partial x}$$

$$\frac{\partial c}{\partial t} = - \frac{\partial \left( u_x c + u'_x c' - e_m \frac{\partial c}{\partial x} \right)}{\partial x}$$

$$\frac{\partial c}{\partial t} + u_x \frac{\partial c}{\partial x} = e_m \frac{\partial^2 c}{\partial x^2} - \frac{\partial u'_x c'}{\partial x} \quad (2.29)$$

The last term on the right hand side of Equation 2.29 is an addition to Equation 2.26, which is presented in the molecular diffusion in fluid movement. Equation 2.29 is normally for turbulent diffusion flow, in which the rate of change in the time-scale for the turbulent fluctuation is able to compare with that of the gradual concentration (Rutherford, 1994). For engineering work, this equation is hardly encountered with solute transport in rivers, but may be seen in estuarine flow due to the comparable time-scale of change in turbulent fluctuation and concentration. In the opinion of the author, data from most river tracer studies are recorded in a long period of time and this will obtain a very small value of fluctuating concentration. As a result, the last term can be ignored.

## 2.8 Advection Dispersion Equation (ADE)

The advection dispersion equation (ADE) was initially presented by Taylor (1953, 1954) for flow in pipes. Afterwards, Fischer (1966) introduced the equation for open channels. Below is the equation for one dimension.

$$\frac{\partial(AC)}{\partial t} + \frac{\partial(AUC)}{\partial x} = \frac{\partial}{\partial x} \left[ D_L A \frac{\partial C}{\partial x} \right] \quad (2.30)$$

where  $A$  = cross-sectional area of the flow,  $C$  = solute concentration,  $U$  = mean velocity,  $t$  = time,  $x$  = distance,  $D_L$  = longitudinal dispersion coefficient.

Under the assumption that  $U$  and  $D_L$  are constant, the solution of Equation 2.30 for an instantaneous point source is presented as Equation (2.31).

$$C(x, t) = \frac{M}{A\sqrt{4\pi D_L t}} \exp\left[-\frac{(x - Ut)^2}{4D_L t}\right] \quad (2.31)$$

where  $M$  = mass of tracer injected at  $x = 0$  and  $t = 0$ . Equation 2.31 is known as the Taylor Solution to the advection dispersion equation.

### Temporal profile prediction

After Taylor's experiment with regard to the longitudinal dispersion in a pipe, the advection dispersion equation was adapted to deal with the solute transport between 2 locations along a river (Fisher, 1966; Rutherford, 1994). However it does not predict a temporal downstream concentration profile well because observed profiles are more of a skew temporal concentration profile, than a Gaussian spatial concentration profile predicted by Equation 2.31. To predict such a profile, Equation 2.31 needs to be developed to deal with the skewness of the downstream profile. A better concept was that the skewness came from the summary of several small profiles. It was assumed that the upstream profile consisted of a number of slugs and each produced a small temporal concentration profile with a constant of the product of the diffusion coefficient and time,  $D_L t$ .

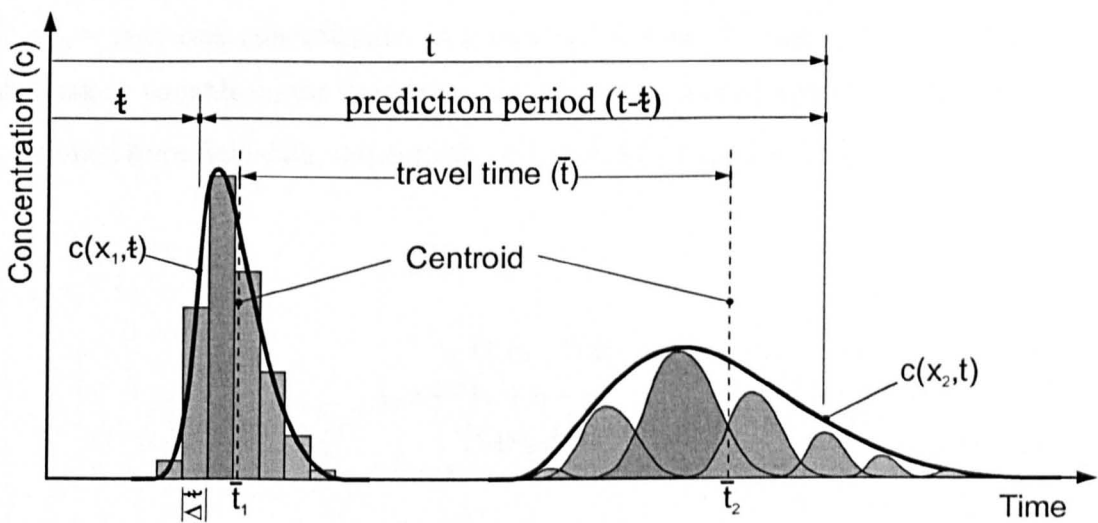


Figure 2.13 ADE routing of several slugs

Figure 2.13 illustrates concentration and time axes and the letter of  $\hat{t}$  is used to describe the time for the upstream profile, while  $t$  is for the predicted downstream profile. The upstream profile is compounded, for example, of 7 slugs, each of which is observed at the same period of time ( $\Delta\hat{t}$ ). Therefore, some terms in Equation 2.31 can be described by variables as the following.

$$x = U\bar{t} = \text{distance between 2 sites}$$

$$M = m_1 + m_2 + \dots + m_7$$

$$m_1 = c_1 U A \Delta\hat{t}$$

or  $m_i = c_i U A \Delta t$   
 prediction period =  $t - \bar{t}$

where  $i = 1, 2, \dots, 7$  in this case  
 (see Figure 2.13)

$$D_L t = D_L \bar{t} = \text{constant}$$

So, Equation 2.31 is able to reform to be Equation 2.32 (Rutherford, 1994).

$$C(x_2, t) = \sum_{i=1}^7 \frac{c_i(x_1, \bar{t}) U A \Delta \bar{t}}{A \sqrt{4\pi D_L \bar{t}}} \exp\left(-\frac{(U\bar{t} - U(t - \bar{t}))^2}{4D_L \bar{t}}\right)$$

$$C(x_2, t) = \int_{\bar{t}=-\infty}^{\infty} \frac{c(x_1, \bar{t}) U}{\sqrt{4\pi D_L \bar{t}}} \exp\left(-\frac{U^2(\bar{t} - t + \bar{t})^2}{4D_L \bar{t}}\right) d\bar{t} \quad (2.32)$$

where  $C_{(x_1, \bar{t})}$  = observed concentration as a function of time at location 1 ( $x_1$  in length);  
 $C_{(x_2, t)}$  = predicted concentration as a function of time at location 2 ( $x_2$  in length);  $\bar{t}$  =  
 integration variable on the time axis;  $\bar{t}_1, \bar{t}_2$  = mean times of passage at location 1 and 2  
 , obtained from field data, respectively, calculated by Equation 2.33.

$$\bar{t} = \bar{t}_2 - \bar{t}_1 \quad (2.33)$$

$$\bar{t}_1 = \frac{\int_{\bar{t}=-\infty}^{\infty} \bar{t} C(x_1, \bar{t}) d\bar{t}}{\int_{\bar{t}=-\infty}^{\infty} C(x_1, \bar{t}) d\bar{t}}$$

$$\bar{t}_2 = \frac{\int_{t=-\infty}^{\infty} t C(x_2, t) dt}{\int_{t=-\infty}^{\infty} C(x_2, t) dt}$$

when  $U$  = mean velocity as Equation 2.34.

$$U = \frac{x_2 - x_1}{\bar{t}_2 - \bar{t}_1} \quad (2.34)$$

According to Rutherford (1994), the longitudinal dispersion coefficient ( $D_L$ ) is linearly related to the spatial variance ( $\sigma_x^2$ ) in the equilibrium zone, where the variance of the



profile increases linearly with time. The relationship between the longitudinal dispersion and the variance is described in Equation 2.35.

$$D_L = \frac{1}{2} \frac{d\sigma_x^2}{dt} \quad (2.35)$$

Meanwhile, the spatial variance can be represented in terms of the temporal variance ( $\sigma_t^2$ ) as Equation 2.36 (Fischer, 1966).

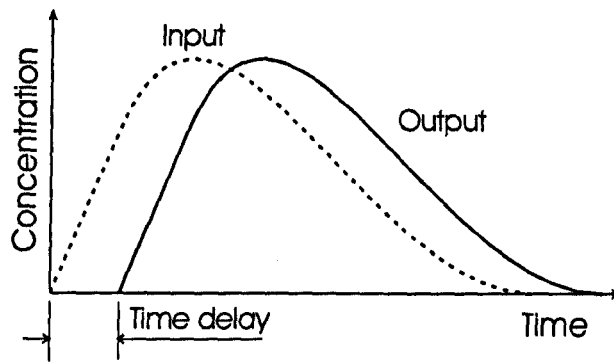
$$\sigma_x^2 = U^2 \sigma_t^2 \quad (2.36)$$

Therefore, the longitudinal dispersion coefficient ( $D_L$ ) in Equation 2.32 can be determined from Equation 2.35 and 2.36, which becomes Equation 2.37.

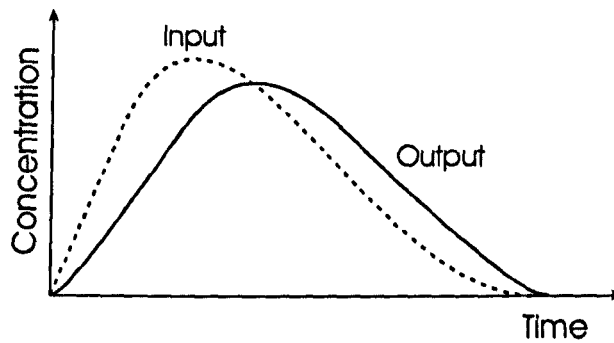
$$D_L = \frac{1}{2} U^2 \left( \frac{\sigma_t^2(x_2) - \sigma_t^2(x_1)}{t_2 - t_1} \right) \quad (2.37)$$

$$\sigma_t^2(x_j) = \frac{\int_{t=-\infty}^{\infty} (t - \bar{t}_j)^2 C(x_j, t) dt}{\int_{t=-\infty}^{\infty} C(x_j, t) dt}$$

## 2.9 Aggregated Dead Zone (ADZ)



(a) Plug flow reactor

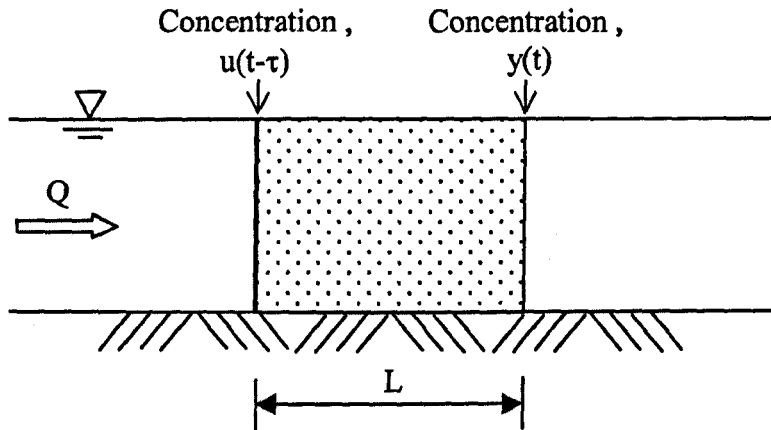


(b) Completely mixed reactor

**Figure 2.14** Influence of advection on the time delay at the onset of the output profile of two ideal reactors: (a) Plug flow reactor and (b) Completely mixed reactor

In general, mixing in a reactor can be described by 2 ideal processes, namely plug flow and complete mixing. The plug flow reactor presents a time lag or time delay ( $\tau$ ) due to pure advection process between the upstream and downstream concentration profiles as shown in Figure 2.14 (a), whereas the completely mixed reactor obtains the effect of instant mixing on the concentration profiles without a time delay in Figure 2.14 (b), for example.

The aggregated dead zone (ADZ) is a solute transport model, which describes the effect of delayed or plug flow storage. Beer and Young (1984) initiated an aggregated dead zone (ADZ) model for solute transport in a river. The model can be derived (Wallis, 1994) from the mass balance in a reach of a river as shown in Figure 2.15. An ADZ concept is assumed that the concentration of the solute at the downstream site depends on the solute concentration at the upstream site and the reach is extremely long,  $L$ .



**Figure 2.15** Solute mass balance for ADZ (after Wallis, 1994)

This solute mass balance is written as

$$\frac{d[V S(t)]}{dt} = Q u(t-\tau) - Q y(t) \quad (2.38)$$

where  $V$  = volume of water in the reach;  $S(t)$  = average solute concentration in the reach;  $Q$  = flow rate of water through the reach;  $u(t-\tau)$  = cross sectional average concentration at the upstream boundary;  $y(t)$  = cross sectional average concentration at the downstream boundary. Also, the steady flow and the volume of the reach are constant. Equation 2.38 is changed to be

$$\frac{dS(t)}{dt} = \frac{Q}{V} [u(t-\tau) - y(t)] \quad (2.39)$$

Moreover, the variable  $S(t)$  can be reduced by assuming that it is proportional to  $y(t)$ .

$$S(t) = \gamma y(t) \quad (2.40)$$

where  $\gamma$  is constant. The term  $Q/V$  can be presented as the travel time,  $\bar{t}$ , for the reach. Now, Equation 2.39 is substituted by Equation 2.40 and becomes

$$\frac{d y(t)}{dt} = \frac{1}{\gamma \bar{t}} [-y(t) + u(t - \tau)] \quad (2.41)$$

Equation 2.41 is the primary equation of the ADZ model. It also explains advection and diffusion processes of solute transport. The former process is represented by the time delay,  $\tau$ ; meanwhile, the latter is  $\gamma$  described for both advection and diffusion in terms of dispersive fraction. The dispersive fraction is also determined from the ratio of the residence time ( $T$ ) and travel time ( $\bar{t}$ ) where the residence time is the difference of the travel time and the time delay ( $\tau$ ). Then this relationship can be written as Equation 2.42.

$$\gamma = \frac{T}{\bar{t}} = \frac{\bar{t} - \tau}{\bar{t}} \quad (2.42)$$

Wallis (1994) and Green et al (1994) transformed Equation 2.41 to a simple discrete time term. Consequently, the concentration of tracer dye can be predicted by Equation 2.43.

$$y_k = -a y_{k-1} + b u_{k-\delta} \quad (2.43)$$

where  $a = -\exp(-\Delta t/T)$ ;  $b = 1 + a$ ;  $y_k$  = dye concentration downstream at time  $k\Delta t$ ;  $u_{k-\delta}$  = dye concentration upstream at  $(k-\delta)\Delta t$ ;  $\Delta$  = time step;  $T$  = residence time or  $\bar{t} - \tau$ ;  $\delta$  = integer value of  $\tau/\Delta t$ .

***ADZ in serial and parallel connections***

Equation 2.43 can be written in another form, z transfer function, for discrete data set. The  $z^{-1}$  operator is used to represent the relation between time series data. If there are series of data such as  $y_1, y_2, \dots, y_{k-1}, y_k$ , the last two data, for example, can be written as Equation 2.44.

$$\begin{aligned} y_{k-1} &= z^{-1} y_k & (2.44) \\ \text{or} \quad y_{k-i} &= z^{-i} y_k & \text{in general form.} \end{aligned}$$

So, Equation 2.43 can be reform as the following.

$$\begin{aligned} y_k &= -az^{-1} y_k + b u_{k-\delta} \\ y_k + az^{-1} y_k &= b u_{k-\delta} \\ y_k &= \frac{b}{1 + az^{-1}} u_{k-\delta} \end{aligned}$$

$$\text{When } u_{k-\delta} = z^{-\delta} u_k, \quad y_k = \frac{b z^{-\delta}}{1 + az^{-1}} u_k \quad (2.45)$$

where

$u_k$  = input data at position k

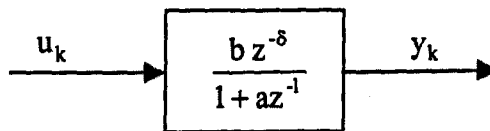
$y_k$  = output data at position k

$\delta$  = the number of the difference of the first input and output positions

a, b = constant

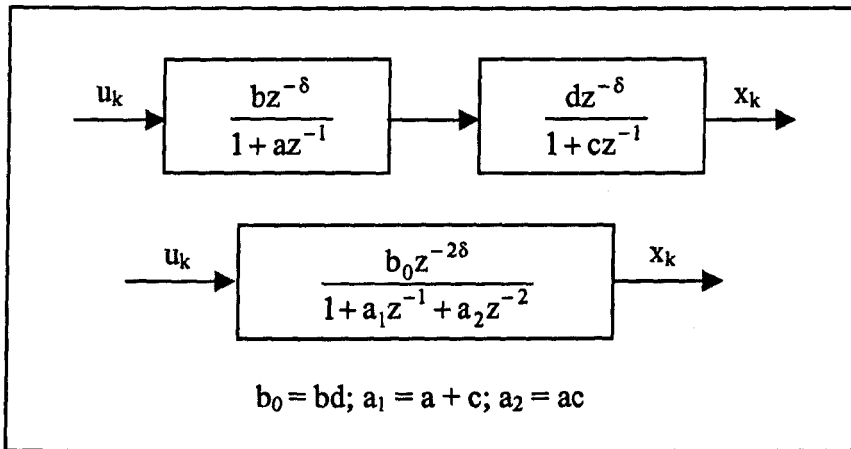
$z^{-1}$  = operator for backward-shift transfer function.

Equation 2.45 is also called as “first-order transfer function” and presented as a block diagram as shown in Figure 2.16.

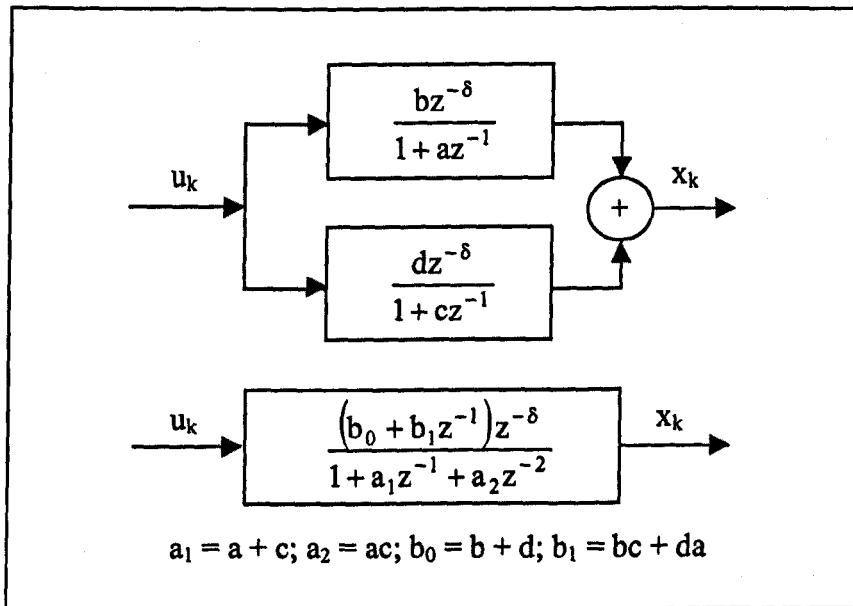


**Figure 2.16** Block diagram of first order transfer function

Young and Lees (1993) and Lees et al (2000) presented the higher order transfer function in terms of serial and parallel connections of the first order transfer function. For instance, Figure 2.17 (a) illustrates two first order transfer functions connecting together in a series. The output of the 2 blocks above is equally the result of the longer block. Similarly, the output of connection of two parallel first order can be represented as its longer block in Figure 2.17 (b).



(a) serial connection



(b) parallel connection

**Figure 2.17** Serial and parallel connection of first order transfer function models (after Young, 1992)

Then, the typical format of the equation in the longer block diagram can be written as Equation 2.46.

$$y_k = \frac{B(z^{-1})}{A(z^{-1})} u_{k-\delta} + e_k \quad (2.46)$$

where  $A(z^{-1}) = 1 + a_1 z^{-1} + \dots + a_n z^{-n}$

$B(z^{-1}) = b_0 + b_1 z^{-1} + \dots + b_m z^{-m}$

$z^{-1} x_k = x_{k-1}$

$y_k$  = downstream concentration at time  $k\Delta t$

$u_k$  = upstream concentration at time  $k\Delta t$

$e_k$  = white noise function at time  $k\Delta t$ .

Young (2002) applied the higher order transfer function of ADZ model to determine residence time for tracer dye in a Florida wetland. Bromide tracer dye was injected at 765 m upstream of a weir, in which samples were collected at every 2 hours. The order of the transfer function to effectively predict the downstream dye concentration profile was either 3<sup>rd</sup> or 4<sup>th</sup>, but the latter order seemed to be more suitable in this case because the decomposition of  $A(z^{-1})$  term in Equation 2.46 obtained all 4 real eigenvalues, for this example. Therefore, the finest model for the prediction was determined as [4, 2, 22] that means the model comprising 4<sup>th</sup> order denominator,  $A(z^{-1})$ ; 2<sup>nd</sup> order numerator,  $B(z^{-1})$ ; and a 22 sampling interval time delay,  $\delta$ . Then, the transfer function model can be written as Equation 2.47 with the format of Equation 2.46 by ignoring a very small value of  $e_k$ .

$$y_k = \frac{B(z^{-1})}{A(z^{-1})} u_{k-22} \quad (2.47)$$

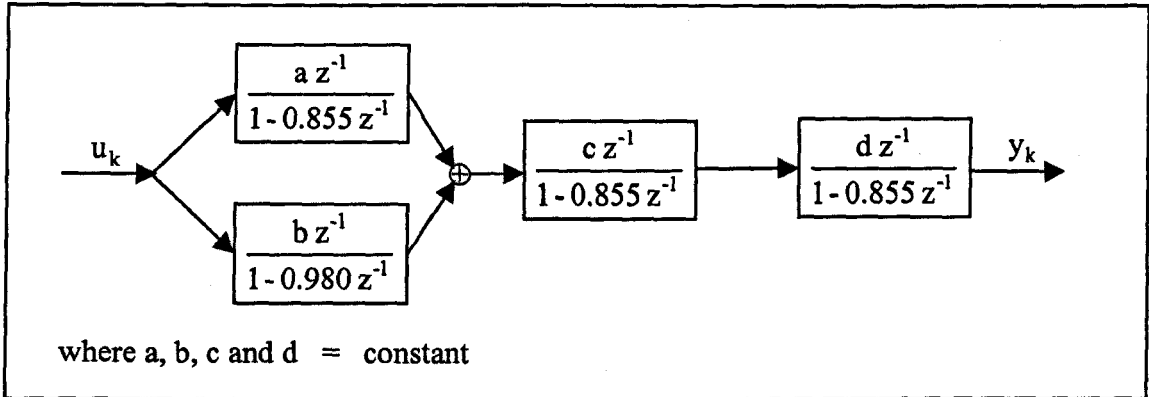
where

$A(z^{-1}) = 1 - 3.67 z^{-1} + 5.06 z^{-2} - 3.11 z^{-3} + 0.72 z^{-4}$

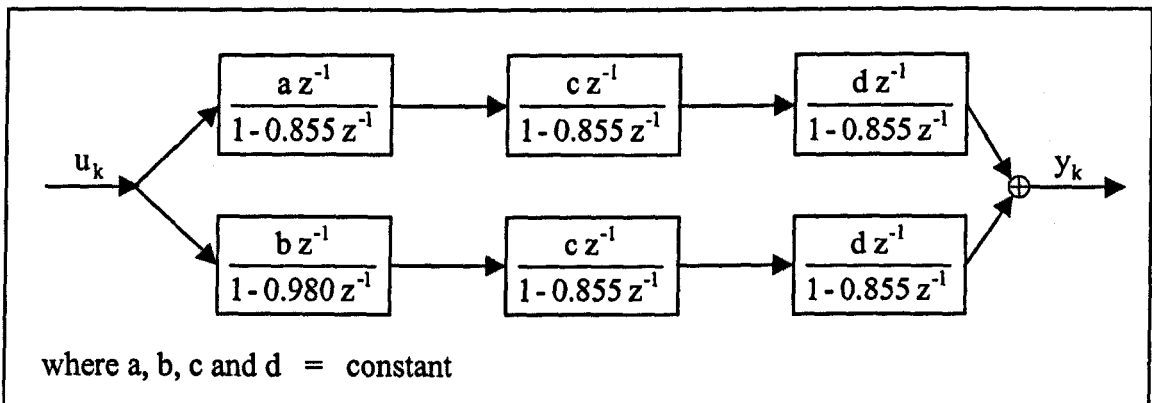
$B(z^{-1}) = 0.00103 - 0.00101 z^{-1}$

or  $A(z^{-1}) = (1 - 0.980 z^{-1})(1 - 0.855 z^{-1})^3$  after the decomposition

Subsequently, Equation 2.47 can be described in terms of 4 blocks joined with parallel and serial connection of first order transfer function as shown in Figure 2.18 (a) and (b), which are identical in terms of the value of transfer function decomposition.



(a)



(b)

**Figure 2.18** Block diagram of transfer function decomposition: (a) equivalent parallel-serial decomposition and (b) fully parallel decomposition

According to Lees et al (2000), the residence time for each block of first order transfer function in Figure 2.18 (b), for example, is determined by Equation 2.48. The calculated residence time is presented with the description of quick and slow flow when the residence time was small and great respectively in Figure 2.19.

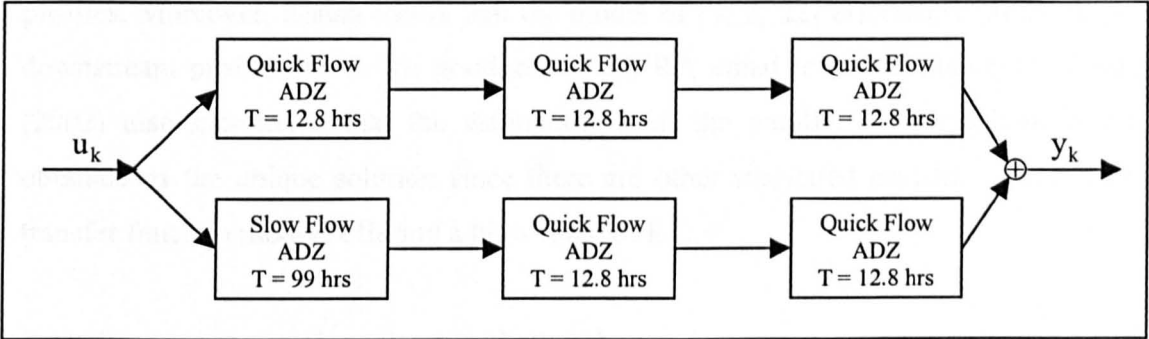
$$T = -\frac{\Delta t}{\ln(-a)} \quad (2.48)$$



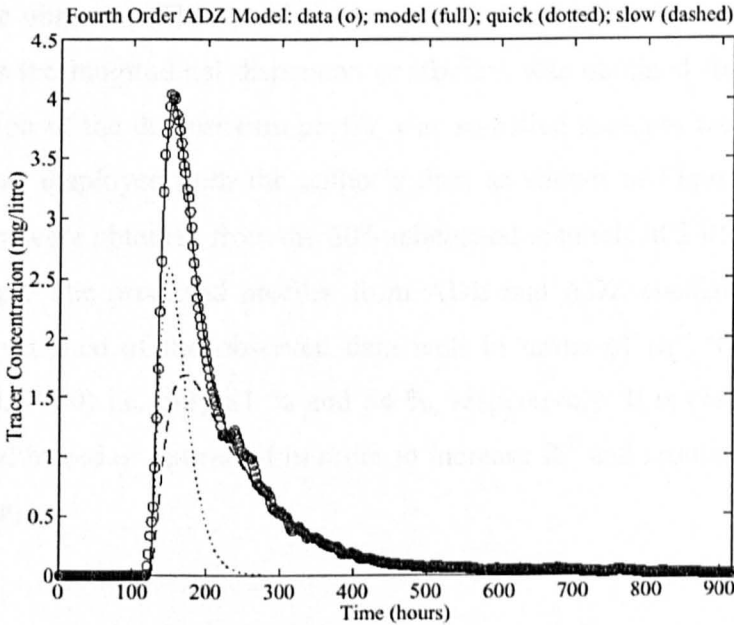
where

$a$  = coefficient of  $z^{-1}$  in denominator, i.e.  $-0.855$  and  $-0.980$

$\Delta t$  = 2 hrs in this case



**Figure 2.19** Residence time for quick and slow flow (after Young, 2002)

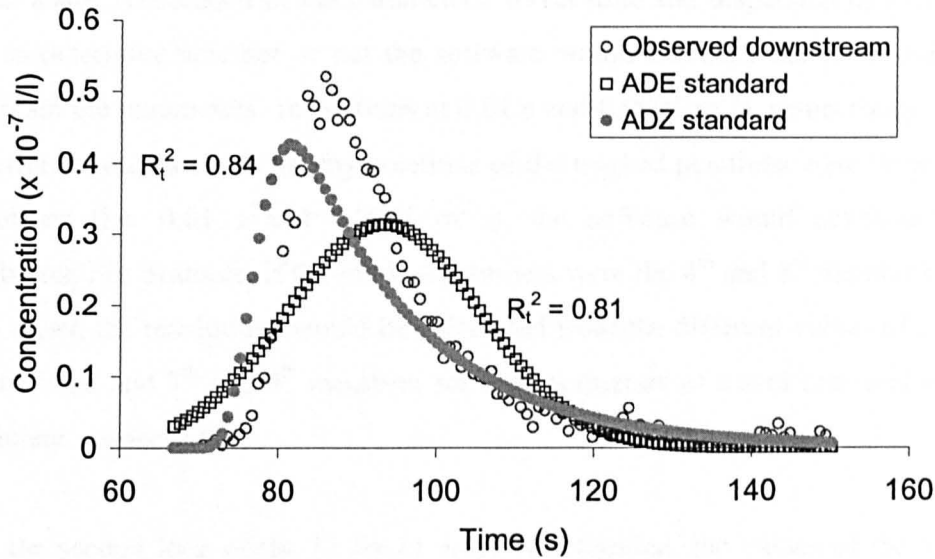


**Figure 2.20** Simulated profile (full line), decomposed into quick flow (dotted line) and slow flow (dashed line), and compared to observed profile (circular points) (after Young, 2002)

The two figures of the residence time were applied to simulate 2 downstream profiles concerning quick and slow flow rates in Figure 2.20. Then, the observed data profile is compared to the simulated profile from the fourth order transfer function of ADZ model, which can be decomposed into two profiles, namely quick flow and slow flow profiles. Moreover, it also shows that the model of [4, 2, 22] effectively predicted the downstream profile due to the goodness of fit,  $R_t^2$ , equal to 0.997. However, Young (2002) also mentioned that the estimation from the parallel decomposition is not obtained as the unique solution since there are other simulated profiles from several transfer function models offering a high value of  $R_t^2$ .

## 2.10 Parameter estimation/optimisation

O'Brien (2000) and Dennis (2000) determined parameters, such as travel time ( $\bar{t}$ ), longitudinal dispersion coefficient ( $D_L$ ) for ADE model, and travel time and reach time delay ( $\tau$ ) for ADZ model after an upstream and downstream temporal concentration profiles were observed. The travel time was calculated by means of the first moment area whereas the longitudinal dispersion coefficient was obtained from Equation 2.37. This prediction of the downstream profile was so-called standard technique. Also, this technique was employed with the author's data as shown in Figure 2.21, where the observed data were obtained from the 60°-unbenched manhole at 2 l/s flow rate and 176 mm surcharge. The predicted profiles from ADE and ADZ standard models did not explain the variance of the observed data well in terms of  $R_t^2$ , the goodness of fit (Young et al, 1980) i.e. only 81 % and 84 %, respectively. It is clear that the models need to be calibrated or optimised in order to increase  $R_t^2$  and reduce noise from signal data collection.



**Figure 2.21** Predicted downstream profiles from ADE and ADZ standard from the 60°-unbenched manhole at 2 l/s flow rate and 176 mm surcharge

Dennis (2000) optimised the prediction of the observed data from stepped manholes for these two models, ADE and ADZ, by means of a trial and error technique. For ADE, the estimated parameters were travel time and longitudinal dispersion coefficient, whereas travel time and reach time delay were analysed for the ADZ model. A FORTRAN programme was coded to estimate and calibrate these two parameters for these two models. Since the same concept was used to optimise the parameters from ADE and ADZ, only the algorithm of ADE optimisation is described as the following sample.

#### ***Algorithm for ADE optimisation***

Dennis (2000) introduced the optimisation method by trial and error with the advection dispersion equation (ADE). The developed program would initiate the series of travel time ( $\bar{t}$ ) and dispersion coefficient ( $D_L$ ) on an 11 by 11 array. Each pair of the array values was taken to predict the temporal downstream profile. So, at this first iteration of the calculation, there would be 121 downstream profiles produced in total; also each was compared to the observed downstream profile and reported in terms of  $R_t^2$ , the goodness of fit (Young et al, 1980) as shown in Equation 2.49. The set of 121  $R_t^2$  would be sorted to collect the best fit to the observed downstream profile. Then, the positions of the members of the arrays giving the best  $R_t^2$  would be marked.

At this stage, resolutions of the parameters: travel time and dispersion coefficient were used to determine whether or not the software would calculate the next loop. Dennis (2000) set the parameters' resolutions at 0.01 s and 0.0001 m<sup>2</sup>/s, respectively. Hence, if the different values of the nearby positions of the marked positions were larger than the resolutions (i.e. 0.01 s and 0.0001 m<sup>2</sup>/s), the software would continue the next calculation. For example, if the marked members were the 4<sup>th</sup> and 8<sup>th</sup> members of the 11 by 11 array, the resolutions would be calculated from the different values of the 3<sup>rd</sup> and 5<sup>th</sup> members, and 7<sup>th</sup> and 9<sup>th</sup> members for the parameters of travel time and dispersion coefficient, respectively.

Once the second loop of the 11 by 11 array was decided, the values of the 5<sup>th</sup> and 7<sup>th</sup> members would become the values of the 1<sup>st</sup> and 11<sup>th</sup> members of the travel time array for calculating the next loop; similarly, the values of the 7<sup>th</sup> and 9<sup>th</sup> would be installed in the 1<sup>st</sup> and 11<sup>th</sup> the dispersion coefficient array, for this example. Next, the values of the others (i.e. the 2<sup>nd</sup>, 3<sup>rd</sup>, ..., 10<sup>th</sup>) would be linearly interpolated between the values of the 1<sup>st</sup> and 11<sup>th</sup> members. Then, the values of all members were used to generate another 121 predicted downstream profiles. The generated profiles would be compared with the observed profile to collect the other 121  $R_t^2$  and the best pair of the arrays giving the best  $R_t^2$  would be marked again.

Then resolutions of both the travel time and the dispersion coefficient from the values of the nearby marked positions were calculated. If such resolutions were accepted (i.e. less than 0.01 s and 0.0001 m<sup>2</sup>/s for travel time and dispersion coefficient, respectively, for this case), the suitable travel time and dispersion coefficient to predict the downstream profile should be the values, which offer the best  $R_t^2$ . If not, the next loop or iteration should be calculated until the resolutions of both the travel time and dispersion coefficient were achieved.

$$R_t^2 = 1 - \left[ \frac{\sum_{t=1}^n (C_t - P_t)^2}{\sum_{t=1}^n C_t^2} \right] \quad (2.49)$$

where  $C_t$  and  $P_t$  = observed and predicted solute concentration at time  $t$ .

This optimisation technique can improve  $R_t^2$  until close to 1.0 for some observed events, while  $R_t^2$  of the rest insufficiently increased because the dispersion coefficient was not constant during the travel time period. This unstable dispersion coefficient was above the limit of Equation 2.32 in that the longitudinal dispersion coefficient should be constant. The improvement of  $R_t^2$  for ADE and ADZ standard in Figure 2.21 by the optimisation technique is shown with its error in Figure 2.22. The figures of  $R_t^2$  significantly increase from 0.81 to 0.94 for ADE model and from 0.84 to 0.99 for ADZ model.

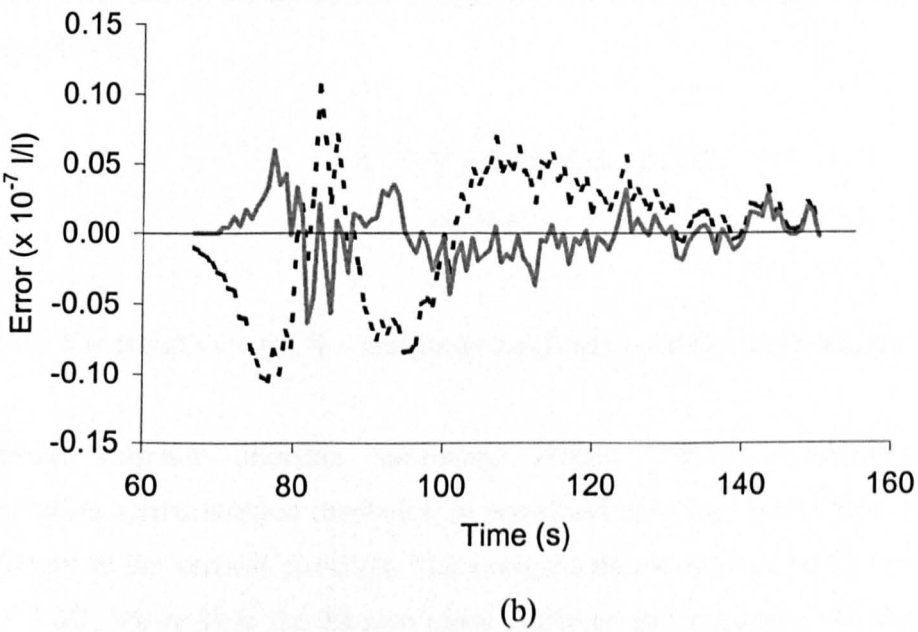
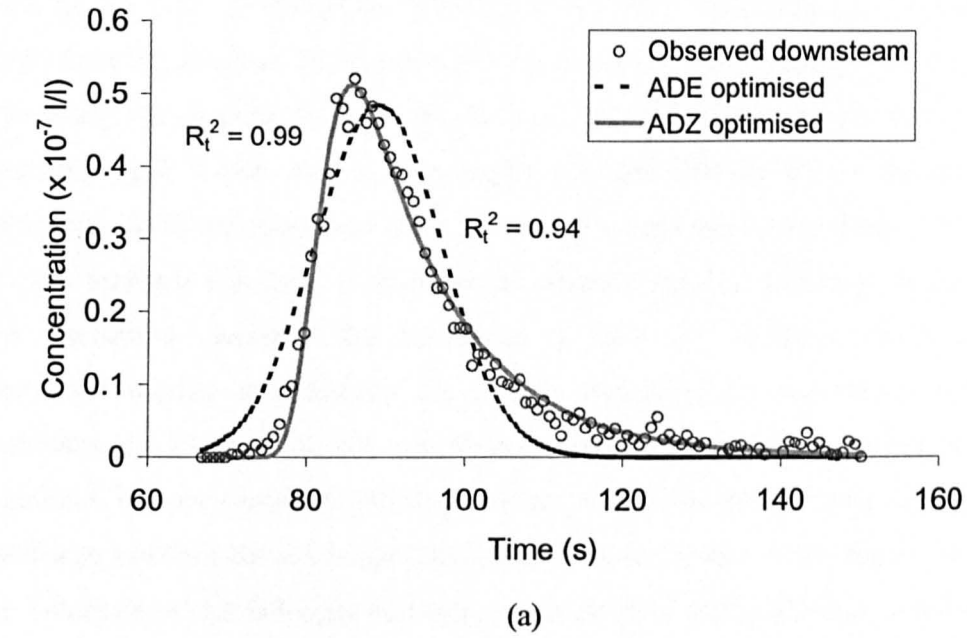
## 2.11 Previous work on longitudinal dispersion and its relationships

Guymer and O'Brien (2000) studied the effect of longitudinal dispersion across a manhole compared to a straight pipe. The investigation was done on a 500 mm diameter manhole with 88 mm diameter inlet and outlet pipes. Consequently, travel time and reach time delay, mechanisms in solute mixing, determined by ADE and ADZ models were significantly related to flow rate and are presented by the equations in Table 2.6. Moreover, when the surcharge effect was combined, the longitudinal dispersion coefficient of the manhole could increase fivefold compared with that of the straight pipe.

**Table 2.6** Predicted variation of dispersion parameters from manhole and pipe data (after Guymer and O'Brien, 2000)

Parameter	Pipe	Manhole
<b>ADE</b>		
Travel time (s)	$15.5 \times 10^{-3} Q^{-1.007}$ ( $R^2 = 0.996$ )	$13.8 \times 10^{-3} Q^{-1.053}$ ( $R^2 = 0.999$ )
Dispersion coefficient ( $m^2/s$ )	$3.3 Q$ ( $R^2 = 0.745$ )	$18.6 Q + 0.0257$ ( $R^2 = 0.838$ )
<b>ADZ</b>		
Travel time (s)	$18.0 \times 10^{-3} Q^{-0.985}$ ( $R^2 = 0.997$ )	$16.4 \times 10^{-3} Q^{-1.055}$ ( $R^2 = 0.992$ )
Reach time delay (s)	$17.0 \times 10^{-3} Q^{-0.971}$ ( $R^2 = 0.993$ )	$11.8 \times 10^{-3} Q^{-1.055}$ ( $R^2 = 0.996$ )

Note: Q is flow rate ( $m^3/s$ )



**Figure 2.22** Predicted downstream profiles from the 60°-unbenched manhole at 2 l/s flow rate and 176 mm surcharge: (a) ADE and ADZ optimised and (b) Error of ADE and ADZ optimised from the observed downstream profile

Since manholes affect solute dispersion in a sewer network, the framework to quantify such an amount has been investigated at some physical configurations of manholes, such as the ratio of diameters of manhole and pipe, pipe direction and floor types. Guymer et al (accepted 2002) presented the effect of solute transport across surcharged manholes, whose diameter was varied from 400, 500, 600 and 800 mm with 88 mm diameter pipes. Tracer studies were tested with Rhodamine WT, a fluorescent solute substance. ADZ technique was used to determine both reach time delay and travel time in each manhole diameter. It consequently showed that the degree of solute mixing in the surcharged manholes did not relate to flow rate as an intrinsic assumption. Dominant mixing mechanisms are clearly depended on surcharge levels in the manholes. At the 600 and 800 mm diameter manholes, there seemed to be surcharge threshold. For pre-surge threshold values, travel time has a linear relationship with surcharge and for post-surge threshold, it is independent of surcharge. For example, the threshold of the 800 mm manhole was located at about 225 mm surcharge. Then, travel time can be predicted from Equation 2.50 and 2.51 for pre- and post-thresholds, respectively.

$$\bar{t} = (1 + 27.51S) 0.0165/Q \quad (2.50)$$

$$\bar{t} = 0.0165/Q \quad (2.51)$$

where  $\bar{t}$  = travel time (s),  $S$  = surcharge level (mm) and  $Q$  = flow rate ( $m^3/s$ ).

Besides manhole diameter variations, Dennis (2000) investigated longitudinal dispersion across stepped manholes, in which the inlet and outlet pipe centre lines are different in the vertical direction. The study examined steps of 0.0D, 0.5D, 1.0D, 1.5D and 2.0D, where D is the 88 mm pipes diameter. Subsequently, Rhodamine WT was injected and temporal concentration distributions recorded before and after the 388 mm diameter manhole. The comprehensive data were analysed by means of ADZ optimisation technique. The results were presented in terms of reach time delay and travel time. Due to the lack of threshold surcharge on this study, either reach time delay or travel time can be estimated directly over reciprocal flow rate as shown in the equations in Table 2.7.

**Table 2.7** Averaged reach time delay and travel time for stepped manholes  
(after Dennis, 2000)

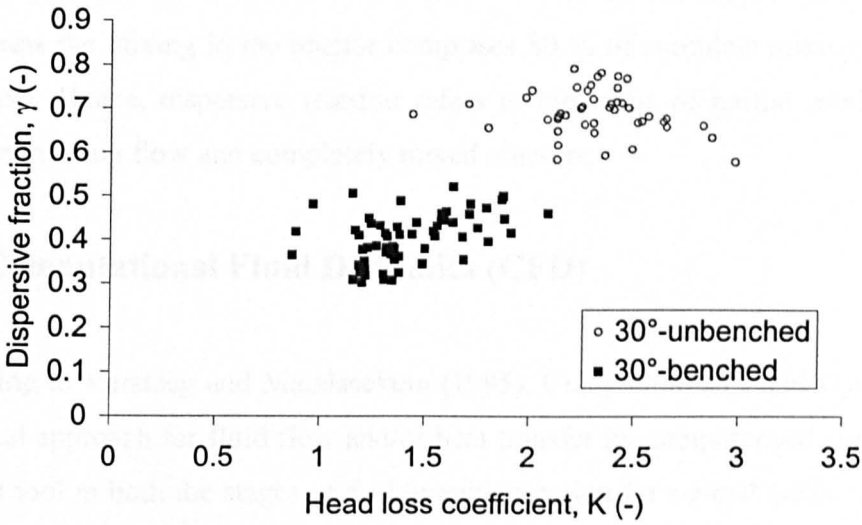
Averaged parameters	0.0D	0.5D	1.0D	1.5D	2.0D
Reach time delay (s)	$0.020Q^{-0.915}$ ( $R^2 = 1.000$ )	$0.015Q^{-0.922}$ ( $R^2 = 1.000$ )	$0.015Q^{-0.901}$ ( $R^2 = 0.999$ )	$0.016Q^{-0.904}$ ( $R^2 = 0.997$ )	$0.016Q^{-0.902}$ ( $R^2 = 1.000$ )
Travel time (s)	$0.024Q^{-0.936}$ ( $R^2 = 1.000$ )	$0.039Q^{-0.915}$ ( $R^2 = 0.999$ )	$0.055Q^{-0.936}$ ( $R^2 = 1.000$ )	$0.060Q^{-0.956}$ ( $R^2 = 0.999$ )	$0.092Q^{-0.908}$ ( $R^2 = 1.000$ )

where Q is flow rate ( $m^3/s$ )

From previous work on dispersion in manholes, as mentioned before, there was not an investigation on solute dispersion due to a manhole, whose pipes change in plane angle, yet. Hence, this study “Effect of changes in pipe direction across surcharged manholes on dispersion and head loss” had been performed to quantify the effect. Also hopefully, it would be beneficial to urban drainage software with regard to quality pollution control.

Apart from the benefit to the software in terms of the water quality, the qualified parameters from ADZ can help to illustrate the relationship between dispersion and head losses. More importantly, it might be a key to convert the value of dispersion to the head loss or vice versa. Dennis (2000) presented an attractive linear regression of dispersive fraction and head loss coefficient for the stepped manholes. Submerged jet was claimed as a key process to describe this correlation. Also, Saiyudthong and Guymer (2002) made an effort to present the correlation of dispersive fraction and head loss coefficient for the benched/unbenched manholes with  $30^\circ$  pipe plane angle. The data is shown in Figure 2.23. It is quite clear that dispersion and head loss are correlated for each other as they are the consequences of the same laws of fluid motion, i.e. mass conservation, momentum conservation and submerged jet theory, occurring within the manholes.





**Figure 2.23** Relationship between dispersive fraction and head loss coefficient

**2.12 Reactor mixing**

“The sewer as a Physical, Chemical and Biological Reactor” had been the title of Water Science and Technology published in the first edition of 1998. Most papers in the issue were concerned with biofilm, sewer solid sediment transport and solid mixing with free flow condition. Yet, what kind of a reactor (sewer) is in terms of mixing has not been investigated, especially under surcharge condition.

If a manhole was looked as a reactor, dispersive fraction might be utilised to describe partial mixing within the reactor. Dispersive fraction ( $\gamma$ ) from ADZ model is defined as a ratio of residence time ( $T$ ) over travel time ( $\bar{t}$ ). In general, there are only two ideal reactors, namely plug flow and completely mixed reactors, used to determine the characteristic mixing of a reactor. Figure 2.24 shows dispersive fraction between the upstream and downstream concentration profiles, which are subscribed by “1” and “2” respectively to refer to these profiles later. Figure 2.24 (a) displays the dispersive fraction of 0 from the plug flow reactor, in which residence time from the upstream ( $T_1$ ) and down stream ( $T_2$ ) concentration profiles are identical. On the other hand, Figure 2.24 (b) illustrates the completely mixed reactor, whose dispersive fraction is equal to 1 (Wallis, 1994). It is the product of two concentration profiles obtained from the equal values of the residence time ( $T = T_2 - T_1$ ) and travel time ( $\bar{t}$ ). These two theoretical

reactors have not been seen in natural reactors. Yet, they are used as references in describing general reactors. For example, if a reactor has the dispersive fraction of 0.8, that means the mixing in the reactor comprises 80 % of complete mixing and 20 % of plug flow. Hence, dispersive fraction refers to the value of partial mixing, which is between the plug flow and completely mixed reactors.

## 2.13 Computational Fluid Dynamics (CFD)

According to Versteeg and Malalasekera (1995), Computational Fluid Dynamics is the analytical approach for fluid flow and/or heat transfer by computerised simulation. It is a robust tool in both the stages of design and operation for several areas, such as flows in rivers, estuaries and ocean; chemical mixing; distribution of pollutants.

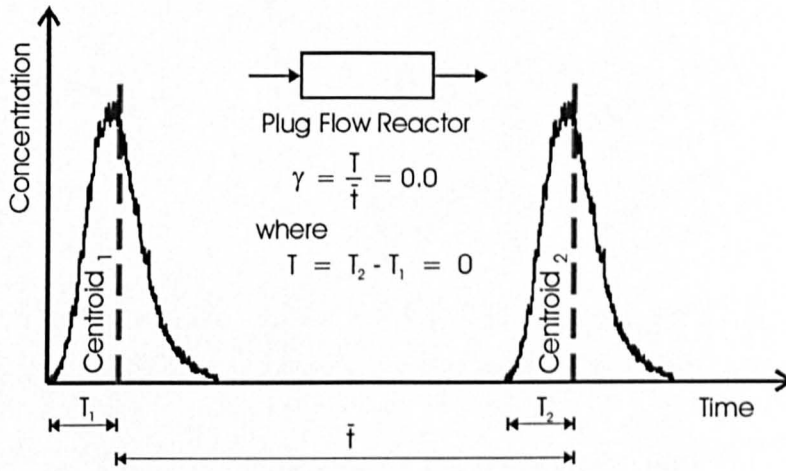
CFD software, in general, consists of 3 main units: pre-processor, solver and post-processor. The preprocessing unit is to input data such as the geometry of the body of a model, meshing the body, physical and chemical properties, and boundary conditions. For the solving unit, most CFD applications employ the finite volume as the numerical method to study the rate of change of a general variable per unit of time. Afterwards, the output unit, postprocessor, is shown graphically in terms of vector or contour for both 2 and 3 dimensions.

### 2.13.1 Governing equations

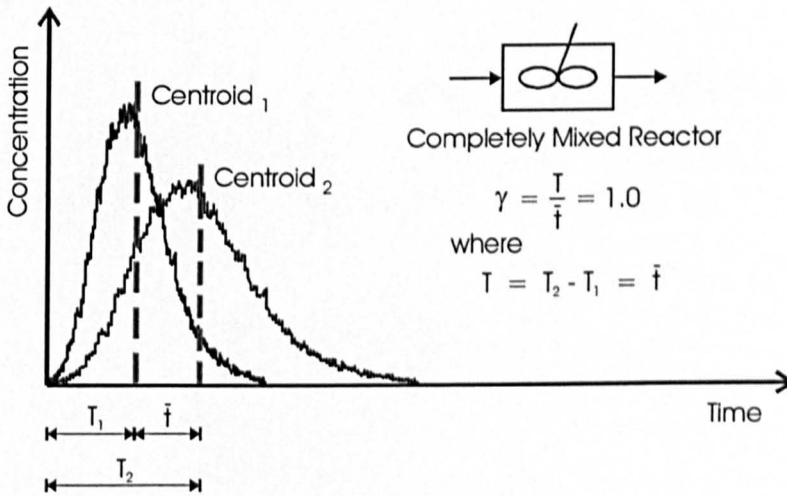
For incompressible fluid, CFD technique for fluid flow is governed by mass conservation and momentum conservation equations (Versteeg and Malalasekera,1995).

#### *Mass conservation*

$$\frac{\partial u_x}{\partial x} + \frac{\partial u_y}{\partial y} + \frac{\partial u_z}{\partial z} = 0 \quad (2.52)$$



(a)



(b)

**Figure 2.24** Dispersive fraction ( $\gamma$ ) describing partial mixing with reference to two theoretical reactors: (a) Plug flow reactor and (b) Completely mixed reactor, where 1 and 2 stand for upstream and downstream;  $T$  and  $\bar{t}$  denote residence time and travel time, respectively

**Momentum conservation**

$$\frac{\partial u_x}{\partial t} + u_x \frac{\partial u_x}{\partial x} + u_y \frac{\partial u_x}{\partial y} + u_z \frac{\partial u_x}{\partial z} = -\frac{1}{\rho} \frac{\partial p}{\partial x} + \frac{\mu}{\rho} \left( \frac{\partial^2 u_x}{\partial x^2} + \frac{\partial^2 u_x}{\partial y^2} + \frac{\partial^2 u_x}{\partial z^2} \right) \quad (2.53)$$

$$\frac{\partial u_y}{\partial t} + u_x \frac{\partial u_y}{\partial x} + u_y \frac{\partial u_y}{\partial y} + u_z \frac{\partial u_y}{\partial z} = -\frac{1}{\rho} \frac{\partial p}{\partial x} + \frac{\mu}{\rho} \left( \frac{\partial^2 u_y}{\partial x^2} + \frac{\partial^2 u_y}{\partial y^2} + \frac{\partial^2 u_y}{\partial z^2} \right) + g \quad (2.54)$$

$$\frac{\partial u_z}{\partial t} + u_x \frac{\partial u_z}{\partial x} + u_y \frac{\partial u_z}{\partial y} + u_z \frac{\partial u_z}{\partial z} = -\frac{1}{\rho} \frac{\partial p}{\partial z} + \frac{\mu}{\rho} \left( \frac{\partial^2 u_z}{\partial x^2} + \frac{\partial^2 u_z}{\partial y^2} + \frac{\partial^2 u_z}{\partial z^2} \right) \quad (2.55)$$

where  $u_x$ ,  $u_y$  and  $u_z$  = the velocity in x, y and z directions, respectively;  $\rho$  = density;  $\mu$  = dynamic viscosity;  $p$  = pressure; and  $g$  = gravitational acceleration, here in y direction.

Equation 2.53, 2.54 and 2.55 are referred to as Navier-Stokes equations.

**2.13.2 Turbulence models**

To deal with the turbulent flow, several models have been constructed for CFD. But the most popular one is k- $\epsilon$  modelling. "k- $\epsilon$ " stands for turbulent kinetic energy and turbulent energy dissipation rate, respectively.

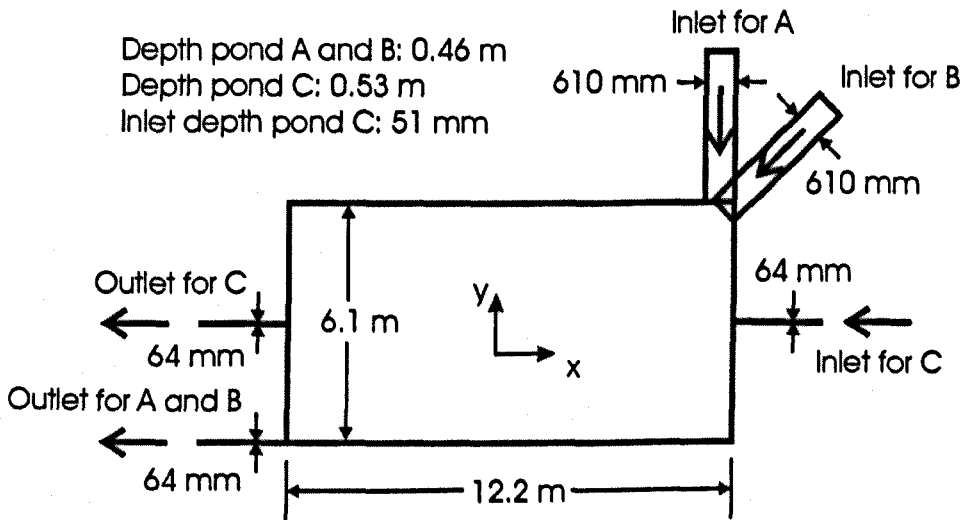
$$k = \frac{1}{2} \left( \overline{u_x^2} + \overline{u_y^2} + \overline{u_z^2} \right)$$

$$\epsilon = \frac{k}{\text{time}}$$

**2.13.3 Previous work**

Wood et al (1998) published 2-D CFD models for waste stabilisation ponds (WSP). Since the failure of WSP performance was mainly caused by hydrodynamic problems, the CFD model might be a tool to design and operate the ponds in terms of experimental parameters of tracer study. Experimental residence time distributions (RTD) from Mangelson and Watters (1972) were compared to simulated RTD with pond configurations in Figure 2.25 and Table 2.8. Similarity models of geometry and velocity were investigated and presented in cases A-1, B-1 and C1, and A-2, B2 and C2, respectively. The features of case A-1 were 610 mm inlet width, 610 mm outlet width,

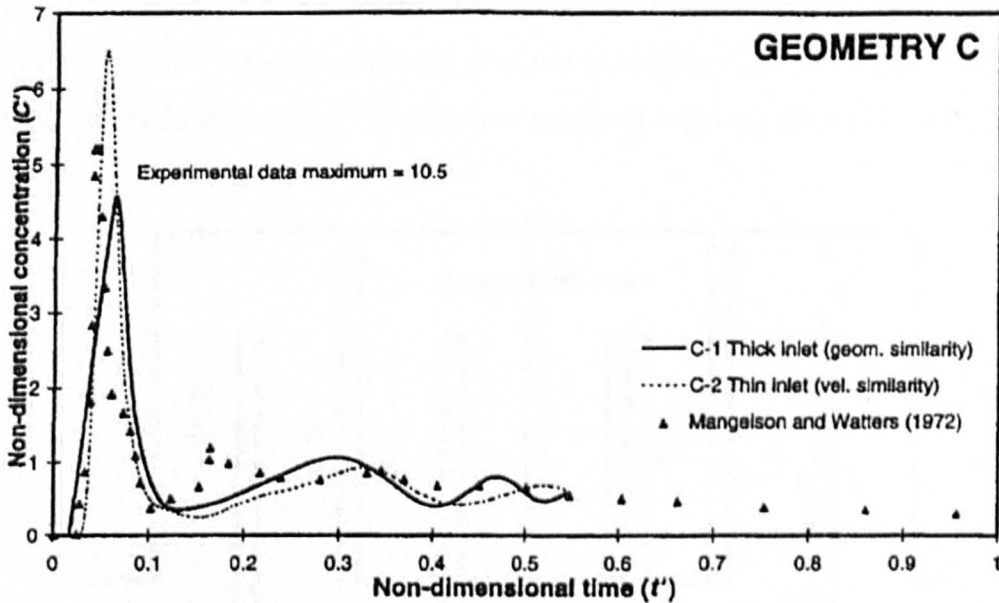
and  $-0.018$  m/s inlet velocity in y direction, for example. The 2-D CFD models were simulated by the commercial finite element package FIDAP (Fluid Dynamics International Inc.) with steady state velocity and the k- $\epsilon$  turbulence model. Then, a tracer residence time distribution was determined from the dynamic advection/diffusion of a second species with identical properties to the fluid and a molecular diffusion coefficient of  $1.0 \times 10^{-9}$  m<sup>2</sup>/s by a transient simulation. Tracer dye of 1 kg/m<sup>3</sup> Rhodamine WT was injected into the transient CFD simulation for an 100 s interval. For the simulation results, only case C could predict the RTD well, compared to the experimental RTD as shown in Figure 2.26. This was because the small difference in geometric and velocity similarity in case C based on the inlet width and fluid velocity, whereas the simulation for case A and B failed due to the difficulty of representing a 3-D inlet in a plane, i.e. the pipe depth would be equal to the depth of ponds. Therefore, 3-D CFD models could be successful to simulate RTD, rather than 2-D models (Wood et al, 1998).



**Figure 2.25** Plan of pond configurations (after Mangelson and Watters, 1972)

**Table 2.8** RTD curves for geometry C (after Wood et al, 1998)

Parameter	CFD simulation case					
	A-1	A-2	B-1	B-2	C-1	C-2
Inlet width (mm)	610	64	610	64	64	51
Outlet width (mm)	610	610	610	610	64	64
Inlet velocity in x direction (m/s)	0	0	-0.013	-0.123	-0.143	-0.186
Inlet velocity in y direction (m/s)	-0.018	-0.174	-0.013	-0.123	0	0

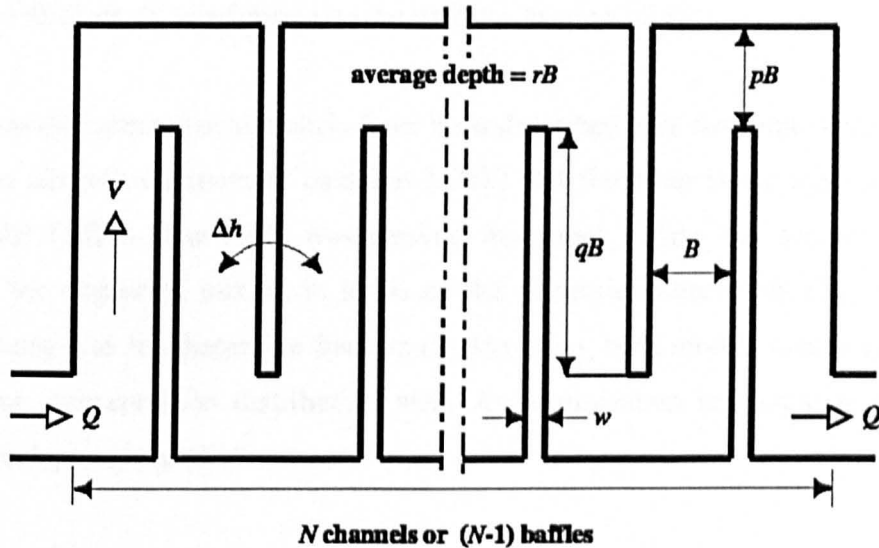


**Figure 2.26** Simulated and observed RTD curves (after Wood et al, 1998)

Besides the simulated RTD from Wood et al (1998), Haarhoff and Walt (2001) suggested that CFD was a useful tool to optimise design parameters for around-the-end hydraulic flocculators as shown in Figure 2.27, where  $N$  is a number of channels or a number of baffles equal to  $N-1$ ;  $B$  is the channel width between baffles;  $p$  is the slot width ratio with respect to  $B$ ;  $q$  is the overlap ratio with respect to  $B$ ; and  $w$  is the baffle thickness. Three parameters, such as slot width ratio ( $p$ ), overlap ratio ( $q$ ) and depth ratio ( $r$ ), of geometrical ratios were optimised  $G$ -value calculated by CFD software.  $G$ -value, an indicator to determine floc breakup, is the degree of variability in energy dissipation as described in Equation 2.56. The  $\varepsilon$  in the equation was simulated from the Navier-Stokes equation and the  $k$ - $\varepsilon$  turbulence model by Flo++ (a CFD software developed at the Potchefstroom University for CHE, South Africa). The simulated model showed that low slot width ratio ( $p$ ) caused greater  $G$ -value than high width ratio did. Moreover, the slot width ratio seemed to be the most important parameter, compared to the others, to design an around-the end flocculator, which is simply, robustly maintained and widely used in most part of the world.

$$G = \sqrt{\rho \frac{\varepsilon}{\mu}} = \sqrt{\frac{g\Delta H}{\nu t}} \quad (2.56)$$

where  $\rho$  = density of water ( $1000 \text{ kg/m}^3$ );  $\varepsilon$  = Dissipation rate of turbulent kinetic energy ( $\text{m}^2/\text{s}^3$ );  $\mu$  = Dynamic viscosity of water ( $1.0 \text{ kg/m-s}$ ); gravitational acceleration ( $\text{m/s}^2$ );  $\Delta H$  = head loss (m);  $\nu$  = kinematic viscosity of water ( $\text{m}^2/\text{s}$ ); and  $t$  = time (s).



**Figure 2.27** Parameter layout of an around-the-end hydraulic flocculator (after Haarhoff and Van der Walt, 2001)

## 2.14 Summary

To carry either sanitary or storm sewage to wastewater treatment plants or receiving waters, sewer system should be suitably designed for each catchment area. Such an amount and quality of the sewage can be determined from size, shape, soil and pavement types, water table levels and land use, for example, of that area. In the past, the sewer network was calculated to transport the wastewater under free surface flow condition, not for surcharge; meanwhile, the sewerage quality was not considered. Recently, the ability of personal computers (PC) have been greatly improved to simulate and predict both the flow rate and the pollution transport in sewer system under pressured flow. Therefore, the knowledge on energy losses and transport processes in the surcharged sewer system has investigated, especially in manholes, where more supported data are needed for the prediction, compared to sewer pipes.

---

Unlike the majority of friction losses in pipes, the losses due to manhole are caused by momentum movement and well-known as “minor losses”. In practice, it can be measured directly from the difference of the upstream and downstream hydraulic grade lines at the manhole centre. To formulate this, the losses ( $\Delta H$ ) are presented as equal to the loss coefficient ( $K$ ) multiplied by the velocity head ( $V^2/2g$ ).

Two important mathematical models have been described here for solute transport. The first is the advection dispersion equation (ADE) and the other is the aggregated dead zone model (ADZ). The ADE was derived from Fick’s first and second laws and describes the degree of mixing in terms of the dispersion coefficient ( $D_L$ ) while the ADZ presents it as the dispersive fraction ( $\gamma$ ). However, both models cannot predict the downstream concentration distribution well. An optimisation technique is needed to increase such precise prediction.

Due to lack of parameters to design and operate reactors, engineers and scientists attempt to obtain that from computer simulation. Computational Fluid Dynamics (CFD) is an approach to describe flow patterns in the reactors. It applies several equations, such as mass conservation equation, momentum conservation equation, advection diffusion equation and turbulence models, to determine the crucial parameters. Nevertheless, the simulated results should be validated with observed data to increase reliability for later implementation.



---

## Chapter 3

# Experimental work

Solute transport and dispersion due to manholes have been investigated in the Department of Civil and Structural Engineering, the University of Sheffield since 1994. The experimental work has been developed continuously. Software has been developed to obtain the precise analysed parameters and to easily predict downstream temporal concentration profiles due to the manhole structure.

To study the effect of changes in pipe direction across a surcharged manhole on the dispersion and head loss, laboratory apparatus was set as shown in Figure 3.1. It is a re-circulating system, which consists of 5 main units: pump sump, header tank, manhole, surcharge tank and storage tank. Firstly, the water in the pump sump is pumped to the constant header tank at a rate greater than required through the apparatus and the excess is returned directly to the sump. After that, it flows by gravity through the manhole, on which a water level follower was placed to measure surcharge; then flows over a variable weir in the surcharge tank and down into the storage tank. Between the header tank and the surcharge tank, 2 fluorimeters and 6 manometer ports were installed to collect raw data. At the far end of the storage tank, the water flows over a 30° V-notch weir into the pump sump. At this stage, the flow re-circulation is complete and it will be sent to the header tank again in order to start a new circulation.

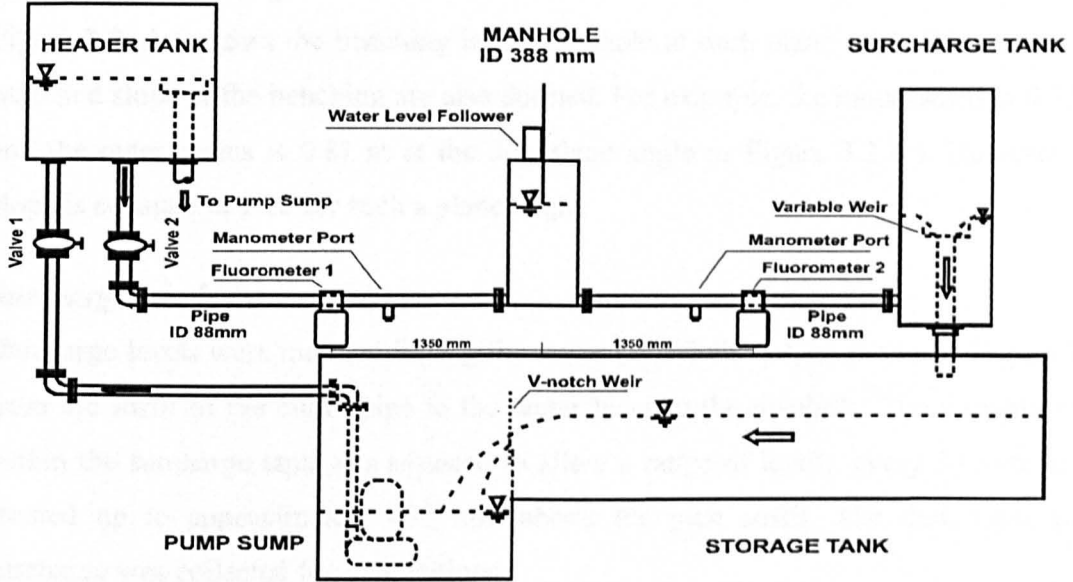


Figure 3.1 Laboratory apparatus

### 3.1 Manhole configurations

A circular 388 mm internal diameter manhole was constructed from transparent material to allow inspection of the internal flow processes occurring. For the manhole, 4 main factors were investigated; that was plane angles, benching/unbenching, surcharge levels and discharge.

#### *Plane Angles ( $\theta$ )*

For this study, the plane angles that is the change in direction in plan between the inlet and outlet pipes, were set at  $0^\circ$ ,  $30^\circ$ ,  $60^\circ$  and  $90^\circ$  as shown in Figure 3.2. This was considered to cover the range of angles, which are often met in sewer system. The angle change directly affects the head loss and possibly the retention time and dispersion of soluble pollutants in such a sewer network. In addition, to remove the effect of elevation changes both 88 mm inlet and outlet pipes were laid horizontally.

### ***Benching/unbenching***

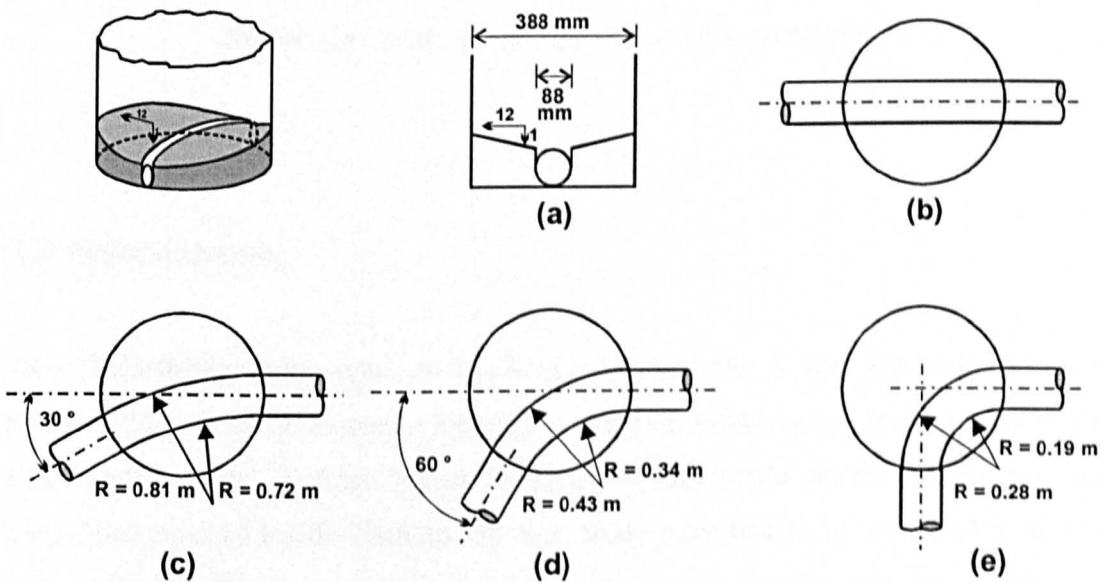
Figure 3.2 also shows the benching in the manhole at each plane angle. Moreover, the radii and slope of the benching are also defined. For example, the inner radius is 0.72 m and the outer radius is 0.81 m at the 30° plane angle in Figure 3.2 (c). However, its slope is constant at 1:12 for such a plane angle.

### ***Surcharge Levels (S)***

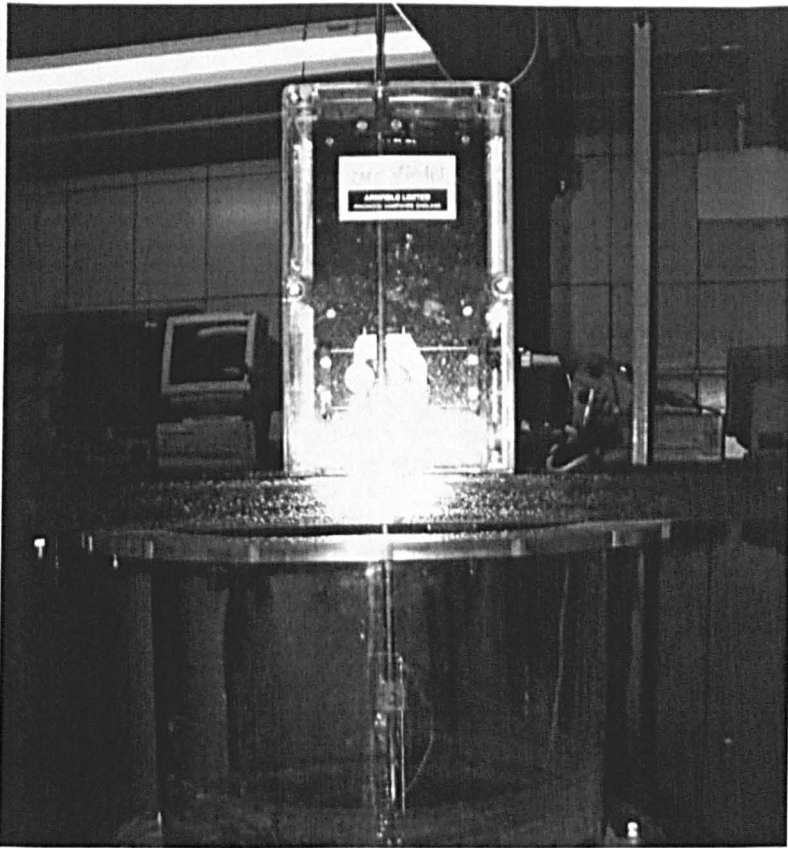
Surcharge levels were measured using the water level follower, as shown in Figure 3.3, from the soffit of the outlet pipe to the water level in the manhole. The variable weir within the surcharge tank was adjusted to allow a range of levels, every 30 mm, to be studied up to approximately 450 mm above the pipe soffit. The data from each surcharge was collected for 3 repetitions.

### ***Discharge (Q)***

The flow rates were studied at 1, 2, 4, 6 and 8 l/s, or at the mean flow velocities of 0.16, 0.33, 0.66, 0.99 and 1.32 m/s, respectively.



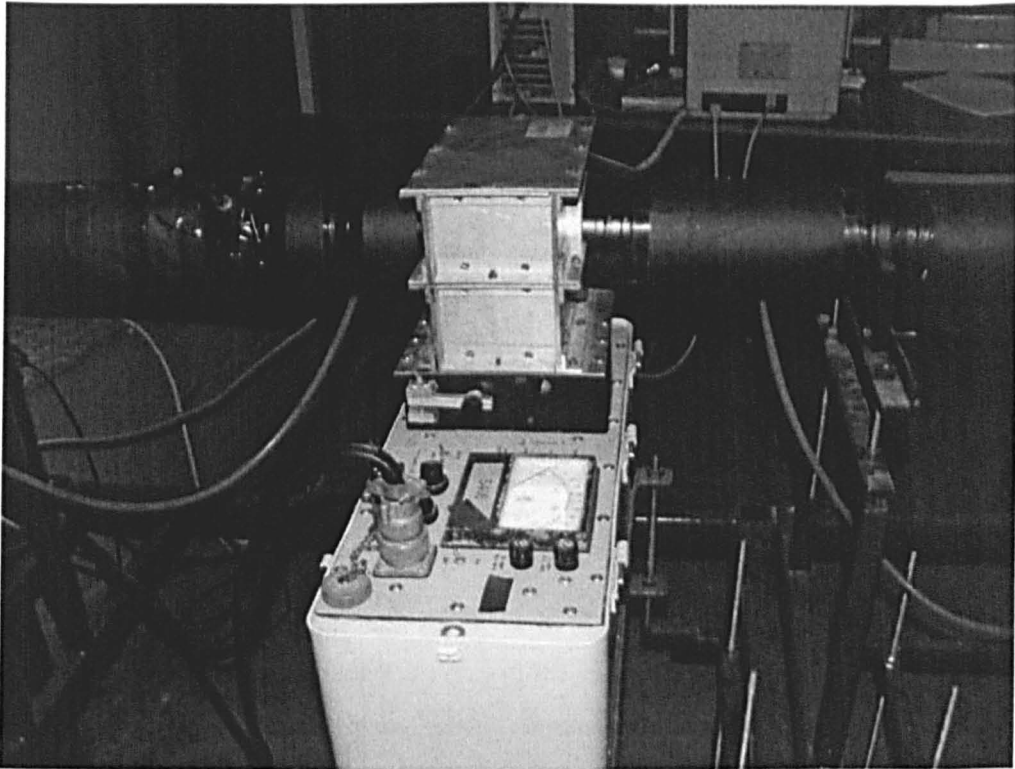
**Figure 3.2** Benched manhole configurations



**Figure 3.3** Water level follower to measure surcharge

### 3.2 Fluorometers

Two fluorometers were used in this study. Fluorometer 1 and Fluorometer 2 were placed 1350 mm from the centre line of the manhole as shown in Figure 3.1. Both were fluorometers model 10 from Turner Designs. As they could not be directly employed with clear pipes of inside diameter 88 mm, some parts had to be modified to fit them with adapters. These were built by the water group, the Department of Civil and Structural Engineering, the University of Sheffield (O'Brien, 2000). The other ends of both adapters were clamped around the inlet and the outlet pipes of the manhole as shown in Figure 3.4.



**Figure 3.4** Fluorometer and adapter

### ***Background***

A fluorometer is an instrument used to measure fluorescence, which is the molecular absorption of light energy at one wavelength and re-emission at a higher one. The fluorometer generates the light required to excite the substance; then it selectively transmits the wavelength of light after which it measures the intensity of the emitted light. Within a certain range, it is proportional to the concentration of the substance. This measurement, however, may be influenced by many variables such as temperature, turbidity, air bubbles, pH, photochemical decay and chlorine.

Fluorescence intensity varies inversely with temperature (Smart and Laidlaw, 1977) and from the experimental data, it was fitted to Equation 3.1,

$$F = F_0 \exp (nt) \quad (3.1)$$

where  $t$  = temperature, ° C;  $F$  = fluorescence at  $t^\circ$  C;  $F_0$  = fluorescence at  $0^\circ$  C; and  $n$  = constant. Smart and Laidlaw (1977) quote a value equal to  $-0.027$  for Rhodamine WT, the fluorescent tracer dye to be used in this study.

### ***Calibration***

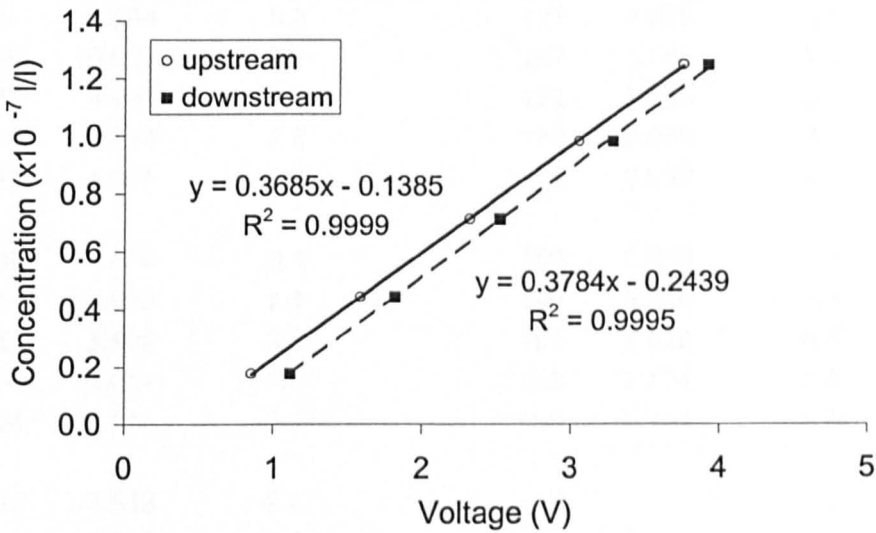
A small closed system was assembled to calibrate both fluorometers in situ. The fitting in front of Fluorometer 1 as shown in Figure 3.1 was taken out. An 88x25 mm reducer was placed instead of the fitting. The surcharge tank was used as a temporary pump sump. A small pump was used to complete the closed system by pumping water from the 88x25 mm reducer to the new pump sump, i.e. the surcharge tank, in which the water was not allowed to overflow to the storage tank.

A fluorometer measures dye concentration by detecting light, so extraneous light must be prevented from interfering with the measurement. Therefore, both the pipes and the manhole were covered by light-proof sheet. In addition, the ends of the flexible pipes that were connected to the reducer and the temporary pump sump also needed to be enclosed.

To effectively apply the scale of the measurement, the upper limit of the scale should be found. After the small closed system and light-proof sheet were fitted, the system was filled with a known amount of water. Rhodamine WT was used as a tracer dye. Even though O'Brien (2000) described that the maximum concentration with a linear response was  $8 \times 10^{-7}$  l/l, the known amount of water was employed to calculate the volume of Rhodamine WT for only  $1.4 \times 10^{-7}$  l/l. A known amount of Rhodamine WT was put into the system; then, the fluorometer measurement was adjusted to the upper range. At this time, the measurement of fluorometer was effectively achieved. Afterwards, the water in the system needed to be withdrawn and the system needed to be cleaned before next calibrating.

The concentration of Rhodamine WT and the mean of each output voltage would be plotted and a calibration equation was determined. An example of fluorometer calibration is shown in Figure 3.5. It presents the output voltage from upstream and downstream fluorometers on the x axis and dye concentration on the y axis. Moreover,

$R^2$ , slope and y-intercept are also shown. Their figures, for example, are 0.9999, 0.3685 and  $-0.1385$ , respectively for the upstream fluorometer.



**Figure 3.5** Calibration for upstream and downstream fluorometers

### 3.3 30° V-notch weir

A 30° V-notch weir was fixed between the storage tank and the pump sump as shown in Figure 3.1. The governing equation for any V-notch weir is

$$Q = C_d \left( \frac{5}{8} \right) \tan \left( \frac{\theta}{2} \right) H^{5/2} \sqrt{2g} \tag{3.2}$$

where  $Q$  = flow rates,  $m^3/s$ ;  $C_d$  = coefficient of discharge, 0.597 (Dennis, 2000);  $\theta$  = V-notch angle, 30°;  $H$  = over flow level, m; and  $g$  = acceleration due to gravity,  $9.81m/s^2$ .

In this study, there were 5 flow rates investigated, namely 1, 2, 4, 6 and 8 l/s. To be practical while doing the experiment, flow rate was presented in terms of the height of the overflow levels in Table 3.1. The levels were measured by the level gauge, whose resolution was 0.1 mm. In reality, it was very difficult to precisely adjust flow rate by reading from the level gauge. Therefore, an allowable error should be considered. Table 3.1 also points that the error per mm of reading is approximately from 2.7 % to 1.2 % at flow rate 1 l/s and 8 l/s, respectively.

**Table 3.1** Error per mm for level gauge reading

H (mm)	Q (l/s)	% error per mm	H (mm)	Q (l/s)	% error per mm
91	0.944	5.3	121	1.925	4.0
92	0.970	2.7	122	1.965	2.0
93	0.997	0.0	123	2.005	0.0
94	1.024	2.7	124	2.046	2.0
95	1.051	5.5	125	2.088	4.1
160	3.870	3.1	189	5.869	2.6
161	3.930	1.5	190	5.946	1.3
162	3.992	0.0	191	6.025	0.0
163	4.054	1.6	192	6.104	1.3
164	4.116	3.1	193	6.184	2.6
212	7.820	2.3			
213	7.913	1.2			
214	8.006	0.0			
215	8.100	1.2			
216	8.194	2.4			

### 3.4 Water level follower

A water level follower was installed to measure surcharge levels above the soffit. It was an H45 model, made by Armfield limited. The water level or surcharge was converted into a digital signal, whose voltage could adjustable between  $-9.75$  to  $+9.75$  V or the signal changed approximately 30 mV per mm. The linear relationship between surcharge and voltage is shown in Figure 3.6 for the calibration.



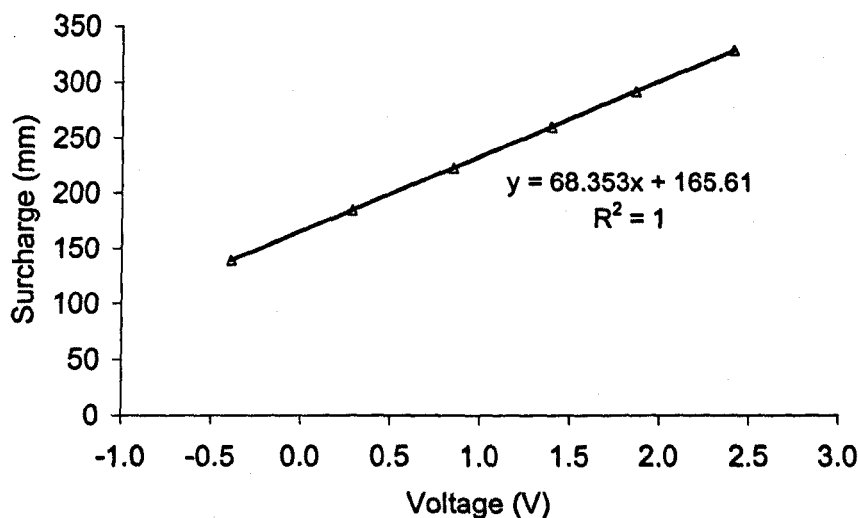


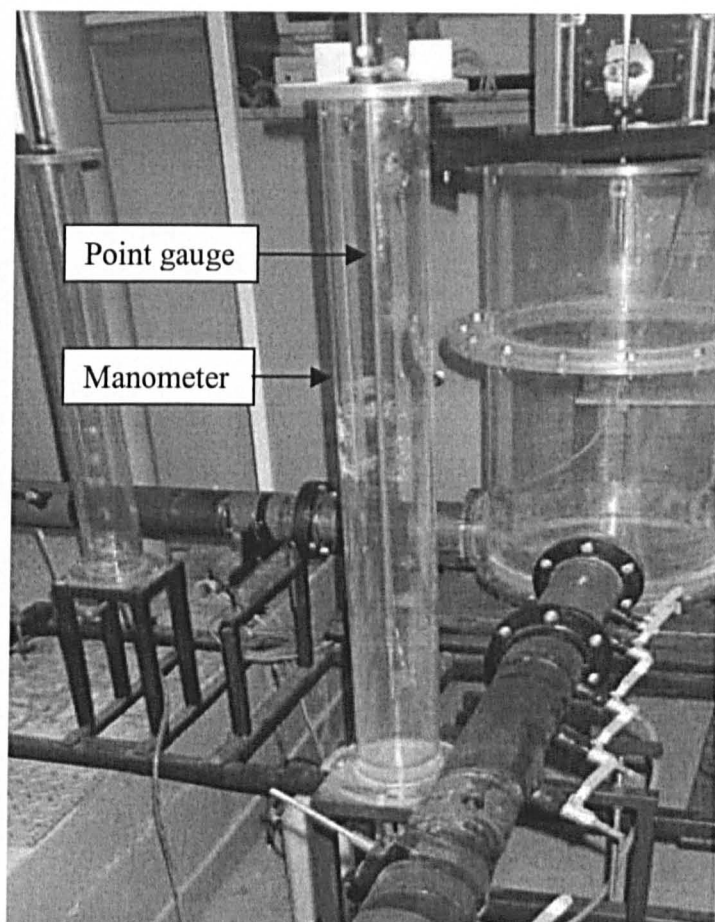
Figure 3.6 Linear calibration for water level follower

### 3.5 Manometers

An 88 mm diameter transparent pipe was used to make a manometer, in which a point gauge was placed to observe water levels as shown in Figure 3.7. At the bottom of the manometer, a flexible tube was connected between the manometer and the inlet or outlet pipe of the manhole. Each side of the inlet and outlet pipes was installed with 3 manometers. On the upstream pipe, the 3 manometers were located at 360, 1380, and 2280 mm from the centre of the manhole; meanwhile another 3 manometers were connected at 950, 1820, 2250 mm on the outlet pipe. The different distances were to avoid the effect of a vena contracta on the downstream pipe, in which the first manometer was placed at 950 mm. Such 3 positions of the manometers obviously showed the best  $R^2$ , compared to the linear fit from 5 positions as shown in Figure 3.8.

### 3.6 Data collection

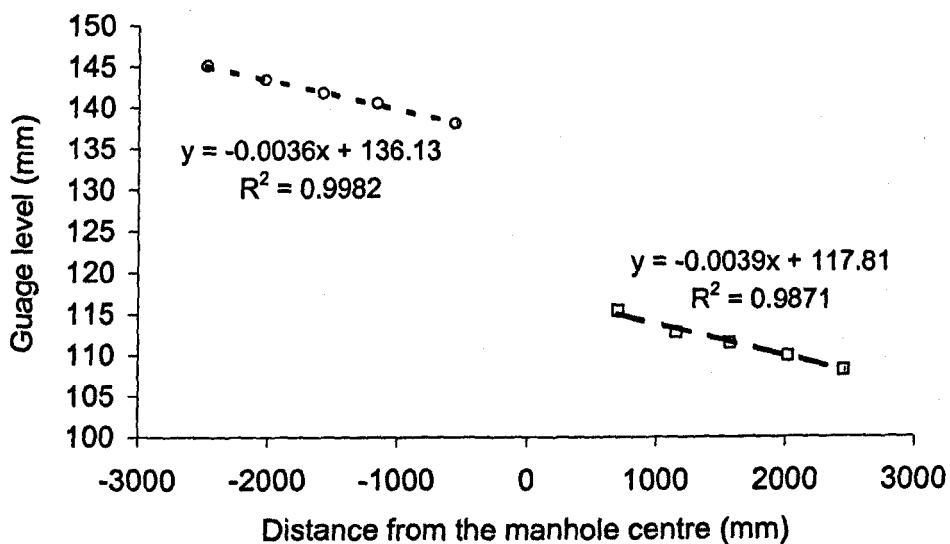
After the laboratory apparatus was set as shown in Figure 3.1, a total of 6 parameters, such as plane angles, benching/unbenching, flow rates, surcharge levels, dye concentration and pressure in terms of heads of water, were required as shown in Table 3.2. The first two parameters were obtained while the apparatus were initially installed, but the remaining parameters were collected while the water was re-circulating .



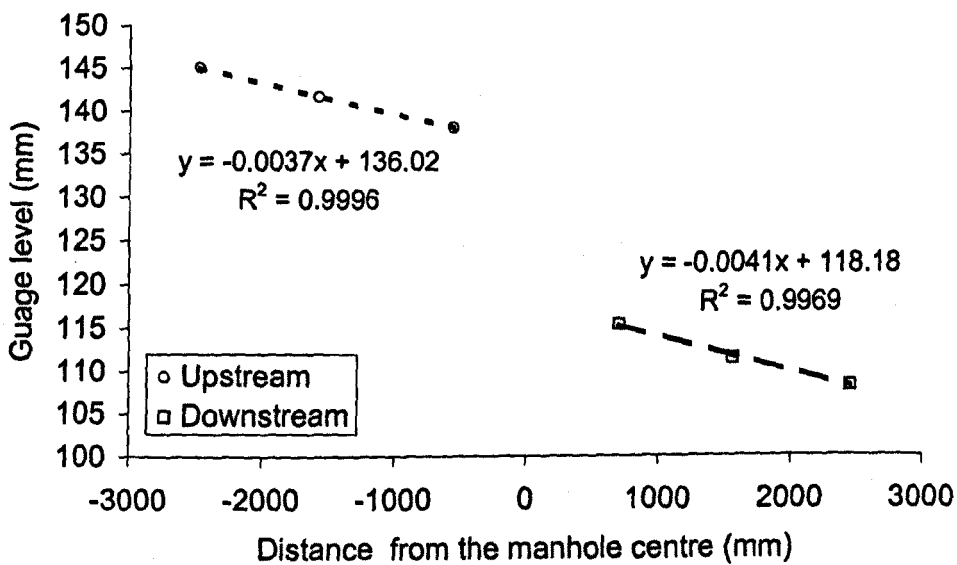
**Figure 3.7** Manometer and point gauge

**Table 3.2** Details of data collection

Collection	Details
Plane angles	0°, 30°, 60° and 90°
Floor types	Benching and unbanching
Flow rates	1, 2, 4, 6 and 8 l/s
Surcharge levels	During 0 - 450 mm, increasing every 30 mm
Temporal dye concentration	Upstream and downstream pipes for 3 repetitions at each surcharge level
Head of water	3 upstream and 3 downstream manometers



(a)



(b)

**Figure 3.8** Comparison on  $R_i^2$  of observed manometers for an inlet/outlet pipe: (a) 5 positions and (b) 3 positions

### ***Collecting procedures***

To attain a required flow rate and surcharge level, firstly Valve 1 was opened fully and the pump was switched on. Once the exceeded water in the header tank returned into the pump sump, Valve 2 was opened partly and the variable weir in the surcharge tank was adjusted to an expected level. It was a stage of trial and error this time. The system might take around an hour before the level of the flow over V-notch weir remained constant. Next, the overflow level was read from a point gauge and converted to a flow rate with Table 3.1; in the mean time, a surcharge level in the manhole was measured by the water level follower. At this time, if either the flow rate or the surcharge level did not reach the desired value, Valve 2 or the variable weir was adjusted again. To gain both the flow rate and the surcharge level, the procedure of opening the valve and performing the weir should be done several times until the required flow rate was obtained within an accepted range of error percentage as also shown in Table 3.1 as well as the surcharge level was acceptable. Then, the flow rate and the surcharge level were recorded.

Secondly, a small amount of dye concentration was injected and its temporal variation was measured by both fluorometers. Approximately  $15 \text{ cm}^3$  of approximately  $2.5 \times 10^{-4}$  1/l solution of Rhodamine WT was introduced at a port which was approximately 10 m upstream from Valve 2. The reason for the certain distance was to ensure that the dye will be mixed well in pipes. It was greater than 100 pipe diameter distance (Guymer and O'Brien, 2000).

Next, output voltages from Fluorometer 1 & 2 and the water level follower were recorded by a personal computer (PC). A computer board type ISA model CIO-DAS802/16, a product of Measurement Computing Corporation, had been installed into the PC. The board was operated with DAS-Wizard software, which was an add-in programme for Microsoft Excel, i.e. the measured data could be placed directly into the cells of an Excel worksheet. Its configuration had been set to log the data for 6 minutes at a rate of 33 Hertz. On the sheet, there had been 4 columns, each of which represented a series of time and voltages from Fluorometer 1, Fluorometer 2 and the water level follower, respectively. Besides, these data were also simply presented in a chart format to monitor the collection. After this, both the data on the worksheet and the chart could be saved as usual by Excel.

To reduce errors while testing, second and third repeated data collections were required. The parameters were analysed and presented in terms of the mean and the deviation in Chapter 4. For the experiment, the tracer dye would be injected every 10 minutes to prevent an influence of the previous dye on the present dye profile. While such data were recorded directly to the PC, the heads of the water in the manometers were also collected manually. In general, scales of the point gauges would be read during the third repetition to ensure that the water level in the manometers remained constant. This would be a complete data collection at each surcharge level with regard to dye concentration profile, surcharge in the manhole and pressure heads along the pipe.

Finally, the flow rate and temperature were recorded from reading the pointer gauge and a thermometer in the storage tank. This was to ensure that it was a required flow rate as well as the dye concentration profile could be adjusted due to the temperature effect on the fluorimeters' output. Then, the surcharge level was ready to set to another level, so that the procedure of the data collection could be restarted from the first step again.

### 3.7 Data analysis

#### 3.7.1 Head loss coefficient

After 6 data points were collected manually from the manometers upstream and downstream, the linear function with least square in Excel were used. Then, the line was extrapolated to the manhole centre before the head loss was determined from the difference of these 2 hydraulic grade lines as shown in Figure 2.4. Finally, the head loss coefficient (K) was calculated from

$$K = \frac{\Delta H}{\frac{V^2}{2g}} \quad (3.3)$$

where

$\Delta H$  = head loss due to the manhole

$V^2/2g$  = velocity head

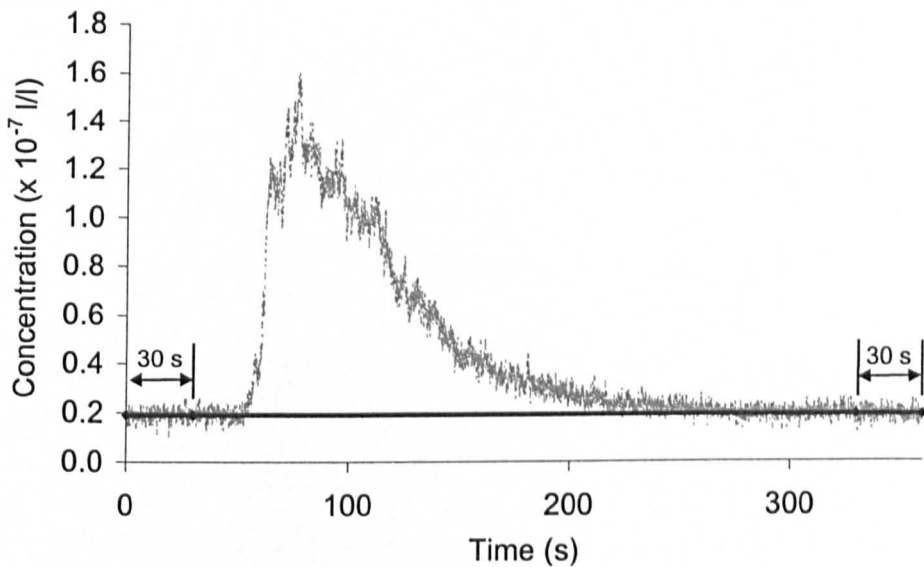
$g$  = acceleration due to gravity

### 3.7.2 ADE/ADZ analysis

To obtain calibrated parameters, such as travel time ( $\bar{t}$ ), dispersion coefficient ( $D_L$ ) and reach time delay ( $\tau$ ), for solute transport modelling, the raw data were processed in order of: removing background, balancing the downstream mass profile and finally optimising parameter technique as mentioned in the previous chapter.

#### *Removing background*

The voltage output data from Fluorometer 1 and 2 were converted to the dye concentration with the prepared calibration lines. Then, the temporal concentration of Rhodamine WT would be transformed again to be the concentration at 20° Celsius. Consequently, the upstream and downstream profiles represented measured concentration distributions, which were ready to remove the backgrounds. Next, a base line was generated from the two mean points of 30 s at the onset and end of each profile as shown in Figure 3.9. The collected upstream and downstream profiles was subtracted from the base line. Afterwards, the peak of each profile was quantified. The beginning and end of the profile were determined from the first 10 consecutive data from the peak position, whose values were smaller than 1 % of the peak value.



**Figure 3.9** Base line generated from two mean points of 30 s from the onset and end of concentration profile

***Balancing mass profile***

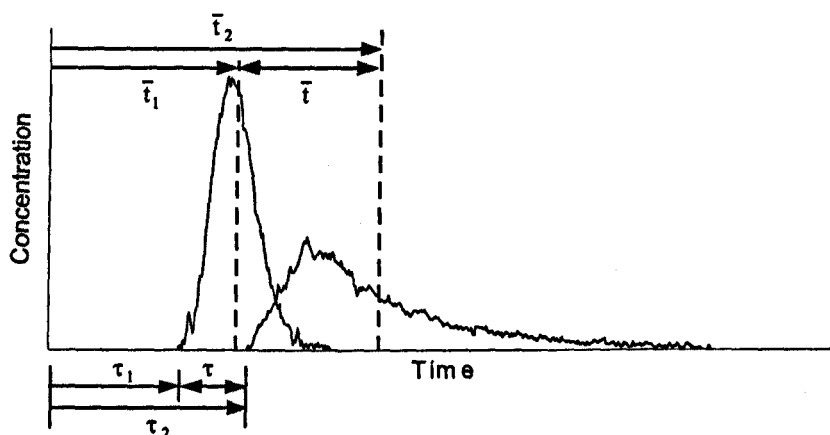
Tracer was injected at more than 10 m from the upstream fluorometer, i.e. greater than 100 times pipe diameter (Guymer and O'Brien, 2000). This is sufficient to achieve full cross-sectional mixing. However once the tracer has passed through the surcharged manhole, the tracer at the downstream fluorometer is unlikely to be cross-sectionally well mixed. Therefore, a difference of solute mass summation occurred between the measured upstream and downstream concentration profiles. Also, as either ADE or ADZ models is derived from mass conservation equation, the downstream profile should have mass or concentration balanced. Equation 3.4 describes that the mass balance factor (MF) equals the area of the upstream temporal concentration profile divided by the area of the downstream temporal concentration profile. Subsequently, the downstream data, whose background had been removed, were multiplied by the mass balance factor to calibrate or optimise the parameters.

$$MF = \frac{\int_{t=-\infty}^{\infty} c_u dt}{\int_{t=-\infty}^{\infty} c_d dt} \quad (3.4)$$

## Chapter 4

# Experimental results

This chapter consists of 2 main sections of the experimental work on the effect of changes in pipe direction, surcharge and benching. The first is concerned with head losses due to manholes, while the second is the result with regard to solute transport. The whole processed comprehensive data in this chapter are also presented in Appendix A, the companion CD-ROM.



**Figure 4.1** Concept for reach time delay and travel time

Figure 4.1 describes the concept of 2 main parameters, namely reach time delay ( $\tau$ ) and travel time ( $\bar{t}$ ) for solute movement. The reach time delay is the difference between when the first dye is observed at two sites and can be written as Equation 4.1. Meanwhile, travel time is the period of time between the centroids of the solute distribution profiles. The first moment of area technique is employed to calculate the centroids for site 1 (upstream) and site 2 (downstream) as shown in Equation 4.2, where  $n$  is equal to 1 and 2. Therefore, the travel time between the profiles is described by Equation 4.3.



$$\tau = \tau_2 - \tau_1 \quad (4.1)$$

$$\bar{t}_n = \frac{\int_{t=-\infty}^{\infty} t c_n(t) dt}{\int_{t=-\infty}^{\infty} c_n(t) dt} \quad (4.2)$$

$$\bar{t} = \bar{t}_2 - \bar{t}_1 \quad (4.3)$$

These 2 basic variables are used to model the solute transport in theory by the moment technique for both ADE and ADZ modelling. But in practice, most of the variables obtained from experimental data cannot predict the solute distribution that accurately fits the observed data. Other techniques, for example, optimisation or trial and error, might provide solutions to obtain better predicted profiles.

#### 4.1 Models to analyse data

To compare the ability of model prediction, ADE, ADE optimised, ADZ and ADZ optimised has been employed. As an example, predicted downstream concentration profiles and  $R_t^2$ , as defined in Chapter 3, from the data of 2 l/s flow rate and 148 mm surcharge from the 30°-unbenched manhole are shown in Figure 4.2. It is clear that the predicted profile from ADZ optimised, whose  $R_t^2$  is 0.99, is closer to the observed profile than the others.

Besides the comparison of the models at only one surcharge level,  $R_t^2$  from ADE optimised and ADZ optimised for the 30°-unbenched manhole from the whole flow rates and surcharge were also compared. Figure 4.3 shows that the  $R_t^2$  obtained from ADZ optimised were better than ADE optimised predicted. This can be described by the limitations of the model. ADE was based on several conditions, one of which is that the flow cross-section is not varying (Guymer and O'Brien, 2000), while the flow pattern in the experiment is not uniform due to the volume of a manhole. Therefore, the experimental data from here will be analysed and predicted by only ADZ optimised.

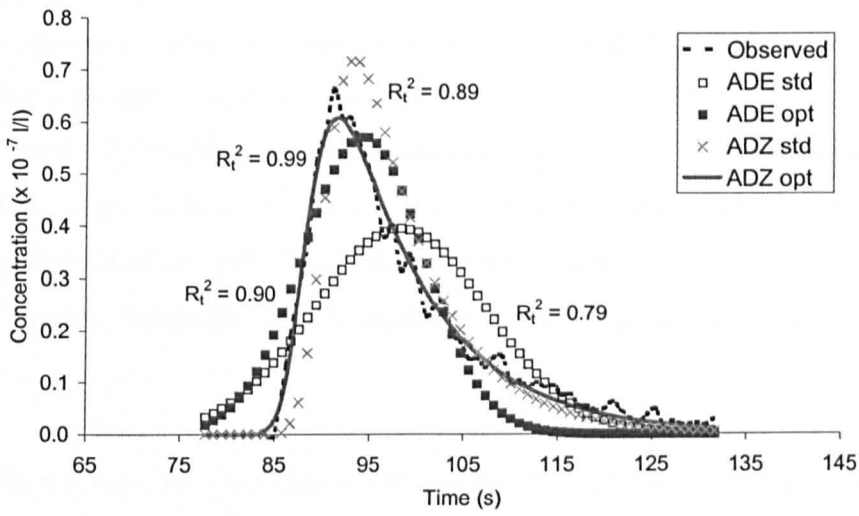


Figure 4.2 Predicted downstream profiles

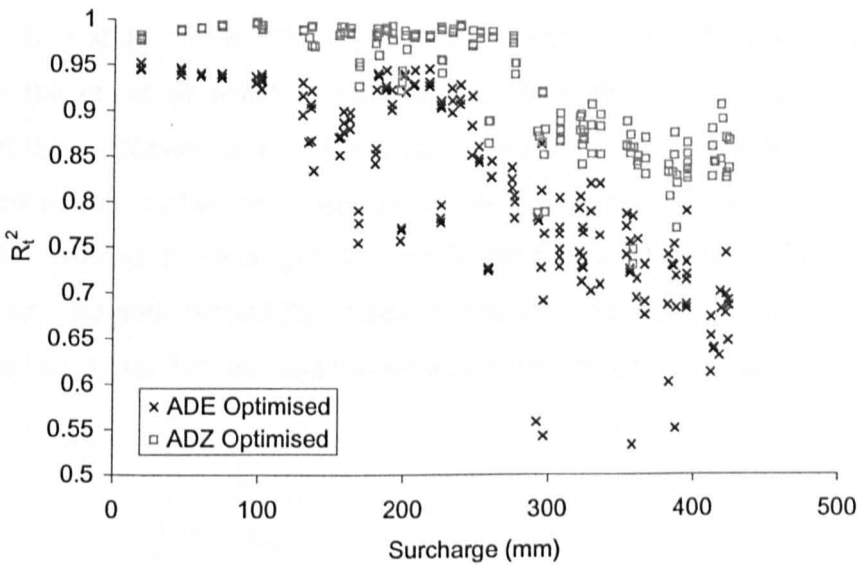
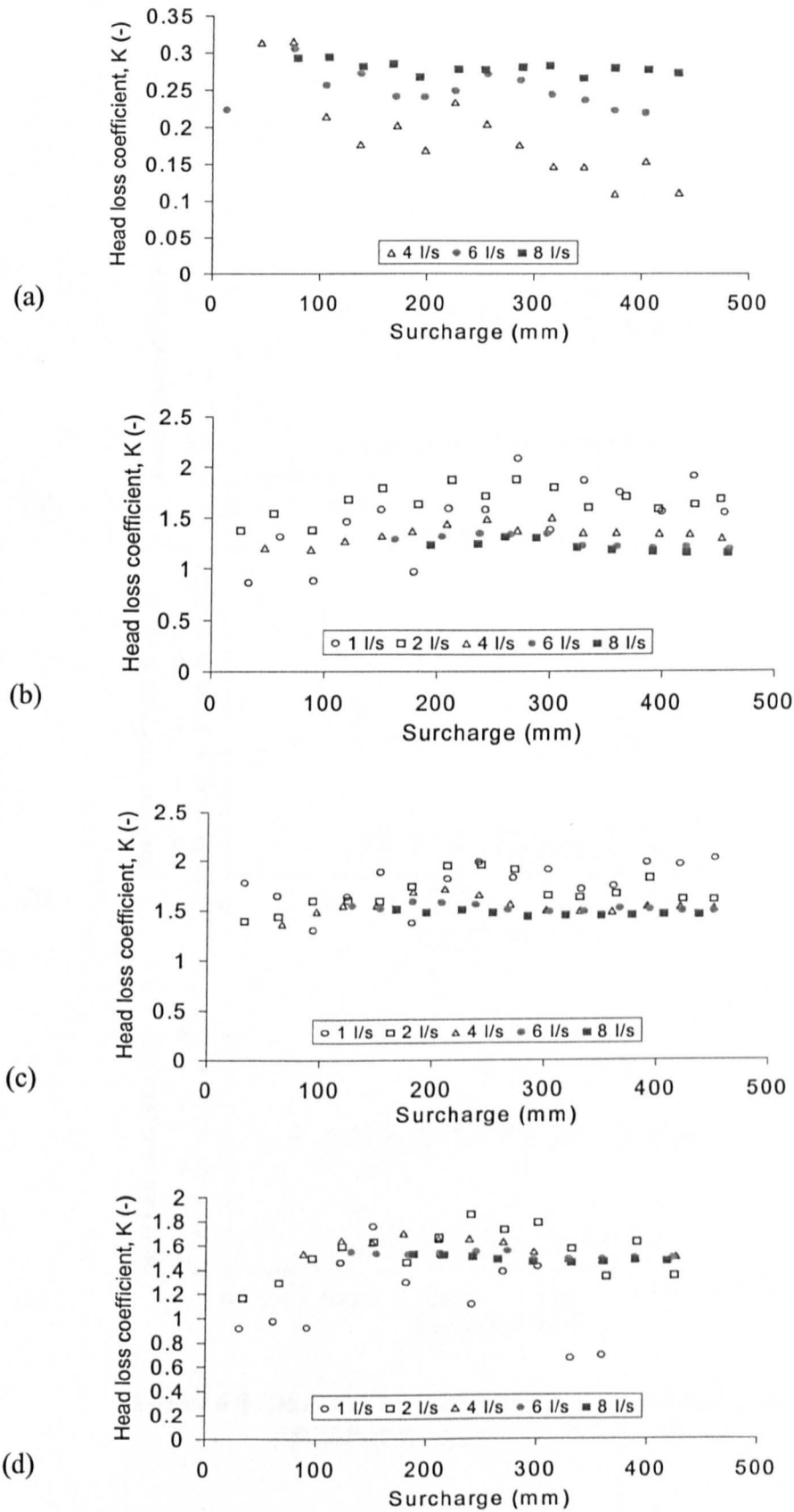


Figure 4.3  $R_t^2$  from ADE and ADZ optimised for the 30°-unbenched manhole

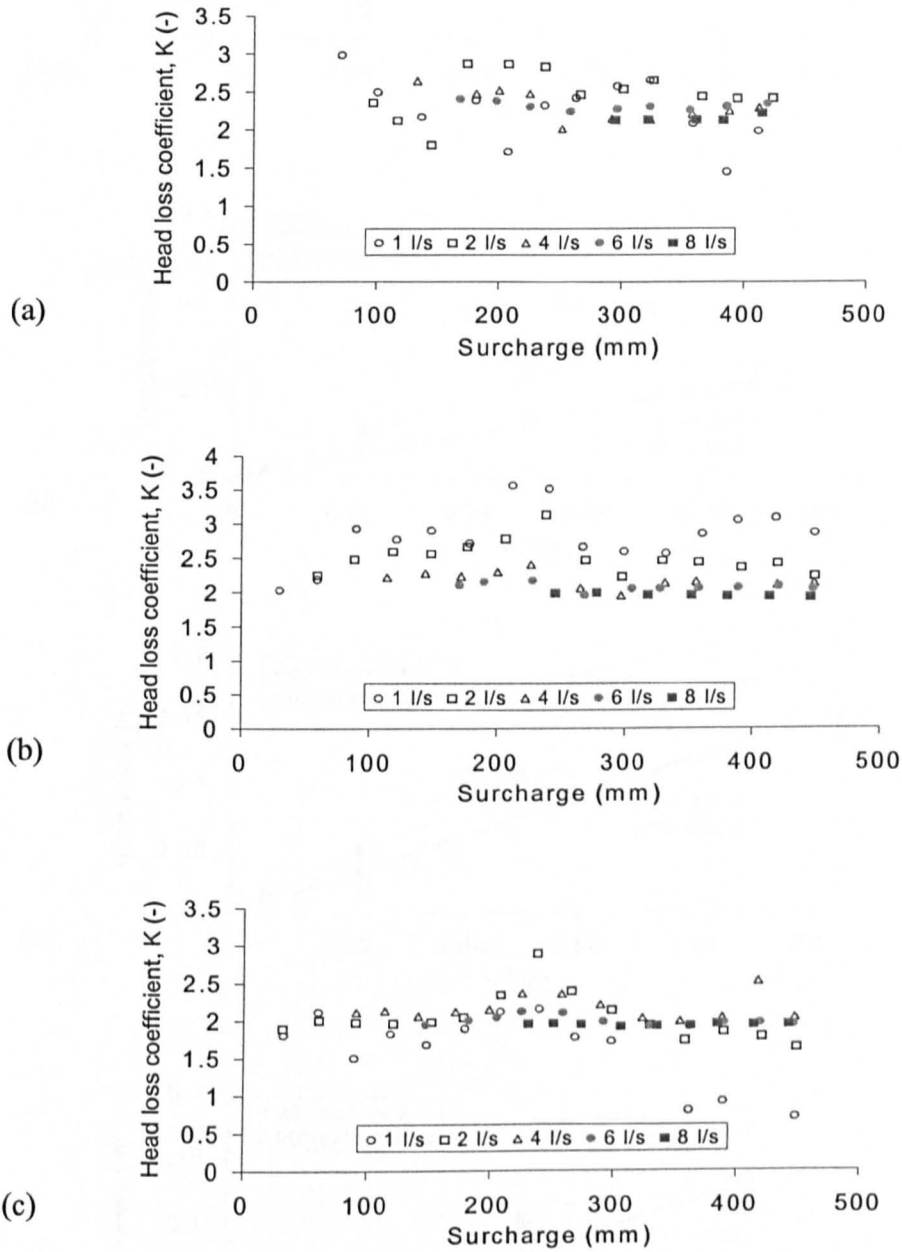
## 4.2 Head losses

The calculated head loss coefficient ( $K$ ) against surcharge is shown in Figure 4.4 and 4.5 for benched and unbenched manholes. It seemed that there was not a relationship between the head loss coefficient and surcharge as well as between the coefficient and flow rate. All of the coefficients were almost constant along the surcharge axis. Except the low flow rates such as 1 and 2 l/s of the 0°-benched manhole, the head loss coefficient fluctuated since the head losses were too small to be observed in the unit of mm; for example, the different value among 3 observing points was only 1 mm on the inlet pipe.

To quantify the head loss coefficient ( $K$ ), averaged head losses along surcharge were plotted against the velocity head ( $V^2/2g$ ) as shown in Figure 4.6. Both  $R^2$  and slopes, representatives of the head loss coefficient, are also presented in the figure. It seemed that the coefficient was related to the plane angle and benching/unbenching. For example, the head loss coefficient of the 0°-benched manhole is 10 times smaller than that of the 30°-unbenched manhole. For only benching effects, the head loss coefficient would drop when the manhole was benched. For instance, it declined from 2.22 to 1.24, 2.02 to 1.50 and 1.97 to 1.50 at the plane angle of 30°, 60° and 90°, respectively. Besides the effect of benching/unbenching, there also seemed to be a relationship between the coefficient and the plane angle. For the benched manholes, the coefficient increased when the plane angle became larger. Conversely, for the unbenched manhole, it reduced, instead. For example, the coefficient increased from 0.27 to 1.24 and to 1.5 for 0°, 30° and both 60° and 90°-benched manholes whereas it decreased from 2.22 to 2.02 and to 1.97 for 30°, 60° and 90°-unbenched manholes, respectively.



**Figure 4.4** Head loss coefficient (K) against surcharge from benched manholes: (a)  $0^\circ$ , (b)  $30^\circ$ , (c)  $60^\circ$  and (d)  $90^\circ$



**Figure 4.5** Head loss coefficient (K) against surchage from unbenched manholes: (a) 30°, (b) 60° and (c) 90°

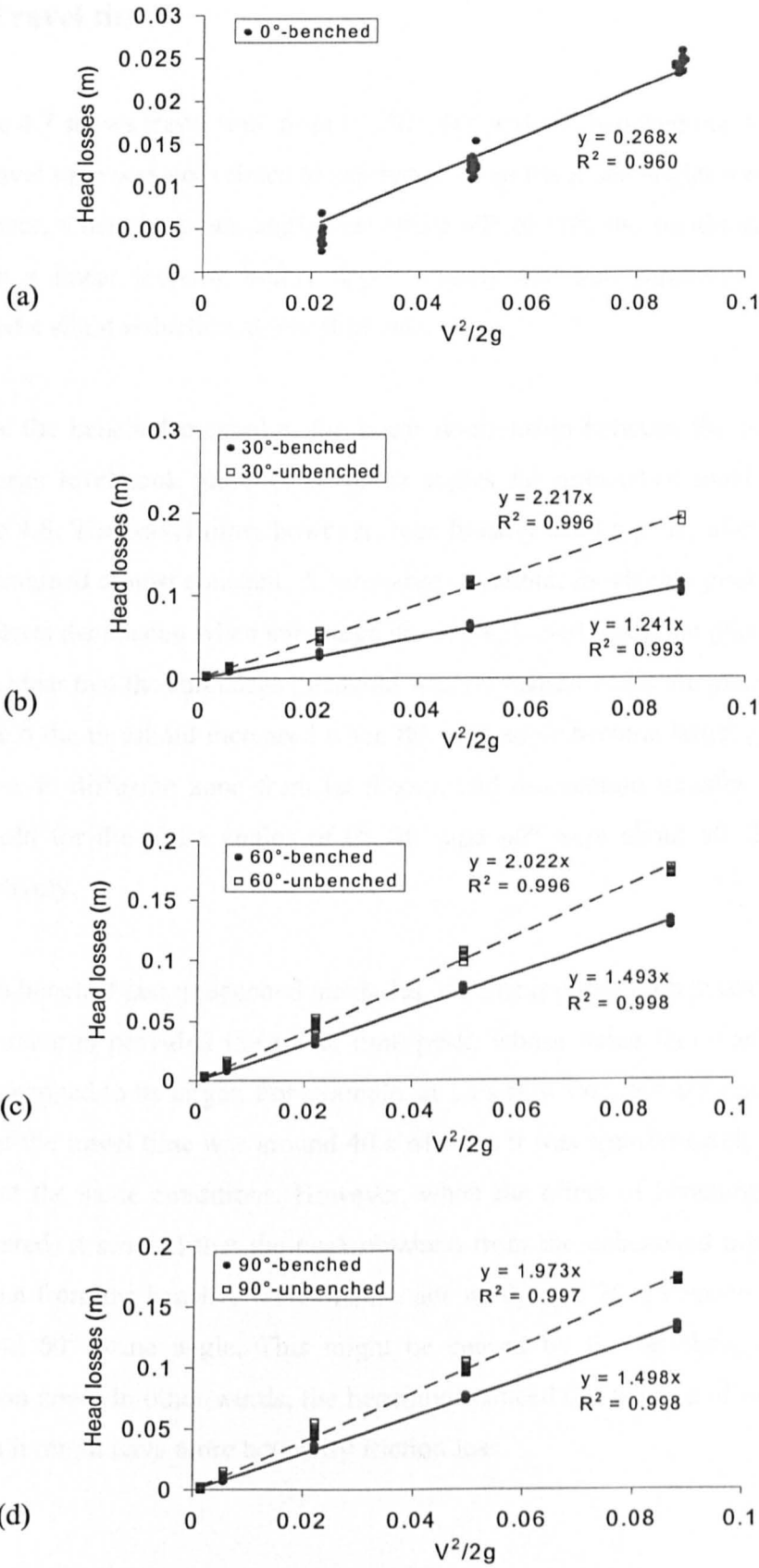


Figure 4.6 Head losses and head loss coefficient (K): (a)  $0^\circ$ , (b)  $30^\circ$ , (c)  $60^\circ$  and (d)  $90^\circ$

### 4.3 Travel time

Figure 4.7 shows travel time from  $0^\circ$ ,  $30^\circ$ ,  $60^\circ$  and  $90^\circ$  benched manholes. It shows that the travel time was not related to surcharge when the plane angles were lower than  $60^\circ$ . However, when the plane angle was either  $60^\circ$  or  $90^\circ$ , the relationship changed to be almost a linear increase before approximately 400 mm surcharge and afterwards it showed a slight reduction at low flow rate.

Unlike the benched manholes, the linear relationship between the travel time and the surcharge level took place at all plane angles for unbenched manholes as shown in Figure 4.8. The travel time, however, rose linearly until a peak; afterwards, it dropped and remained almost constant. A surcharge threshold, in which a peak occurs and travel time starts decreasing when surcharge increases, varied when the plane angles changed. It was clear that the surcharge threshold was very small while the plane angle changed a little and the threshold increased when the plan angle became larger probably due to an increase in diffusion zone from jet theory, and momentum transfer. For instance, the threshold for the plane angles of  $0^\circ$ ,  $30^\circ$  and  $60^\circ$  were about 50, 275 and 325 mm, respectively.

In both benched and unbenched manholes, the linear correlation between the travel time and surcharge provided the travel time peak, whose value increased when the plane angle changed to be larger. For example, at 1 l/s flow rate,  $60^\circ$ -unbenched manhole, the peak of the travel time was around 40 s whereas it was approximately 30 s at  $30^\circ$  plane angle at the same conditions. However, when the effect of benching/unbenching was considered, it seemed that the peak obtained from the unbenched manhole was higher than that from the benched manhole, i.e. about 40 s and 25 s, respectively on 1 l/s flow rate and  $60^\circ$  plane angle. This might be caused by the benching confining the jet diffusion zone. In other words, the benching reduced the volume of the diffusion, even though it might have more boundary friction loss.

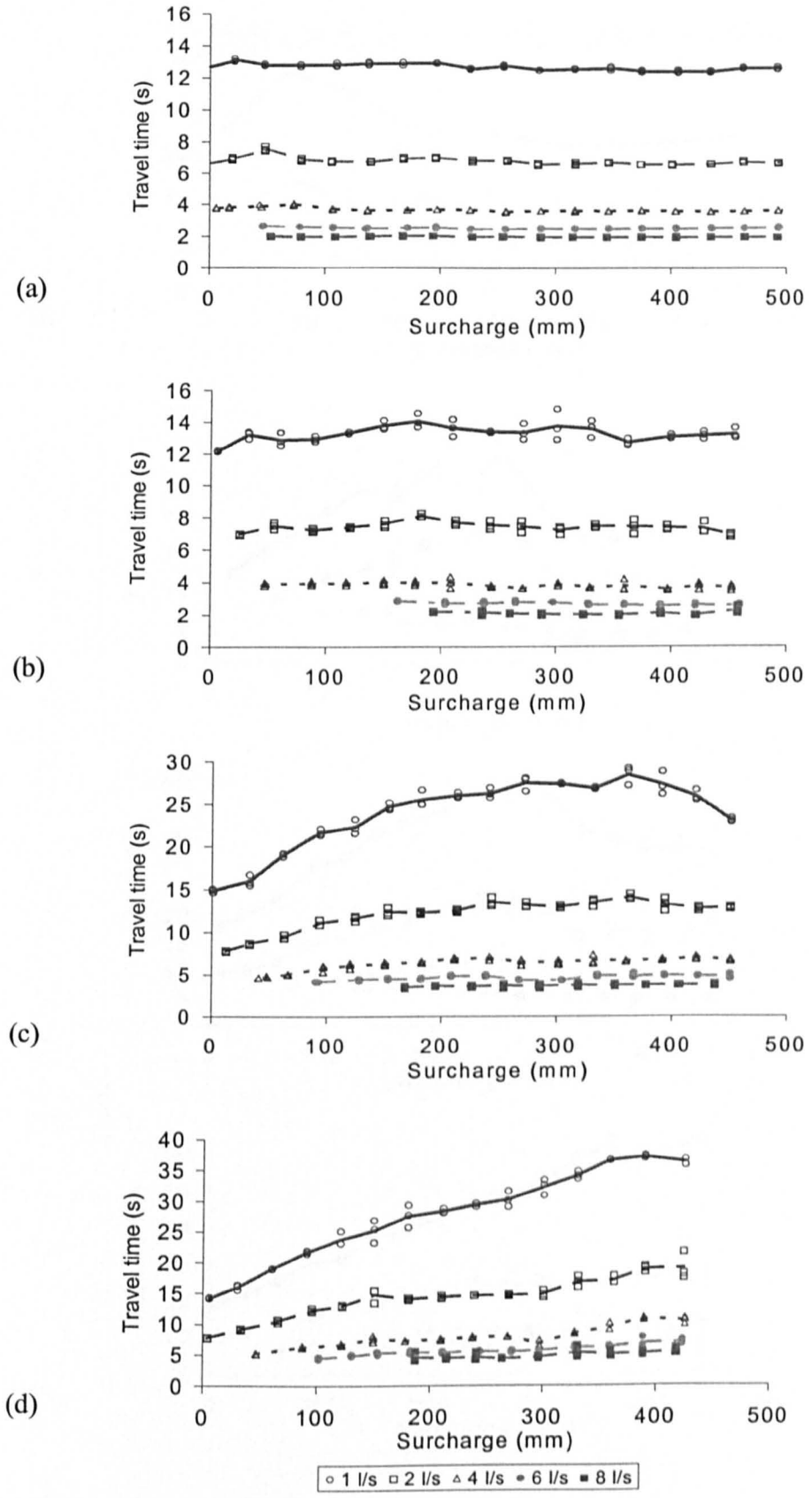
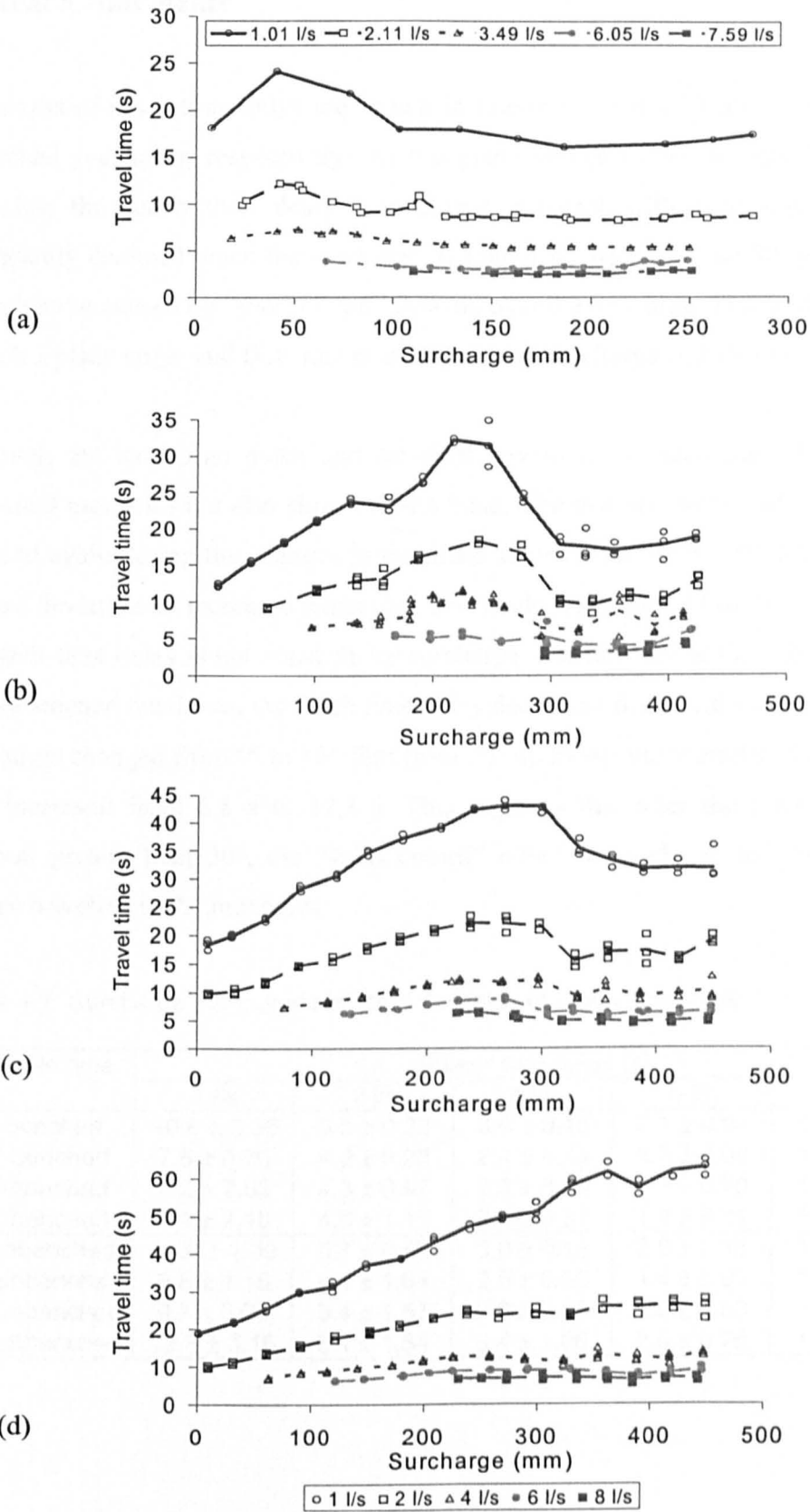


Figure 4.7 Travel time from benched manholes: (a) 0°, (b) 30°, (c) 60° and (d) 90°





**Figure 4.8** Travel time from unbenched manholes: (a) 0° (after Dennis, 2000), (b) 30°, (c) 60° and (d) 90°

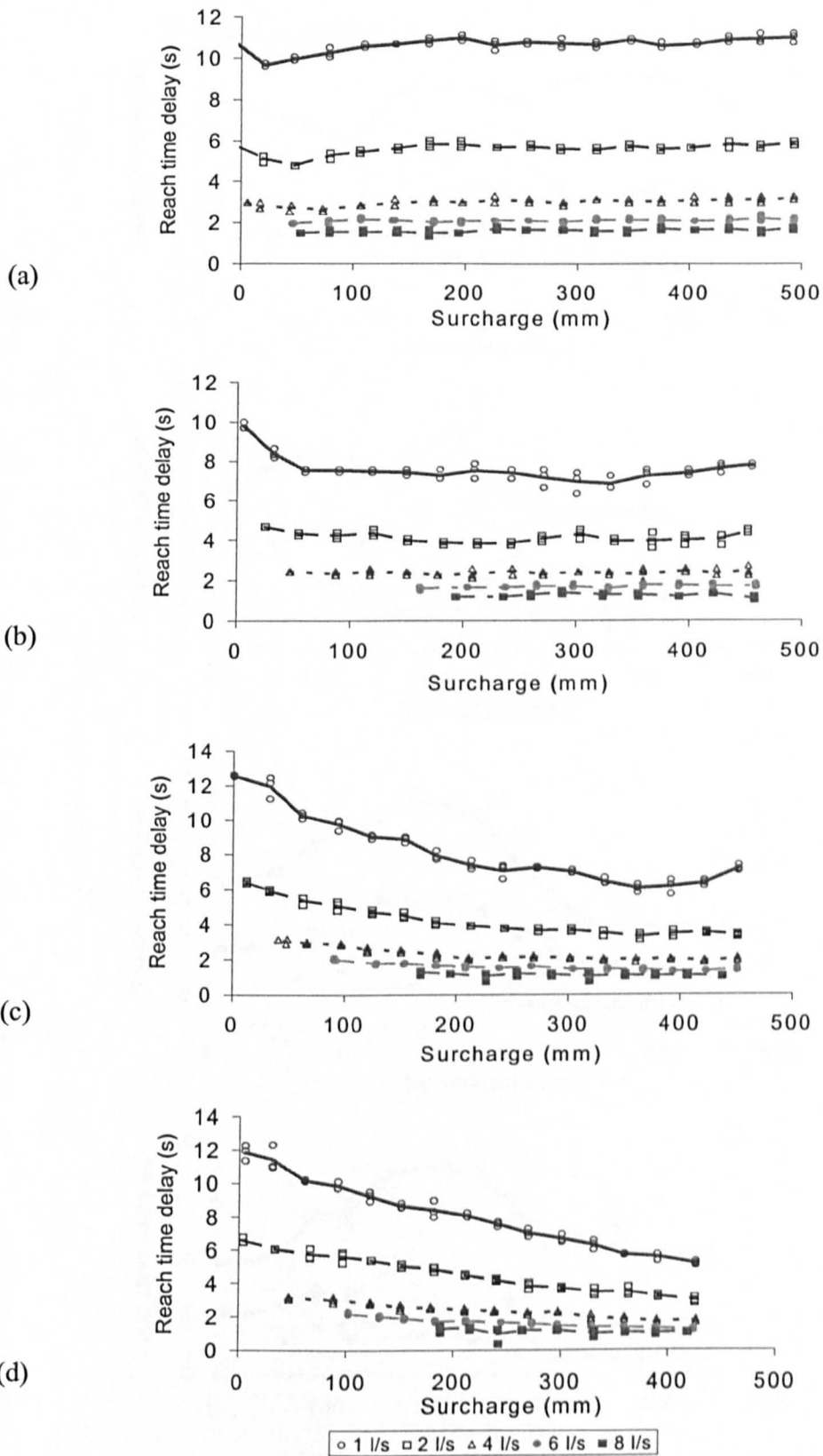
#### 4.4 Reach time delay

The results of reach time delay are shown in Figure 4.9 and 4.10 for the benched and unbenched manholes, respectively. At the plane angles of the 0° and 30°-benched manholes, the reach time delay was almost constant with surcharge whereas it significantly declined when the surcharge increased for both 60° and 90° plane angles. This might be caused by “short circuit” flowing over the benching. The reach time delay for such a plane angle and flow rate is averaged over surcharge and shown in Table 4.1.

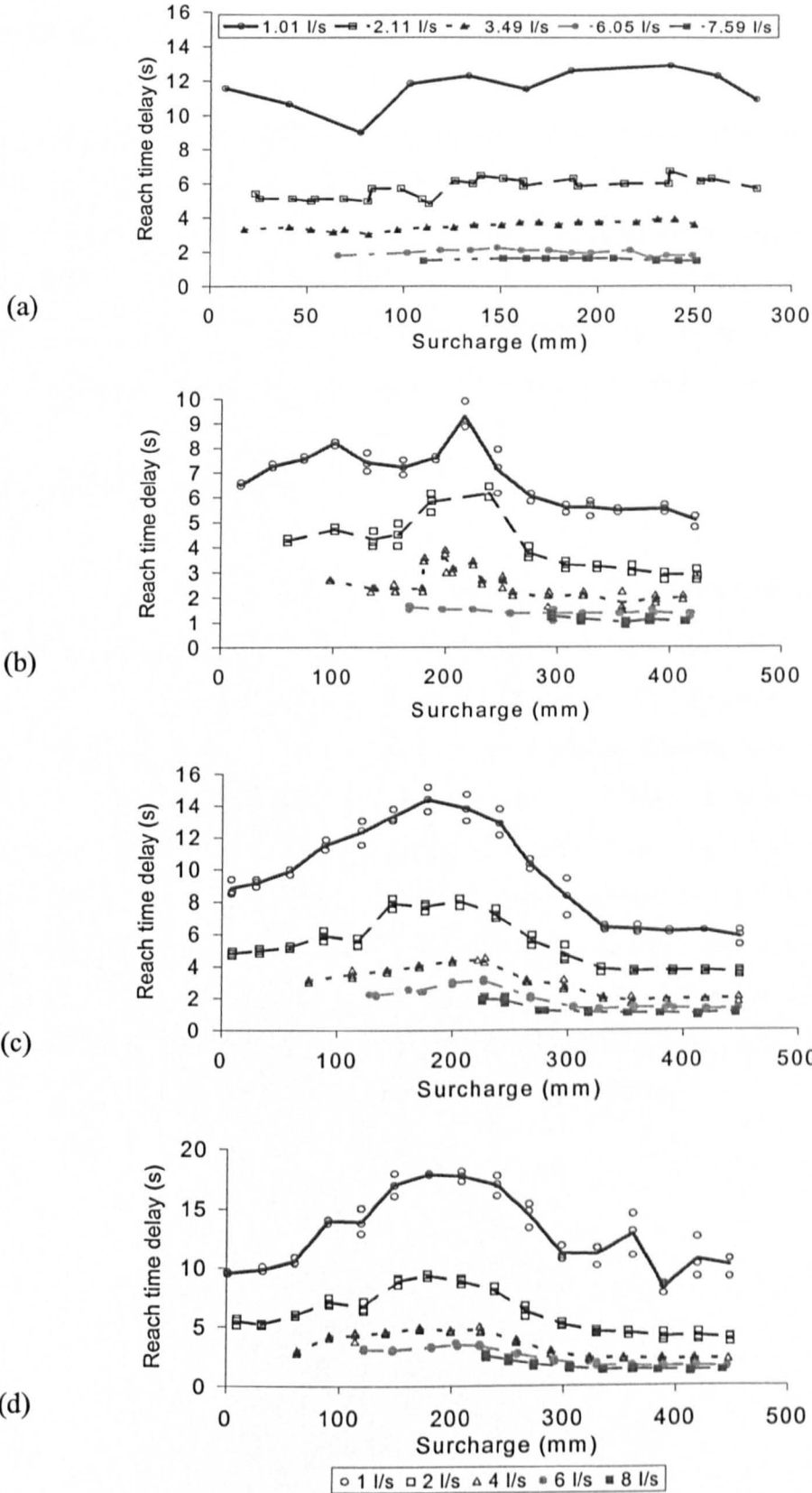
Moreover, the surcharge mean and standard deviation of reach time delay for the unbenched manholes are also shown in the table. The average decreased first and then increased again during the changes in the plane angles from 30° to 90°. Meanwhile, its standard deviation all increased when the plane angle was modified from 0°. This shows that reach time delay is not constant for surcharge. For instance at the velocity of 1 l/s from unbenched manholes, the reach time delay decreased from 11.6 s to 6.8 s when the plane angle changed from 0° to 30°. But from 30° up to 90° plane angles, the reach time delay increased from 6.8 s to 12.8 s. This suggests that after the plane angle was increased greater than 30°, the “short circuit” effect was reduced due to the longer distance travelled in the manholes.

**Table 4.1** Surcharge mean and standard deviation of reach time delay

Manhole type	Reach time delay (s)				
	1 l/s	2 l/s	4 l/s	6 l/s	8 l/s
0°-benched	10.6 ± 0.35	5.6 ± 0.28	3.0 ± 0.15	2.1 ± 0.07	1.6 ± 0.08
30°-benched	7.6 ± 0.70	4.2 ± 0.28	2.4 ± 0.14	1.7 ± 0.08	1.3 ± 0.10
60°-benched	8.2 ± 2.03	4.3 ± 0.97	2.3 ± 0.39	1.6 ± 0.20	1.1 ± 0.08
90°-benched	8.1 ± 2.10	4.6 ± 1.13	2.4 ± 0.31	1.6 ± 0.31	1.1 ± 0.13
0°-unbenched	11.6 ± 1.09	5.7 ± 0.55	3.0 ± 0.18	2.0 ± 0.16	1.6 ± 0.07
30°-unbenched	6.8 ± 1.15	4.1 ± 1.04	2.5 ± 0.55	1.4 ± 0.09	1.1 ± 0.09
60°-unbenched	9.7 ± 3.05	5.4 ± 1.57	3.0 ± 0.95	1.9 ± 0.69	1.3 ± 0.39
90°-unbenched	12.8 ± 3.16	6.1 ± 1.84	3.4 ± 1.06	2.5 ± 0.76	1.7 ± 0.46



**Figure 4.9** Reach time delay from benched manholes: (a)  $0^\circ$ , (b)  $30^\circ$ , (c)  $60^\circ$  and (d)  $90^\circ$



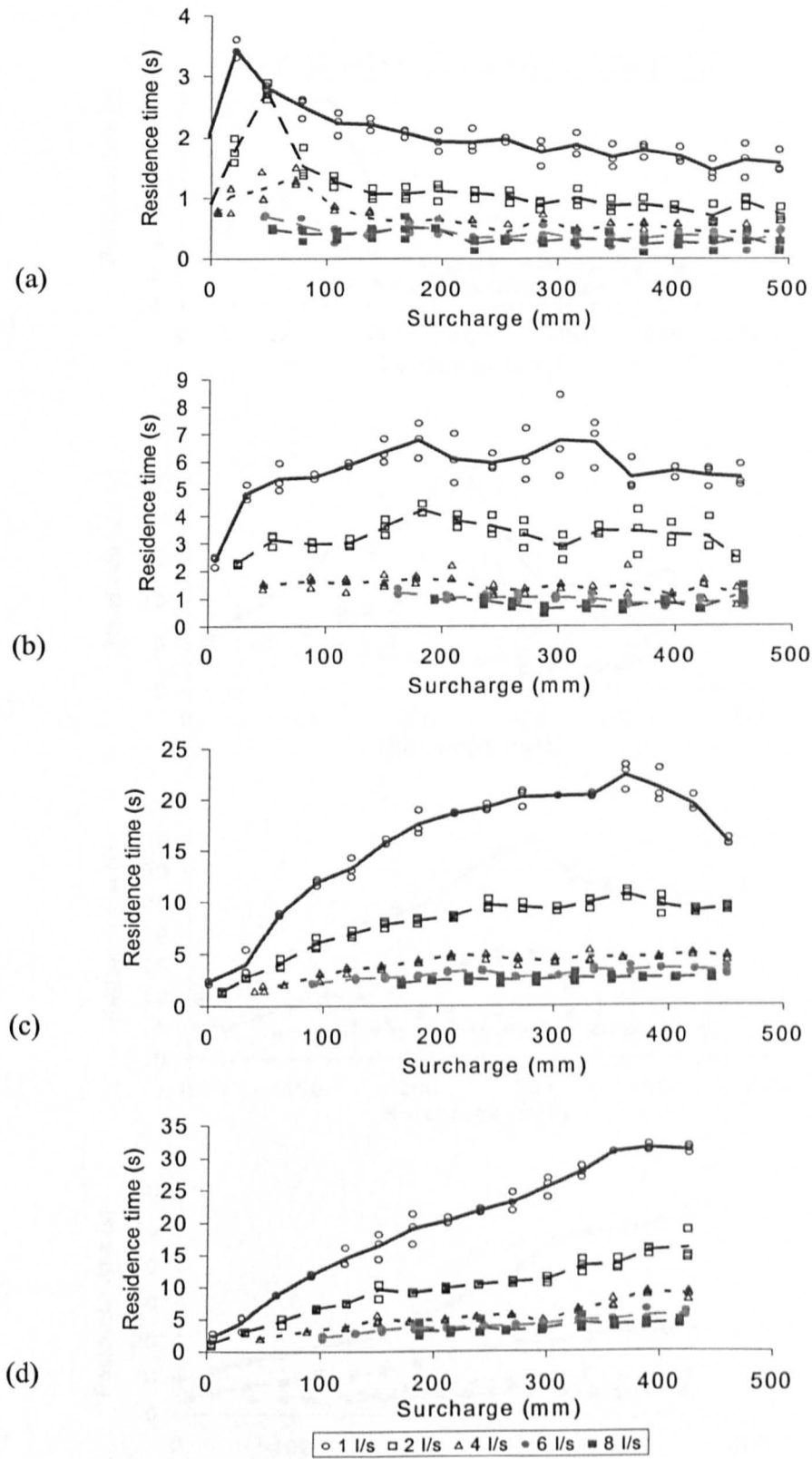
**Figure 4.10** Reach time delay from unbenched manholes: (a)  $0^\circ$  (after Dennis, 2000), (b)  $30^\circ$ , (c)  $60^\circ$  and (d)  $90^\circ$

## 4.5 Residence time

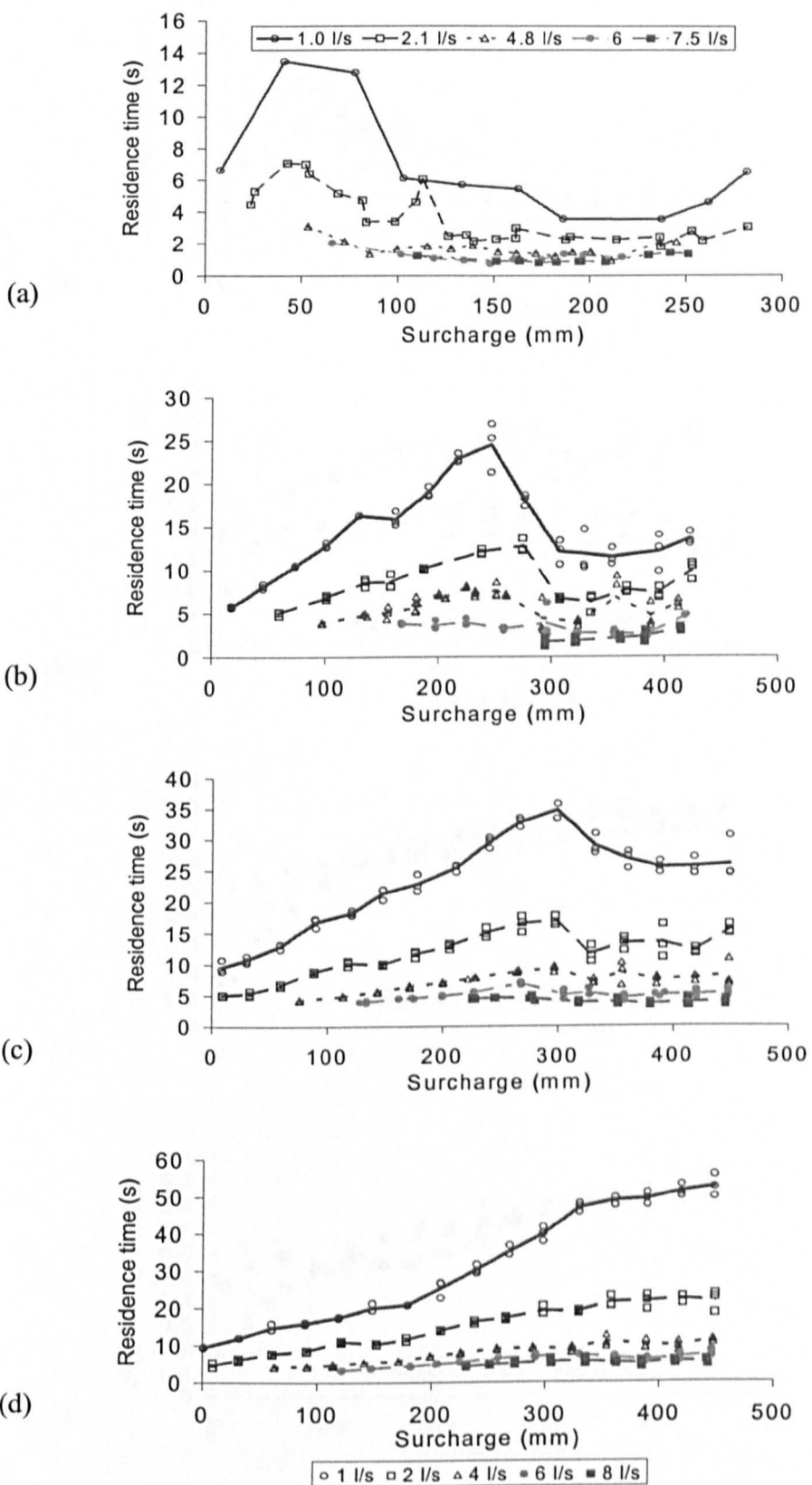
Residence time versus surcharge for benched and unbentched manholes are shown in Figure 4.11 and 4.12, respectively. The residence time is travel time subtracted from reach time delay, which is very small and nearly constant when compared to the travel time. The relationship between the residence time and the surcharge is rather similar to that of the travel time against the surcharge in terms of the effect of benching/unbenching and the surcharge threshold as described before.

## 4.6 Dispersive fraction

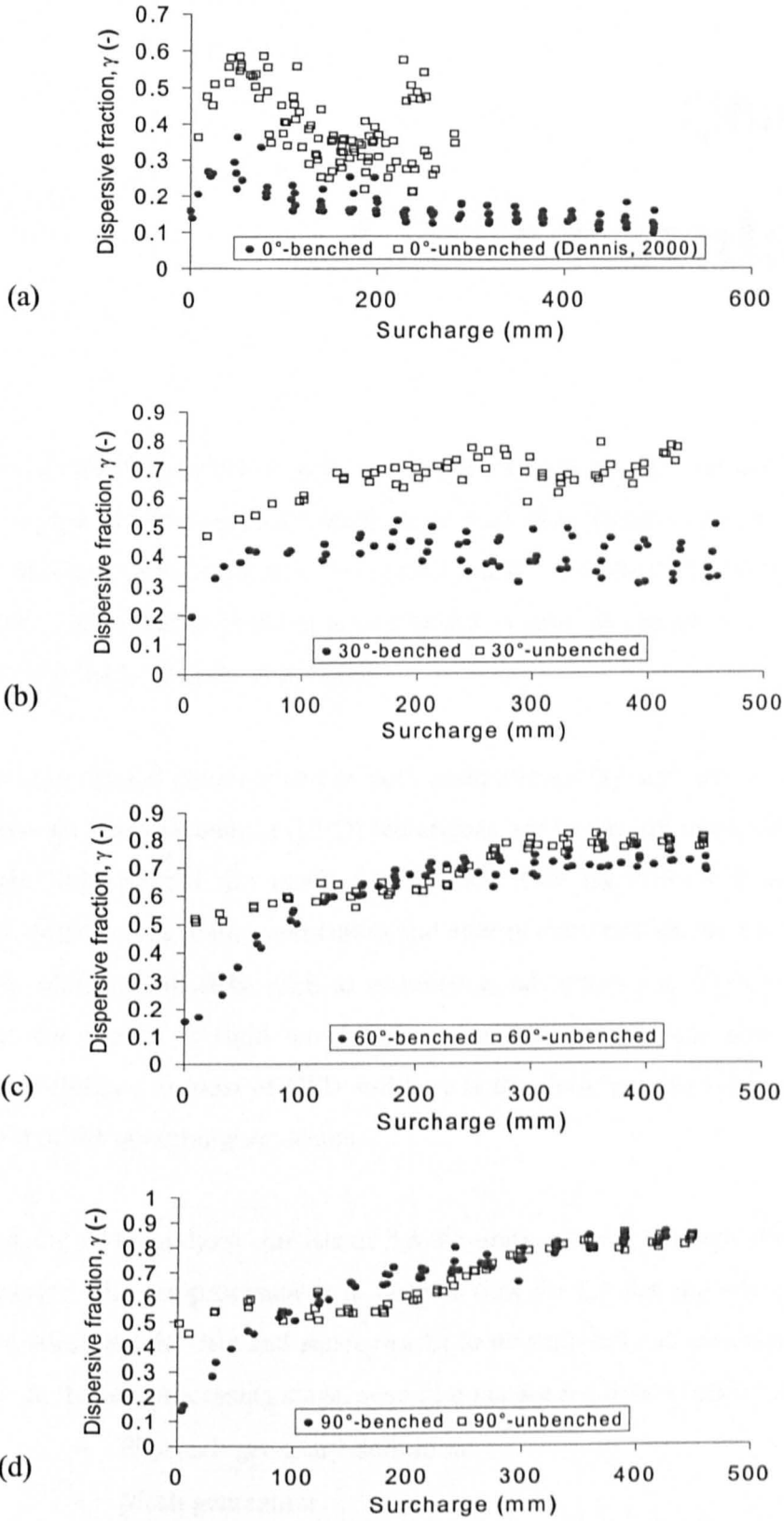
The ratio of the residence time ( $T$ ) and the travel time ( $\bar{t}$ ) is called “dispersive fraction” ( $\gamma = T/\bar{t}$ ) and is shown in Figure 4.13 for all of the flow rates and plane angles. The dispersive fraction non-linearly increased with surcharge when the plane angle was greater than  $0^\circ$ . However, the increase was limited below approximately 0.8. For  $0^\circ$  and  $30^\circ$  plane angles, the dispersive fraction from the unbentched manholes was always higher than that from the benched manholes at all surcharge levels. This was not true for the  $60^\circ$  and  $90^\circ$  plane angles. When the surcharge was lower than 100 mm, the unbentched manholes produced the higher dispersive fraction. Between 100 to 300 mm surcharge, the fraction from the unbentched manholes was similar to that from the benched manholes. Finally, at the surcharge higher than 300 mm, the dispersive fraction from both the benched and unbentched manholes were similar.



**Figure 4.11** Residence time from benched manholes: (a)  $0^\circ$ , (b)  $30^\circ$ , (c)  $60^\circ$  and (d)  $90^\circ$



**Figure 4.12** Residence time from unbent manholes: (a) 0° (after Dennis, 2000), (b) 30°, (c) 60° and (d) 90°



**Figure 4.13** Dispersive fraction over surcharge: (a)  $0^\circ$ , (b)  $30^\circ$ , (c)  $60^\circ$  and (d)  $90^\circ$



---

## Chapter 5

# CFD simulation

The aims of this chapter are to gain an insight into the energy loss coefficient due to changes in pipe direction across a manhole as well as to visualise mechanisms, such as velocity profile, vena contracta, jet profile and re-circulation, using basic CFD simulation. The simulated head loss coefficient is also compared with the coefficient obtained from the laboratory experiment.

Under the accelerated development of both computer ability and numerical algorithms, Computational Fluid Dynamics (CFD) techniques are becoming increasingly important to visualise and predict the result from either fluid theories or experiments. The governing equations of mass, momentum and energy conservation are mainly applied in CFD with additional models, such as turbulence, advection and diffusion, in order to determine the pattern of fluid movement and solute, particle and heat transfer. The numerical technique in most of CFD software is the finite control volume to discretise the domain of the governing equations.

In general, the CFD analysis consists of 3 main units, namely pre-processor, solver and post-processor. The pre-processor is to prepare data for the solving unit; subsequently, the solver calculates the data and sends results to be analysed and presented in the post-processor. In the pre-processing stage, several tasks are required in order; they are:

- Physical geometry definition
- Mesh generation
- Geometry boundary definition
- Boundary condition application
- Fluid property definition

The above 3 main units of using CFD software were adopted to present a preliminary study of the effect of changes in pipe directions on the energy losses and flow patterns due to surcharged manholes. Some of flow rates, surcharge levels and plane angles from the laboratory work were simulated by elementary models in CFD software. The resulting simulated value for the head loss coefficient might be an analogy to the experimental result. Moreover, the simulation of CFD could visualise what occurs in the manhole when the plane angles change.

## 5.1 Simulated energy losses

This preliminary investigation of energy losses due to surcharged manholes is to compare the loss coefficient obtained from laboratory with the value obtained from numerical simulation.

The head loss coefficient in this section was the difference of the simulated static pressure along the inlet and outlet pipes projected at the manhole centre divided by the pipe velocity head. The static pressure was obtained by running Fluent5, a CFD software product of Fluent Inc. The sequence of the CFD processes followed the 3 main steps: pre-processing, solving and post-processing.

### 5.1.1 Pre-processing

#### *Physical geometry and grid generation*

Gambit, another software package from Fluent Inc for geometry and grid generation, was applied to create and mesh the 388 mm diameter manholes with 88 mm diameter inlet and outlet pipes. Each manhole had the similar floor type, i.e. unbenched. The height of the manholes was varied and equal to the 88 mm pipe diameter plus surcharge levels, such as 200 mm and 400 mm. Another parameter investigation was concerned with changes in plane angle of pipe directions, which were studied at 0°, 30°, 60° and 90°. After the geometry of such a manhole including pipes was complete, meshing was the next step to generate cells in the manhole. For instance, Figure 5.1 shows the geometry and grid of the 60°-unbenched manhole with 400 mm surcharge, including grid quality. The quality of meshing is described in terms of "EquiAngle Skew" ( $Q_{EAS}$ ) defined as

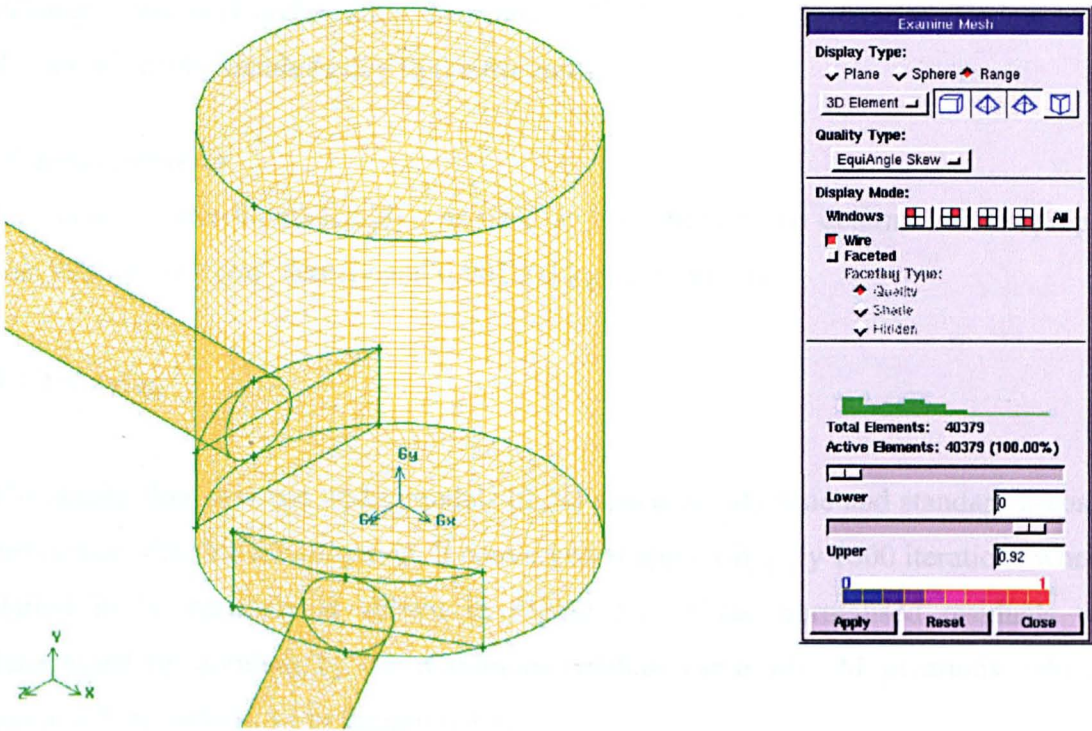
$$Q_{EAS} = \max \left\{ \frac{\theta_{\max} - \theta_{\text{eq}}}{180 - \theta_{\text{eq}}}, \frac{\theta_{\text{eq}} - \theta_{\min}}{\theta_{\text{eq}}} \right\}$$

where

$\theta_{\max}$  and  $\theta_{\min}$  = maximum and minimum between the edges of the element, degrees

$\theta_{\text{eq}}$  =  $60^\circ$  for triangular and tetrahedral elements and

=  $90^\circ$  for quadrilateral and hexahedral elements



**Figure 5.1** Meshed model and mesh quality (in the dialog) before CFD simulation for the  $60^\circ$ -unbenched manhole with 400 mm surcharge

By following the guide in Gambit, the element quality of the model in Figure 5.1 has the average value of  $Q_{EAS}$  between 0 to 0.6, represented by green colour in the dialog. This means that the grid quality is between fair and excellent, but if  $Q_{EAS}$  had been equal to 1.0, the grid model could be degenerate (Fluent Inc, 1999).

### ***Boundary conditions***

Each generated manhole would be simulated under conditions of 2 and 6 l/s flow rate, and  $-9.81 \text{ m/s}^2$  acceleration due to gravity on y-axis. These two flow rates were 0.33 and 0.99 m/s mean flow velocity, normal on the inlet surface. Also, the outlet was defined as “outflow” type with the flow rate weighting of 1. The skin of the inlet, outlet pipes and manhole was set as “wall” type with the roughness height of 0.003 mm for Perspex material (Chadwick and Morfett, 1995). Meanwhile, it was specified as zero at the surface of the manhole due to the frictionless.

### ***Material property***

In Fluent5, water-liquid (fluid) was used as a medium to be determined. Its property was  $998.20001 \text{ kg/m}^3$  density and  $0.001003 \text{ kg/ms}$  viscosity.

## **5.1.2 Solving**

The steady flow was run under models of 3D space, steady time and standard k-epsilon turbulence. For this investigation, it converged at approximately 1600 iterations where it started to be constant as shown in Figure 5.2. These normalised residuals were determined by dividing by the maximum residual value after  $M$  iterations, which is equal to 5 by default, as in Equation 5.1.

$$\bar{R}^{\phi} = \frac{R_{\text{iteration } N}^{\phi}}{R_{\text{iteration } M}^{\phi}} \quad (5.1)$$

where

$$R^{\phi} = \frac{\sum_{\text{cells } P} |\sum_{\text{nb}} a_{\text{nb}} \phi_{\text{nb}} + b - a_P \phi_P|}{\sum_{\text{cells } P} |a_P \phi_P|}$$

$\phi$  = a general variable in the conservation equation at a cell  $P$

$a_P$  = the centre coefficient

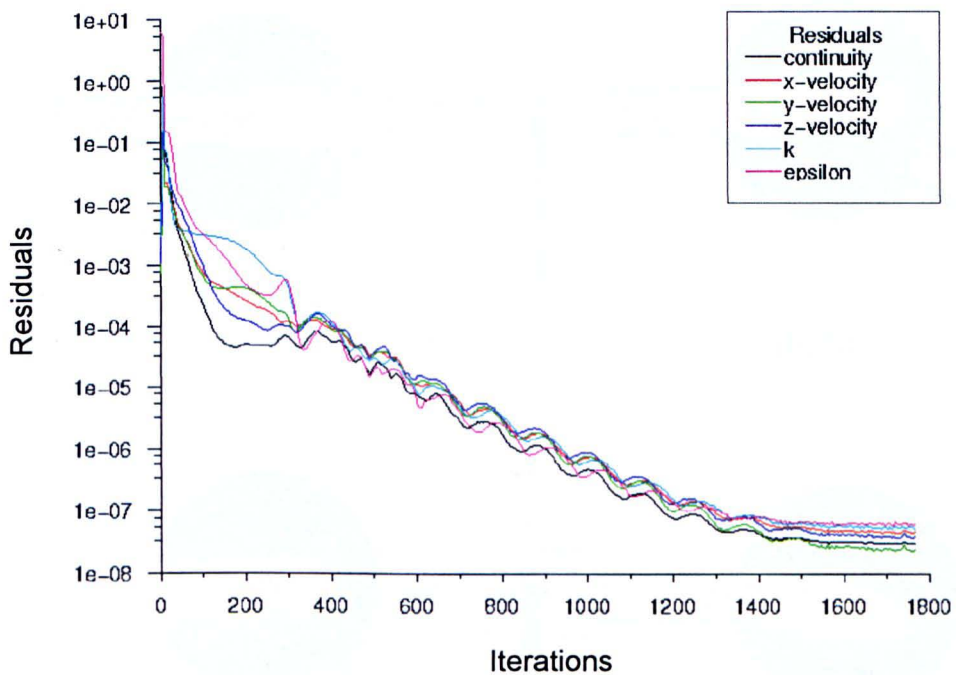
$a_{\text{nb}}$  = the influence coefficients for the neighbouring cells

$b$  = the contribution of the constant part of the source term,  $S_c$

### 5.1.3 Post-processing

#### *Velocity contour*

Figure 5.3 and 5.4 illustrate the plan and front views of the velocity contour along the inlet pipe centre, respectively. It is a visual result of the numerical simulation at 6 l/s flow rate and 400 mm surcharge at the plane angles of  $0^\circ$ ,  $30^\circ$ ,  $60^\circ$  and  $90^\circ$ . On the plan view (Figure 5.3), there seemed to be “short circuit” occurring in the manhole, when the plane angle increased, as shown by the connection of green colour. It denotes the velocity of approximately 0.5 m/s, connecting between the jet zone from the inlet pipe and the onset of the outlet pipe. Black arrows on Figure 5.3 were assumed to be short-circuit paths of the  $0^\circ$ ,  $30^\circ$ ,  $60^\circ$  and  $90^\circ$ -unbenched manholes with 6 l/s flow rate. It may infer that the longest black arrow should happen on the plane angle of  $0^\circ$ , while the shortest occurred on the  $90^\circ$  plane angle.



**Figure 5.2** Convergence of residuals at approximately 1600 iterations

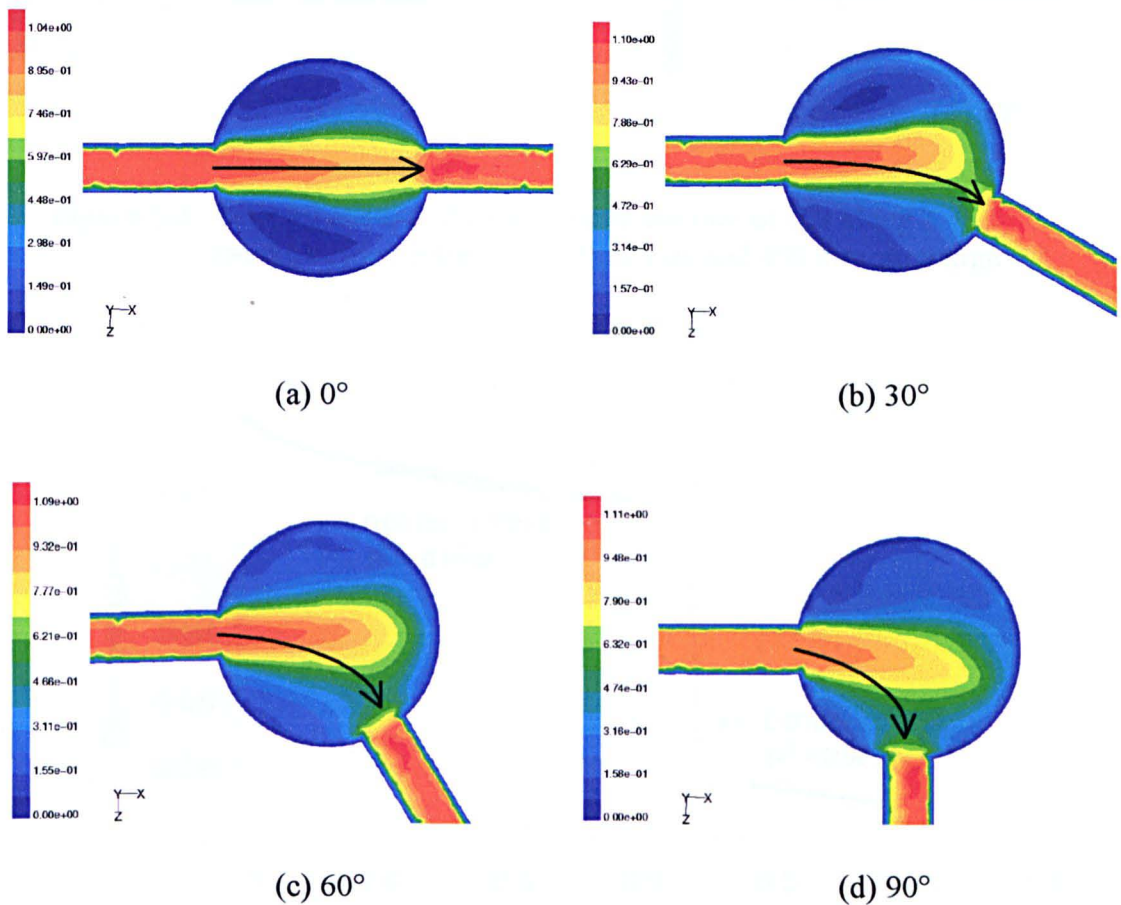
In addition to the short circuit, the plots in a vertical plane show the re-circulation in the surcharged manholes in Figure 5.4. Green colour that is on the wall against the inlet pipe presents the velocity in the y-direction and likely to be more when the plane angle became larger. This may be described in another way in which the almost stationary



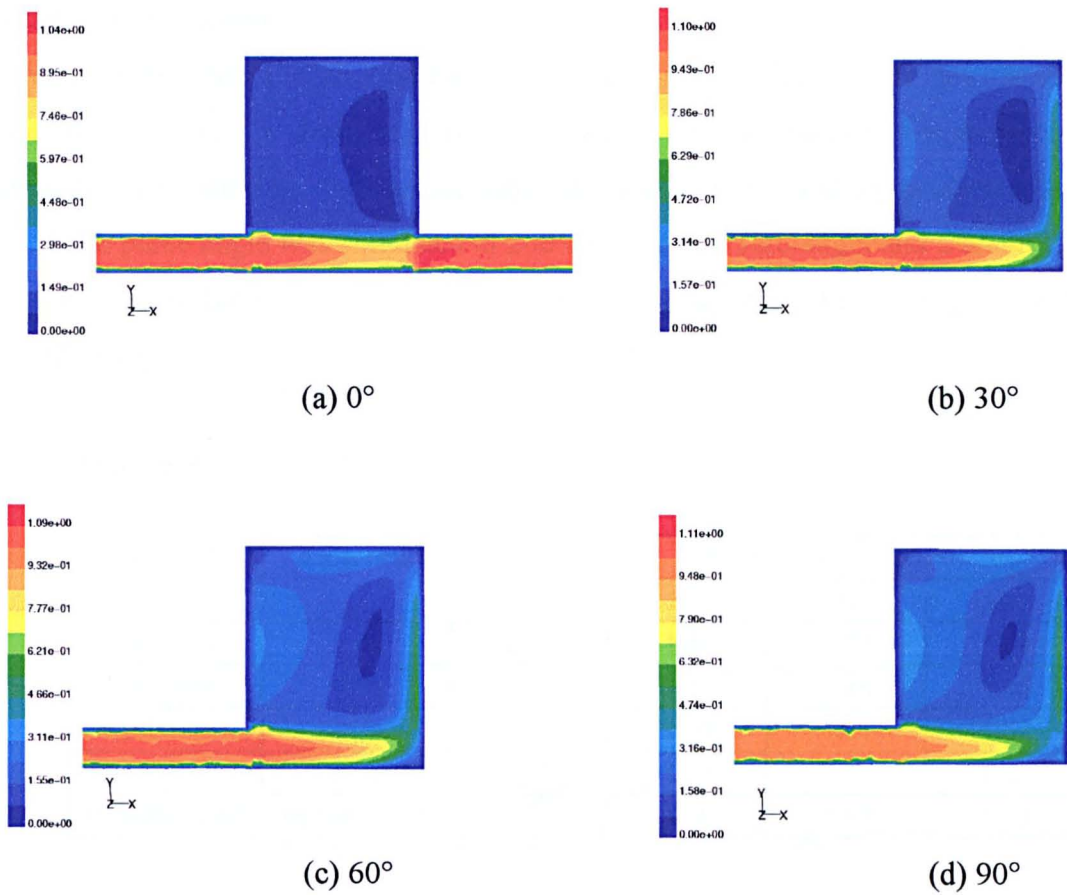
zone, i.e. dark blue denotation of the velocity between 0 up to 0.075 m/s, decreased when the plane angle increased.

### *Energy losses due to manholes*

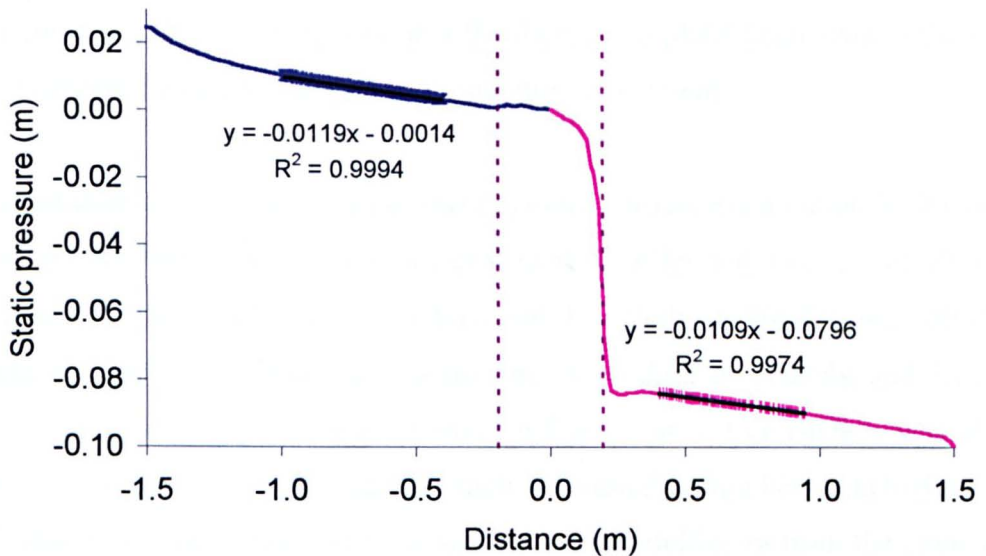
Figure 5.5 shows how to determine the energy losses due to a manhole. It was the figure analysed from the 90°-unbenched manhole with the configuration of 400 mm surcharge and 6 l/s flow rate. Energy losses at the beginning and the end of the inlet and outlet pipes are non-linearly related to the pipes. Therefore, only some parts in the figure from all of the upstream and downstream static pressure profiles are used in order to calculate the best linear function. In this case, the best fit is presented as  $R^2 = 0.9994$  and  $0.9974$  for upstream and downstream pressure profiles, respectively. The difference of the y-intercept would be representative of the energy loss due to a manhole, which is  $(-0.0014) - (-0.0796)$  m for this example.



**Figure 5.3** Plan of velocity contour in the unit of m/s along the pipe centre of 6 l/s flow rate and 400 mm surcharge



**Figure 5.4** Velocity contour at front view in the unit of m/s along the inlet pipe centre of 6 l/s flow rate and 400 mm surcharge



**Figure 5.5** Using a range of a pressure profile to determine the energy loss of the 90°-unbenched manhole with 6 l/s flow rate and 400 mm surcharge

### ***Head loss coefficient (K)***

Having determined the energy loss, the head loss coefficient was calculated from Equation 2.5. All the head loss coefficients for this preliminary investigation were simulated from varying plane angle, surcharge and flow rate and are presented in Table 5.1. Each plane angle was simulated at 200 and 400 mm surcharge, and 2 and 6 l/s flow rate. It seemed that the simulated coefficient increased when the plane angle and flow rate increased, but decreased when surcharge increased.

**Table 5.1** Simulated head loss coefficient

Surcharge	Flow rate	Plane angle			
		0°	30°	60°	90°
200 mm	2 l/s	0.72	1.42	1.73	1.89
200 mm	6 l/s	0.73	1.45	1.76	1.93
400 mm	2 l/s	0.71	1.33	1.41	1.54
400 mm	6 l/s	0.72	1.36	1.43	1.56
Average head loss coefficient		0.72	1.39	1.58	1.73

## **5.2 Conclusion**

After simulating the additional flow rates, the change in coefficient remained almost constant. Table 5.2 presents the comparison of the average head loss coefficient, from its above rows in Table 5.1. It seemed that the increase in plane angle caused the higher simulated loss coefficient due to greater momentum movement.

CFD may be used as a tool to design a sewer system, particularly a manhole. It can help visualise the fluid flow very well in terms of velocity profiles and a vena contracta at the outlet pipe, but only some cases (Asztely and Lyngfelt, 1996; Dennis, 2000) are acceptable to predict the head loss coefficient. According to Asztely and Lyngfelt (1996), a symmetrical manhole with a small influence on a free surface was able to simulate flow pattern and energy losses, which was tested with a half-benched manhole and high surcharge. From this study, the simulated loss coefficient from the plane angle of 0° might be sufficiently applied since the figure was a little greater than the coefficient from the laboratory, whereas the rest offered smaller values than the measurement due to the lack of swirling determined in the standard k-ε model. Hence,



RNG k- $\epsilon$  model might be employed instead because it allows for the swirling effect (Fluent Inc., 1998). This further study is probably a little beyond this preliminary investigation which was determined from only the basic mathematical models.

**Table 5.2** Head loss coefficient from simulation and measurement

Plane angle of Unbenched manholes	Average head loss coefficient	
	CFD	Laboratory
0°	0.72	0.51*
30°	1.39	2.22
60°	1.58	2.02
90°	1.73	1.97

\* Dennis (2000)

---

# Chapter 6

## Discussion

This chapter comprises the comparison of the results and the improvement of the downstream concentration prediction. The experimental and simulated results from CFD of the head loss coefficient are also compared. The quantified travel time as a parameter in mixing in Chapter 4 is applied to generate predictive equations. Dispersive fraction, another parameter, is also used to describe how a solute is mixed in a manhole. Subsequently, energy dissipation is introduced to demonstrate the relationship of the head loss due to a manhole and residence time in the manhole. Finally, Cells in ADZ model are explained in order to increase an ability of software for more correct prediction of downstream concentration profiles than only a single cell of ADZ did.

### 6.1 Head loss coefficient

The average head loss coefficient was determined from the slope of a trend line through co-ordinates representing the estimated head losses and the velocity head with the best  $R^2$ , as shown in Figure 4.6. This means was also employed by Marsalek (1984) and Dennis (2000).

#### 6.1.1 Influence of benching

Table 6.1 presents the average head loss coefficient ( $K$ ) for the benched and unbenched manholes, in which the plane angles are  $0^\circ$ ,  $30^\circ$ ,  $60^\circ$  and  $90^\circ$ . It is clear that the loss coefficients of benched manholes were smaller than those of the unbenched manholes. This may be caused by the benching which confines almost three quarters of the jet flow and reduces the mixing zone in the manholes (Saiyudthong and Guymer, 2002;

Pedersen and Mark, 1990). For instance, the loss coefficient of the 0°-benched manhole accounted for 0.27, which is nearly half as much as the coefficient of the 0°-unbenched manhole. This may conclude that the benching is a major reduction of energy losses. Nevertheless, the influence of benching did not seem as important when the plane angle became larger.

**Table 6.1** Head loss coefficient (K)

Plane angle ( $\theta$ )	Head loss coefficient (K)	
	Benched	Unbenched
0°	0.27	0.51*
30°	1.24	2.22
60°	1.49	2.02
90°	1.50	1.97

\* Dennis (2000)

### 6.1.2 Influence of changes in plane angle

The head loss coefficient clearly increased when the plane angle increased, especially for the benched manholes, but not for all plane angles of the unbenched manholes as shown in Figure 6.1. However, for the benched manholes, the loss coefficient was greater while the plane angle increased. For example, it rose from 0.27 to 1.24, 1.49 and finally 1.50 once the angle changed from 0° to 30°, 60° and 90°, respectively. Momentum transfer may be the key to the increase in the loss coefficient for this case, change in flow direction. However, apart from jet flow confined by benching and momentum transfer due to changes in plane angle at the benching, Howarth and Saul (1984) claimed that the coefficient might increase several times, for example from 0.15 up to 1.0, when swirl occurred at the surface water. Lindvall (1984), Pedersen (1986), and Kusuda and Arao (1996) also mentioned that swirling motion or oscillation on the free water surface caused the increase of head losses. Nevertheless, a magnitude of the motion was not justified yet. Therefore, the figures of the coefficients might be described that the effect of momentum transfer on the benched/unbenched manholes was likely to increase when the plane angle became larger.

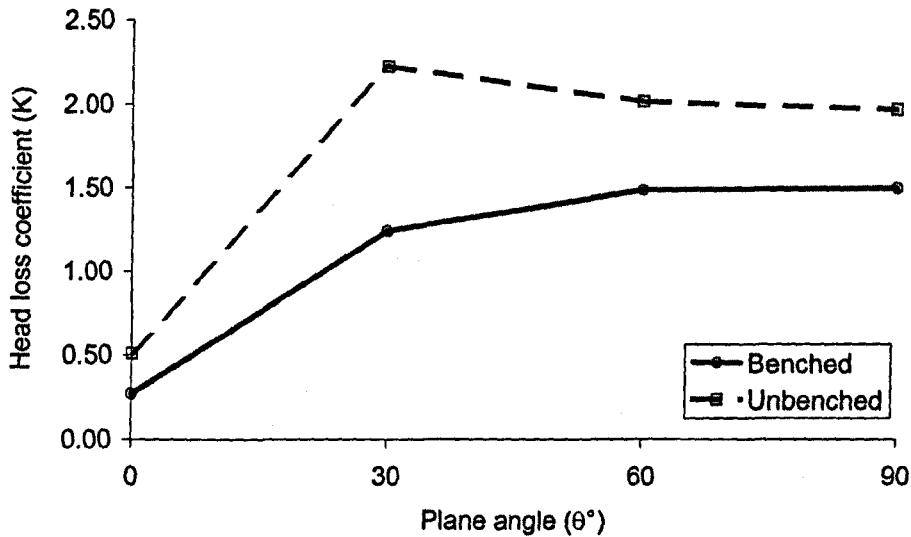


Figure 6.1 Observed head loss coefficient based on the plane angles

### 6.1.3 Comparison of head loss coefficient to previous work

The head loss coefficient obtained from the experiment was compared to the result from Equation 2.8 (Young et al, 1999) as presented in Chapter 2. Several terms in the equation would be replaced by particular constant values, which came from the experimental configurations, such as  $C_1 = 0.36$  due to the relative manhole diameter ( $D_m/D_o$ ) greater than 4.0;  $C_2 = 0.82$  when the relative water depth ( $d_{mH}/D_o$ ) larger than 3.0; and the benching configuration ( $\omega$ ) = 1.0 and 0.75 for the unbenched manholes and the benched manholes, respectively. Consequently, Equation 2.8 can be rewritten as

$$K_I = ((0.36)(0.82)C_3 + C_4)(0.75) \quad \text{for benched manholes}$$

$$K_I = (0.36)(0.82)C_3 + C_4 \quad \text{for unbenched manholes}$$

where

$$C_3 = 1 + \frac{(\cos \psi)(0.85)}{(3.2)^{0.3}}$$

$$C_4 = 1 + [(1 + 2 \cos \psi)]$$

The resulting values of  $C_3$  and  $C_4$  are presented in Figure 6.2; subsequently the calculated loss coefficient is shown in Table 6.2 and compared with the head loss coefficient obtained from the laboratory in Figure 6.3. It seemed that the coefficient from the equation was much lower at the plane angles of  $30^\circ$  and  $60^\circ$ . This might be caused by the fact that  $C_3$ , the effect of flow rate, connecting angle and elevation of the inlet pipe, was determined from scattered data due to air entrainment and turbulence (Young, et al, 1999) for use with all kinds of manholes. Meanwhile, the coefficient of  $90^\circ$  from the equation was larger than that of the experiment because  $C_4$  increased extremely high after the plane angle of  $60^\circ$  as in Figure 6.2. Consequently, the equation can estimate the head loss coefficient for all surcharge levels, whereas the observed loss coefficient from the experiment does not and was based on the concept that the head loss coefficient remained constant. This difference may make the coefficient from the equation different from the experiment.

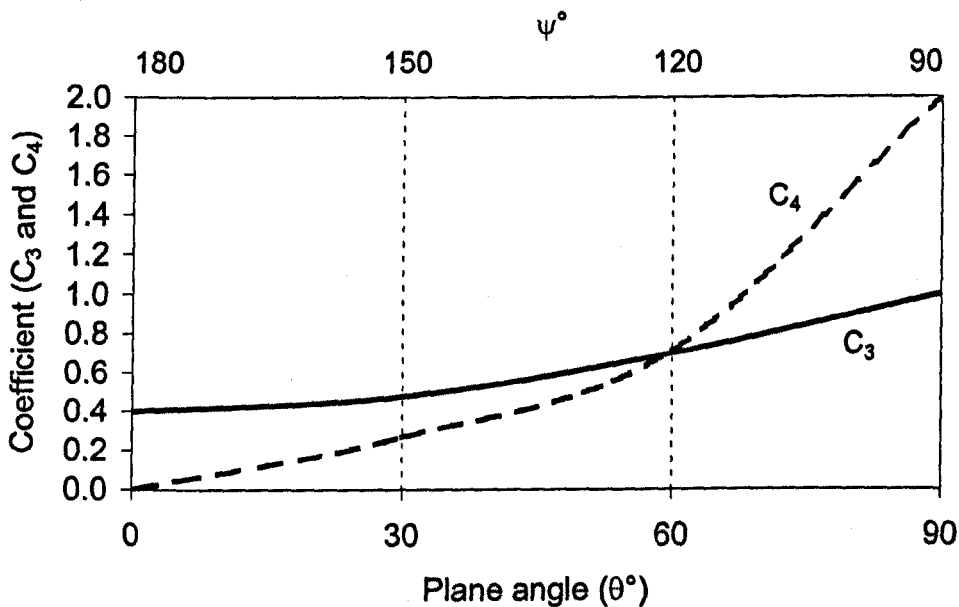
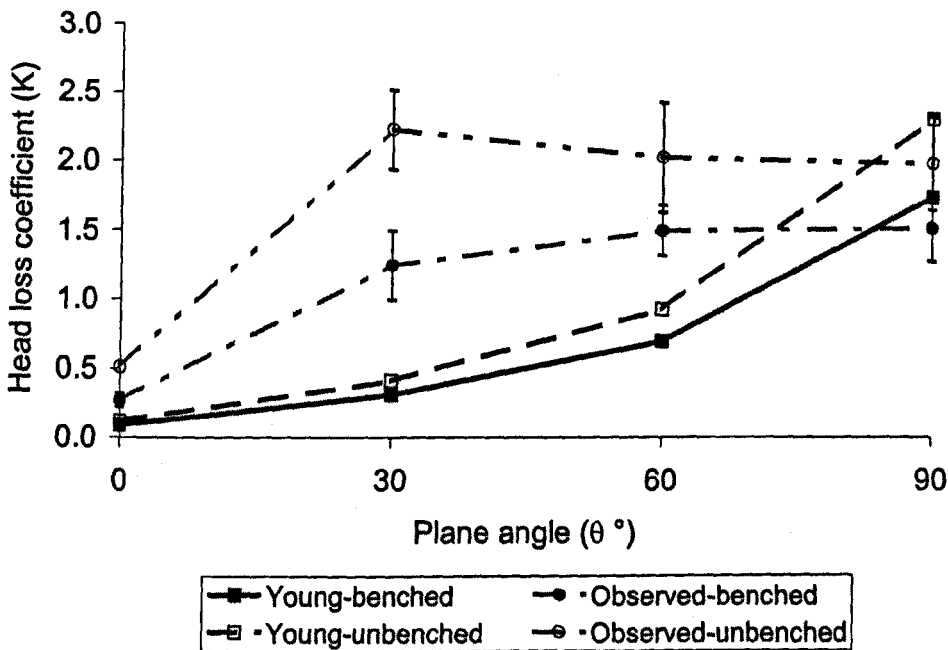


Figure 6.2 Coefficient ( $C_3$  and  $C_4$ )

**Table 6.2** Head loss coefficient calculated from the equation (Young et al, 1999)

Plane angle ( $\theta$ )	Head loss coefficient (K)	
	Benched	Unbenched
0°	0.09	0.12
30°	0.31	0.41
60°	0.69	0.92
90°	1.72	2.30

**Figure 6.3** Comparison of the head loss coefficient from Young's equations and from the experiment

In addition to the comparison between the head loss coefficient from the experiment and from Young's equations, the predicted loss coefficient obtained from Pedersen and Mark (1990) was also compared. The loss coefficient would be calculated, compared and based on the same physical configurations, i.e. the similar ratio of manhole and pipe diameters at 4.0, the same floor type conditions: flat, half and full (see detail in Figure 2.9) and surcharge levels over 3.2 times pipe diameter. The latter seems not to affect the head loss coefficient in the equation from Pedersen and Mark (1990), while the general equation from Young et al (1999) allowed an addition due to the effect of surcharge on the prediction of the head loss coefficient. The result of the calculated head coefficient

is shown in Table 6.3. It seemed that the predicted loss coefficient from Pedersen and Mark (1990) was closer to the coefficient obtained in laboratory and almost twofold the coefficient from Young's equation under flat floor type condition. However, under other floor type conditions, it was not greatly different between the coefficient predicted from these equations.

Consequently, this probably confirmed that the equations from Young et al (1999) only predicted the head loss coefficient well under general configuration of manholes, such as straight pipe and benching. In contrast, it poorly predicted the head loss coefficient from complicated configurations, for example unbenched manholes with changes in pipe directions. More importantly, Young et al (1999) also claimed that some terms in the equations were generated from scattered data obtained from manholes, in which flow condition was more turbulent.

**Table 6.3** Comparison of head loss coefficient calculated from Pedersen and Mark (1990), and Young et al (1999)

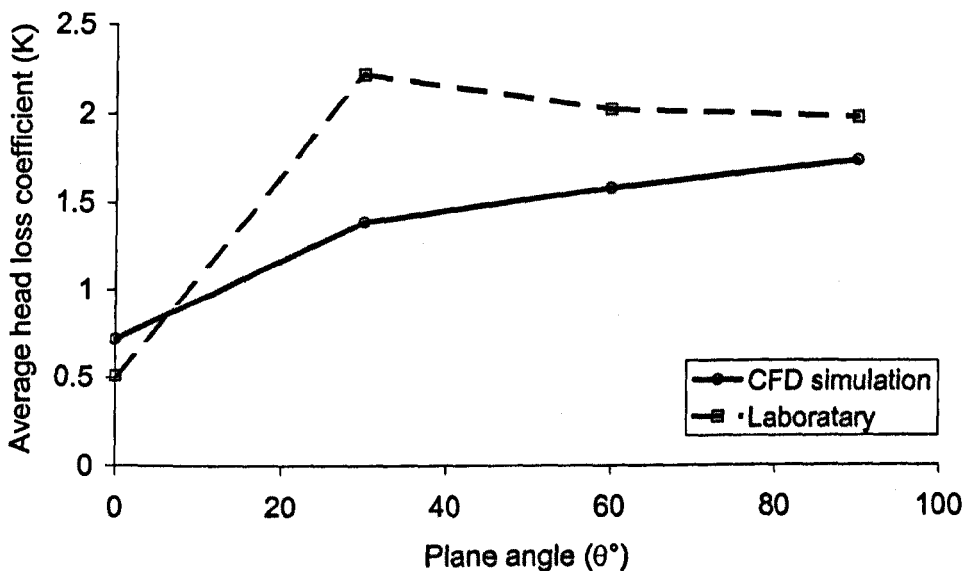
Floor type	Flat	Half	Full
K from Pedersen and Mark, 1990	0.48	0.28	0.10
K from Young et al, 1999	0.28	0.22	0.12

#### 6.1.4 Comparison between experiment and CFD simulation

The CFD simulated loss coefficient can also be compared to that from the measurement in the laboratory. Figure 6.4 presents that the simulated loss coefficient (see detail how to determine the coefficient in Chapter 5) was smaller than the measured coefficient in the experiment, except the coefficient at plane angle of  $0^\circ$ . The simulated coefficient of the  $0^\circ$ -unbenched manhole was greater than the measured coefficient, i.e. 0.72 and 0.51, probably because the top wall did not serve properly as the water surface. There was greater energy losses than the real condition. On the other hand, when the plane angle was equal to or greater than  $30^\circ$ , the simulated loss coefficient was less than the measured coefficient. This might be caused by the fact that the momentum conservation equation and the standard k- $\epsilon$  model could not simulate the flow pattern well, especially at the water surface on this physical model. The water surface was treated as a plane

wall, rather than a free flow surface, where the swirling or oscillation occurs. As a result, the effect of the swirling or oscillation, as mentioned in previous section, was negligible.

To improve the head loss coefficient obtained from CFD simulation, RNG  $k-\epsilon$  model and the free flow surface model might be used instead, rather than the standard  $k-\epsilon$  model in FLUENT5 software. The RNG  $k-\epsilon$  model was derived from the standard  $k-\epsilon$  model to deal with the effect of swirl on turbulence (Fluent Inc., 1998) by means of re-normalisation group (RNG), a mathematical technique. Sarker (2000) physically modelled a free surface over broad-crested weir and numerically simulated it by using the free surface model of water and air by Fluent, the CFD commercial software. The physical model was simulated not only by the standard  $k-\epsilon$  model, but also by the RNG  $k-\epsilon$  model in order to compare the results. Consequently, it was found that the RNG  $k-\epsilon$  model could improve the predicted water depth on the weir crest closer to the measured depth than the standard  $k-\epsilon$  model did.



**Figure 6.4** Comparison of the head loss coefficient from CFD simulation and measurement



---

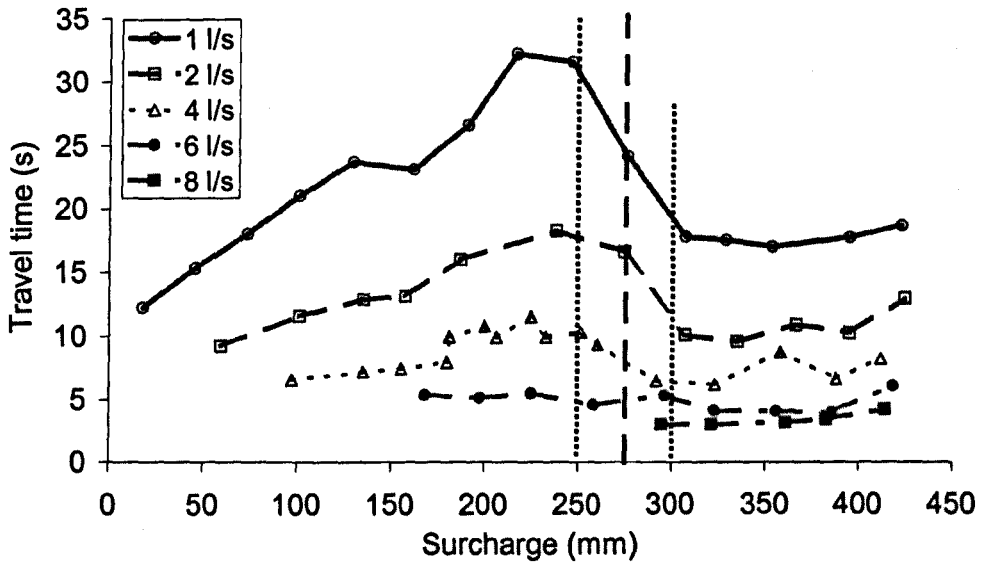
## 6.2 Travel time

On some figures of the travel time against surcharge in Chapter 4, it was likely that the travel time linearly increased when the surcharge increased, e.g. Figure 4.8 (b), (c) and (d). Once the surcharge reached a transient zone, the travel time decreased and remained constant after that. Therefore, to predict the travel time, it may require 2 equations to predict travel time for each manhole's configuration before/after the transient zone. The following section will briefly describe how to obtain the equations for the predicted travel time from a surcharge level and flow rate. Moreover, the travel time may be also predicted from an equation developed by the technique of multiple regression, without the transient zone determined.

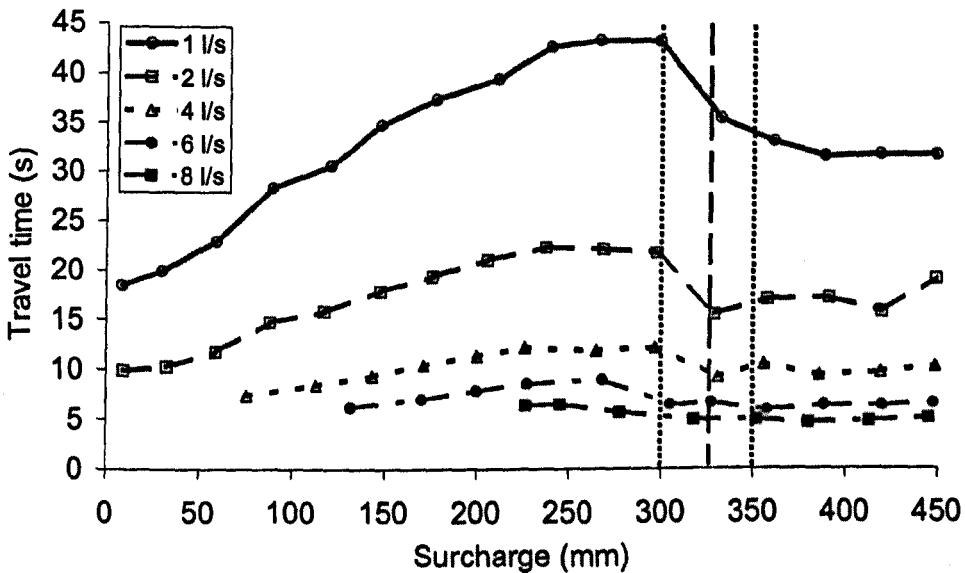
### 6.2.1 Predictive equation using threshold surcharge

#### *Threshold surcharge*

Figure 6.5 and 6.6 present threshold surcharge lines, the average of the lower and upper surcharge values in the transient zone. For example, the 30° and 60°-unbenched manholes have the threshold lines at approximately 275 mm and 325 mm, respectively. These lines are obtained from the lower and upper arbitrary surcharge values in the transient zones, which are approximately 250 mm and 300 mm for the 30°-unbenched manhole, and 300 mm and 350 mm for the 60°-unbenched manhole.



**Figure 6.5** Threshold surcharge at approximately 275 mm within the transient zone of the travel time for the 30°-unbenched manhole



**Figure 6.6** Threshold surcharge at approximately 325 mm within the transient zone of the travel time for the 60°-unbenched manhole

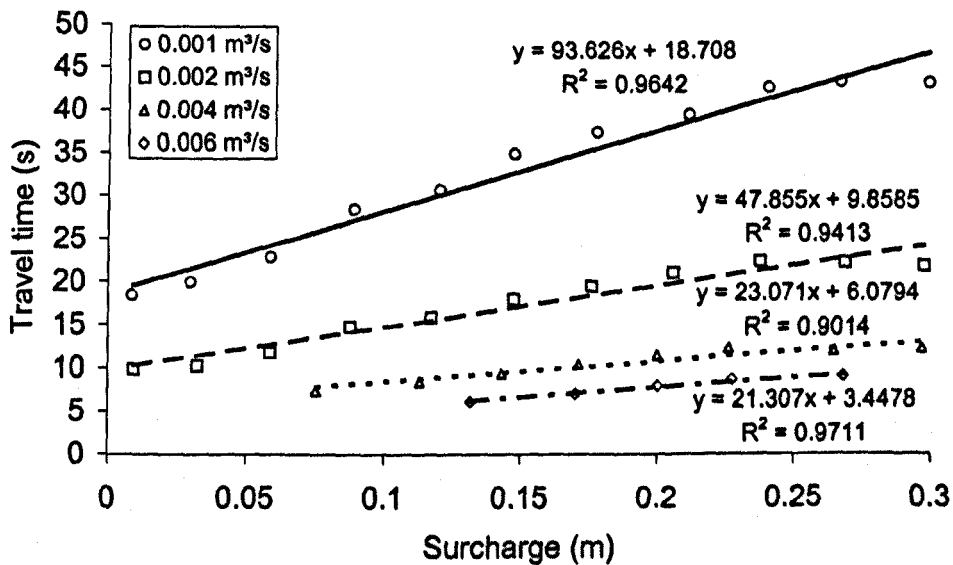
**Equations for pre-threshold surcharge**

To predict travel time at the pre-threshold surcharge, several linear relationships between travel time and surcharge are plotted by means of the least square for such a flow rate as shown in Figure 6.7. It was, for example, the relationship between the travel time and pre-threshold surcharge from the 60°-unbenched manhole. All values of the slope and y-intercept from the linear equations were subsequently searched for a correlation with regard to flow rates. Figure 6.8 and 6.9 illustrate the linear relationships between the figures of the slope, and y-intercept and reciprocal flow rate, respectively. It also shows 2 linear equations, together with the good values of R<sup>2</sup>. Afterwards, the linear equation from the values of the slope and y-intercept were replaced to multiply and add a surcharge factor, respectively. For example, the function of travel time, surcharge and flow rate of the 60°-unbenched manhole was written as Equation 6.1, following the approach of Guymer and O'Brien, 2000.

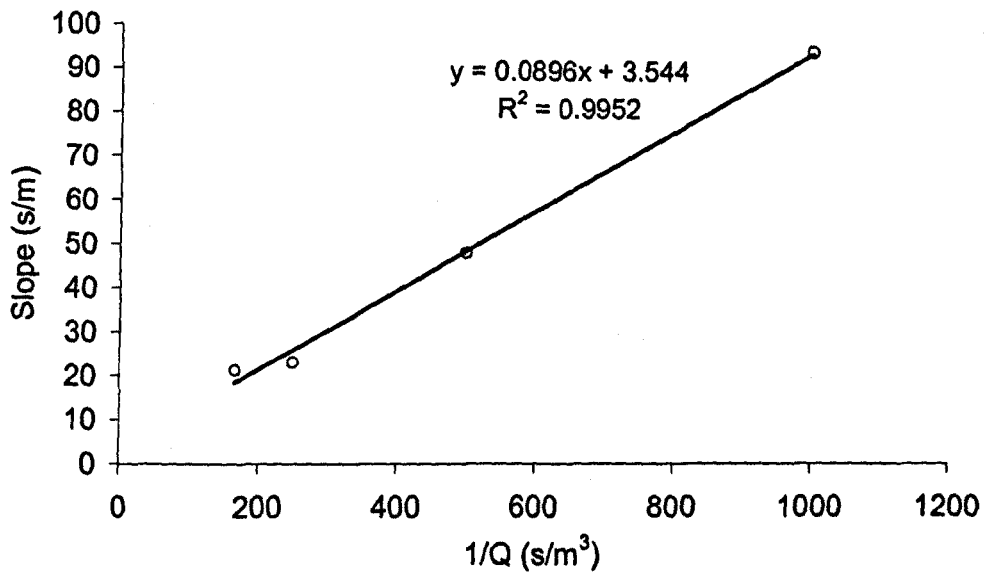
$$\bar{t}_{60^\circ\text{-unbenched}} = \frac{0.09(S)}{Q} + 3.544(S) + \frac{0.018}{Q} + 1.0 \quad (6.1)$$

- where
- $\bar{t}$  = travel time (s)
  - S = surcharge (m)
  - Q = flow rate (m<sup>3</sup>/s)

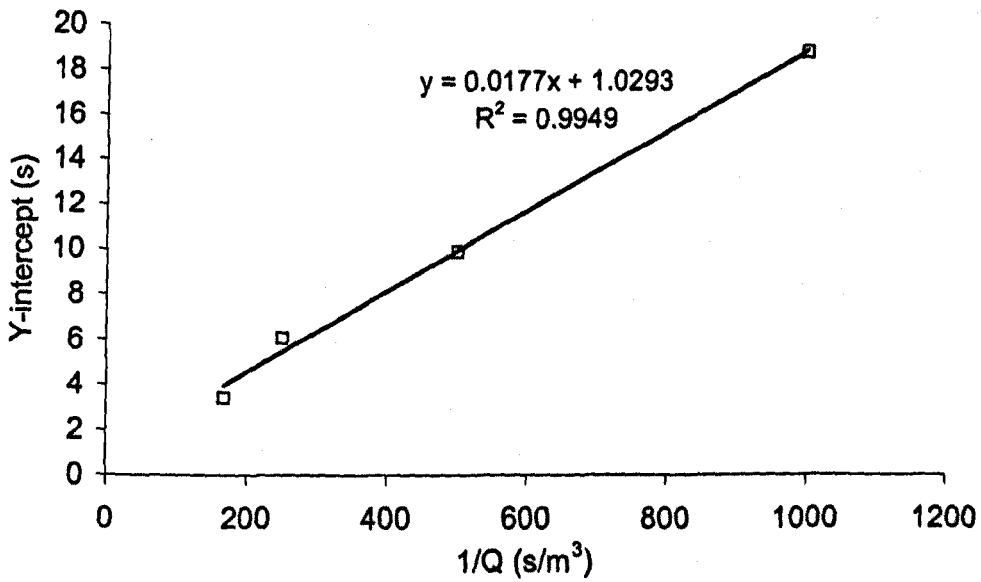
Also, this equation was employed to generate travel time in order to be compared with observed travel time as shown in Figure 6.10.



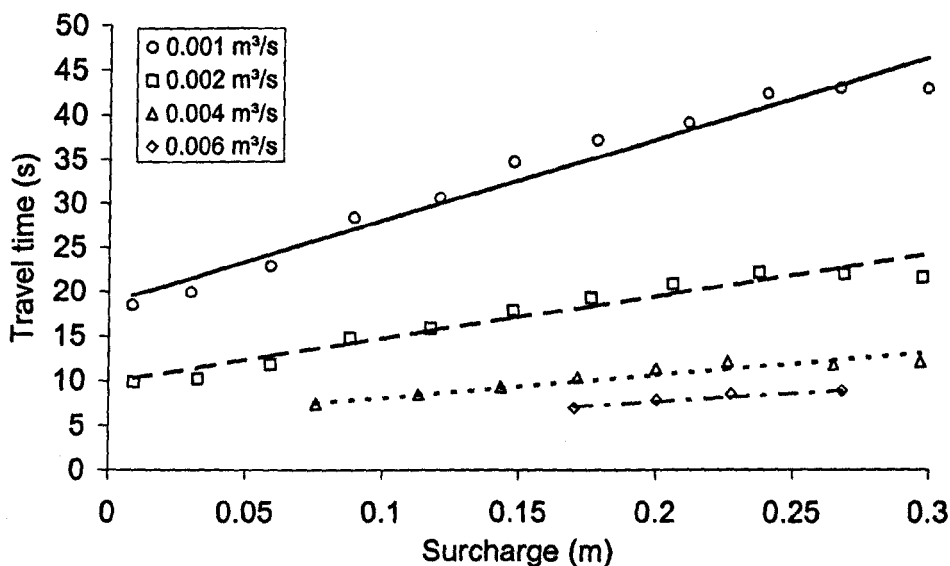
**Figure 6.7** Linear relationship between travel time and pre-threshold surcharge of the 60°-unbenched manhole



**Figure 6.8** Correlation between values of the slope and reciprocal flow rate



**Figure 6.9** Correlation between value of the y-intercept and reciprocal flow rate



**Figure 6.10** Comparison between observed travel time from ADZ optimised and predicted travel time (presented by lines) from Equation 6.1

#### *Equations for post-threshold surcharge*

Besides the equation of the travel time taking place prior to the threshold surcharge, travel time after the threshold was also related to an inverse flow rate, where the travel time was independent of surcharge. Figure 6.11 shows the correlation between the travel time and an inverse flow rate as a power function for the 0°-benched/unbenched and 30° benched/unbenched manholes, including  $R^2$ . Also, the standard error of the travel time is presented, which seemed to be greater in the unbenched manholes.

#### *Predicted travel time*

Table 6.4 shows a summary of travel time equations developed using threshold surcharge concepts. It also illustrates that for some manhole configurations, predictive equations have not been developed (represented by "-"), since the threshold surcharge could not be specified. This was because either the threshold level was insignificant (represented by "\*") or the surcharge threshold was beyond the experimental surcharge limit (represented by "&"). For example, at the 0°-unbenched situation (Figure 4.8 (a)), a threshold value around 50 mm might be suggested. However, this was only evident for the lowest flow rate of 1.0 l/s and there are only 2 cases where the surcharge was less than 50 mm. With surcharge limited information, little confidence can be given to the identification of a threshold level for this case. Further detailed studies would be required to provide evidence of a threshold level. On the other hand, for the 90°-

unbenched situation (Figure 4.8 (d)), the studies up to maximum possible surcharge of 450 mm were performed. In this situation, the results suggest that the threshold value has not been reached.

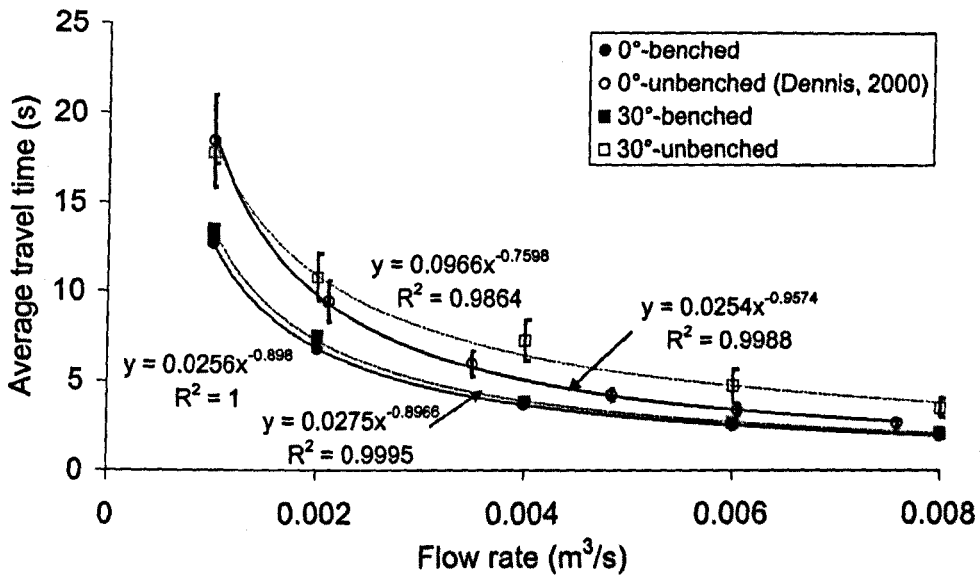


Figure 6.11 For post-threshold surcharge, travel time related to reciprocal flow rate

Table 6.4 Equations to predict travel time

Plane angle (θ°)	Floor type	Travel time (Tbar)		Threshold mm
		Pre-threshold	Post-threshold	
0	benched	-	Tbar = 0.0256Q <sup>-0.90</sup>	*
	unbenched	-	Tbar = 0.0254Q <sup>-0.98</sup>	*
30	benched	-	Tbar = 0.0275Q <sup>-0.90</sup>	*
	unbenched	Tbar = 0.072S/Q+13.75S+0.011/Q+0.7	Tbar = 0.0966Q <sup>-0.78</sup>	275
60	benched	Tbar = 0.041S/Q-4.726S+0.015/Q+1.4	-	&
	unbenched	Tbar = 0.09S/Q+3.544S+0.018/Q+1.0	Tbar = 0.0745Q <sup>-0.88</sup>	325
90	benched	Tbar = 0.06S/Q-3.982S+0.014/Q+1.8	-	&
	unbenched	Tbar = 0.123S/Q-20.55S+0.016/Q+4.0	-	&

Note

- Tbar = travel time (s)
- S = surcharge (m)
- Q = flow rate (m<sup>3</sup>/s)
- = no equations since threshold cannot be specified
- \* = insignificant threshold
- & = cannot specify threshold due to experimental surcharge limit

Nevertheless, for the specifiable threshold, the predictive equations for travel time would be presented in the formats of

$$\bar{t} = A \frac{S}{Q} + BS + \frac{C}{Q} + D \quad \text{pre-threshold surcharge}$$

$$\bar{t} = a Q^b \quad \text{post-threshold surcharge}$$

where

A, B, C, D, a and b = constant

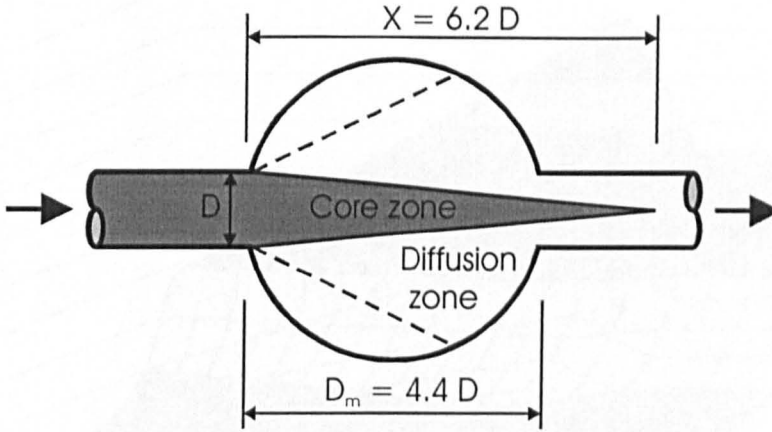
$\bar{t}$  = Tbar = travel time (s)

S = surcharge level (m)

Q = flow rate (m<sup>3</sup>/s)

Due to a change in the dominant mixing process between advection and dispersion when surcharge levels increased, a surcharge threshold was used as an interface between the processes. For example, the 30° and 60° unbenched manholes had a surcharge threshold at approximately 275 mm and 325 mm, respectively. It may interpret that before the 275 mm surcharge, the mixing in the manhole was dominated by dispersion mechanism, in which travel time almost linearly increased with surcharge. Meanwhile, after the 275 mm surcharge, it was presented that advection process was dominant and travel time was independent of surcharge as can be predicted by the equation for post-threshold for the 30°-unbenched manhole in Table 6.4.

Also, the equations indicated that both the surcharge and flow rate could affect the travel time when the plane angle was equal to or greater than 30° without benching, while only flow rate influenced the travel time when the plane angle was equal to or less than 30° with benching. This may be a result of the core zone and diffusion zone within jet flow pattern. In the case of the travel time prior to the threshold, the mixing volume in the manhole increased with the surcharge and was dominated by the diffusion zone (see Figure 2.7). In contrast, the travel time after the threshold seemed to be dominated by the core zone of jet as shown in Figure 6.12. The core flowed through the manhole without more effect of diffusion mixing since the core's length (6.2D) was greater than the diameter of the manhole ( $D_m = 388$  mm), where D was the inlet pipe diameter of 88 mm (see submerged jet theory in Chapter 2).



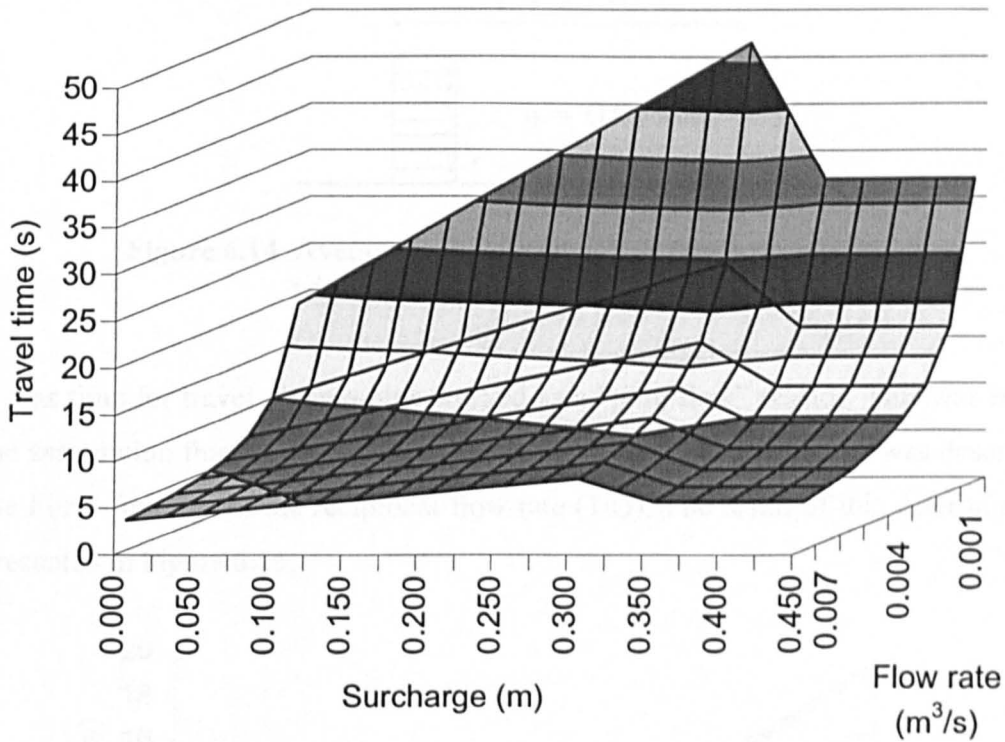
**Figure 6.12** Longer core zone than manhole diameter

This effect also happened at the  $30^\circ$  and  $60^\circ$ -unbenched manhole, in which the travel time could be determined from both types, i.e. for pre- and post-surge threshold, of the equations in Table 6.4 due to the threshold surge occurring within the experimental range of surge. It might suggest that after the surge was above the threshold, the travel time was independent of the surge and influenced by the dominant core zone. In other words, it may be interpreted that after the surge passed the threshold, it was beyond the certain effective mixing volume by the diffusion of solute. Therefore, the surge no longer affected the travel time, which depended on only the flow rate. For example, the equations to predict the travel time of the  $60^\circ$ -unbenched manhole were calculated and plotted in 3 dimensions in Figure 6.13. For the predicted travel time at the threshold surge in the figure, the travel times before and after one surge step of the surge threshold were averaged.

#### ***Travel time from post-threshold and from “plug flow”***

To compare the travel time from the post-threshold surge of the  $0^\circ$  and  $30^\circ$ -benched/unbenched manholes on a same standard, the equations of travel time in Table 6.4 were imposed to be functions of the flow rate power of exactly  $-1$ . The concept of the functions was developed from Equation 6.2 and Figure 6.14.





**Figure 6.13** Prediction of travel time for pre- and post-threshold surcharge, in which the threshold is at 0.325 m for the 60°-unbenched manhole

$$Q = VA \quad (6.2)$$

$$V = L/t$$

$$t = LAQ^{-1}$$

or  $t = c Q^{-1}$

where

$$Q = \text{flow rate (m}^3/\text{s)}$$

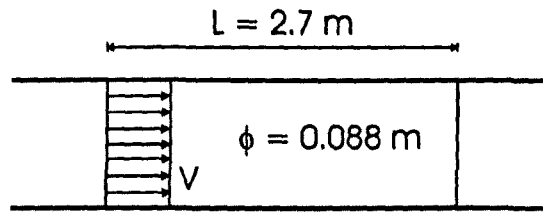
$$V = \text{average flow velocity in pipe (m/s)}$$

$$A = \text{area of the pipe (m}^2\text{)}$$

$$L = \text{distance (m)}$$

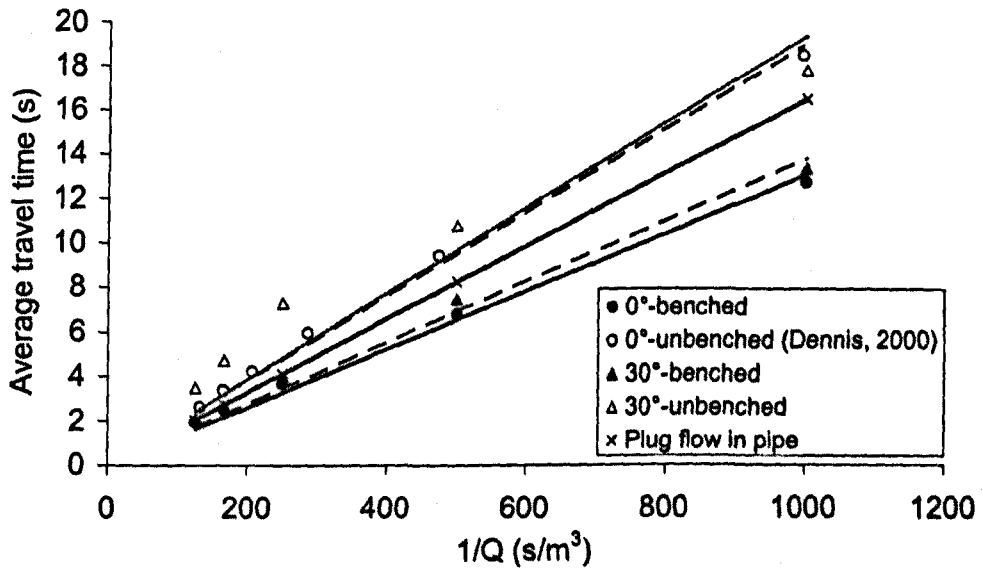
$$c = \text{constant}$$

$$t = \text{time for travel (s)}$$



**Figure 6.14** Average flow velocity ( $V$ ) in 0.088 m diameter pipe with distance of 2.7 m

It was time for travel along a pipe worked as a “plug flow” reactor. This was based on the assumption that the travel time from the post-threshold surcharge was described on the linear function of the reciprocal flow rate ( $1/Q$ ). The result of this determination is presented in Figure 6.15.



**Figure 6.15** Trend lines from the co-ordinate of reciprocal flow rate and average travel time

The equations of the trend lines in Figure 6.15 and  $R^2$  are presented in Table 6.5. The ideal of travel time from “plug flow”, was also placed in the table as presented by the item of plug flow in pipe. It was calculated from  $L$  times  $A$  divided by  $Q$ , where  $L$  = distance between fluorometers (2.7 m),  $A$  = area of 0.088 m diameter pipe. As a result, this equation of the average velocity in the experimental pipe may help to compare the equations for predicting the travel time from the post-threshold surcharge.

**Table 6.5** Equations to predict travel time from linear function of reciprocal flow rate

Configurations	Equations	R <sup>2</sup>
0°-benched	Tbar = 0.013/Q	0.9924
0°-unbenched	Tbar = 0.019/Q	0.9955
30°-benched	Tbar = 0.0134/Q	0.9888
30°-unbenched	Tbar = 0.0193/Q	0.9013
Plug flow in pipe	Tbar = 0.0164/Q	1.0000

Note

Tbar = travel time (s)

Q = flow rate (m<sup>3</sup>/s)

It was clear that the predicted travel time from this approach was different from the ideal travel time. The travel time from the 0° and 30°-benched manhole was less than that of the plug flow in pipe. This was because the ideal travel time was calculated from the average velocity, whereas the travel time from the 0° and 30°-benched manholes was the effect of the maximum velocity distribution at the pipe centre line. On the other hand, the travel time from the 0° and 30°-unbenched manhole was greater than that of the plug flow in pipe. It may be described that there was an additional distance between the fluorometers due to the manholes.

### 6.2.2 Predictive equation using multiple regression

Besides the predictive equations developed using threshold surcharge, there is an alternative approach to predict travel time. Since travel time is a function of flow rate (Q), cross section area of pipe (A), ratio of manhole and pipe diameters (D<sub>m</sub>/D), surcharge level (S), plane angle (θ) and benching, it can be written as

$$\bar{t} = f\left(Q, A, \frac{D_m}{D}, S, \theta, \text{Benching}\right)$$

However for this study, both cross section area of pipe and ratio of manhole and pipe diameters was constant. Hence, the function could be reduced to

$$\bar{t} = f(Q, S, \theta, \text{Benching})$$

Moreover, due to a complexity of benching, such as benching and unbenching, to be numerical, the function would be separated into 2 mathematical models, i.e. one for benched manholes and another for unbenched manholes. However, these two different equations were represented by the same parameter model as

$$\bar{t} = a Q^b S^c \theta^d$$

where a, b, c and d are constant.

Subsequently, multiple regression was applied to average such values of a, b, c and d. As a result, 2 empirical equations for benched and unbenched manholes to predict travel time are shown as Equation 6.3 and 6.4, respectively.

$$\bar{t} = 9.514 Q^{-0.8981} S^{0.0642} \theta^{-1.2102} \quad (6.3)$$

$$\bar{t} = 6.230 Q^{-0.9110} S^{0.1300} \theta^{-1.1255} \quad (6.4)$$

where

$\bar{t}$  = travel time (s)

Q = flow rate (m<sup>3</sup>/s)

S = surcharge level (mm)

$\theta$  = plane angle (90°-180° for right angle to straight pipe)

Nevertheless, when these constant variables for benched and unbenched manholes were compared to one another, it was found that the figure of c, i.e. the power of surcharge parameter, from benched manholes was approximately half as much as that from unbenched manholes. This might show that surcharge was a dominant parameter, which significantly influences travel time, when the benching changes.

To evaluate errors, each of the equations was employed to generate a set of predicted data before being compared to the observed data. For benched manholes, the range of the observed travel time were 1.93 – 37.06 s, whereas the predicted travel time remained within the range of 1.75 – 29.95 s. Its maximum error was 9.34 s or 59.71 %.

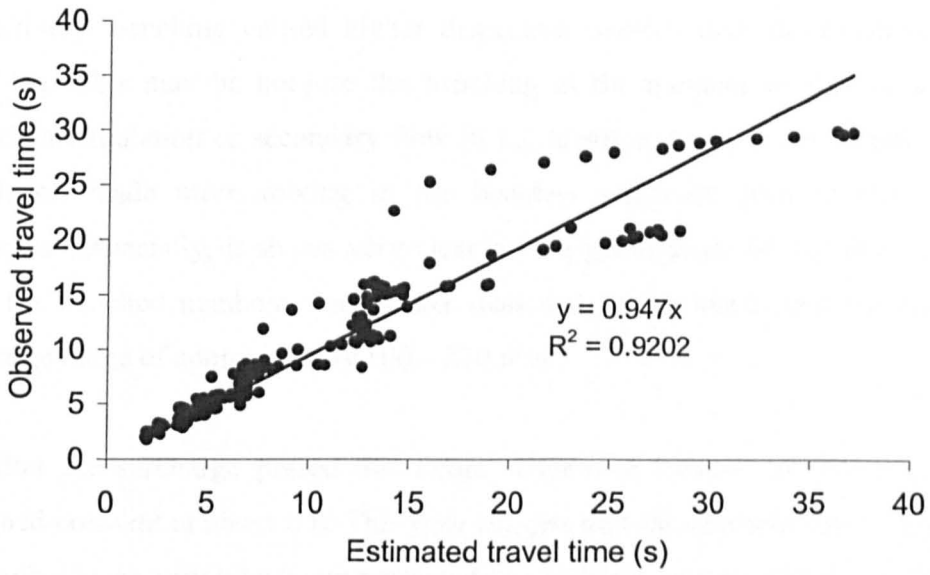
---

Similarly, for unbenched manholes, the observed travel time were between 2.47 – 62.76 s, while the travel time from the prediction were between 2.81 – 47.01 s. Also, its maximum error was 15.96 s or 57.21 %.

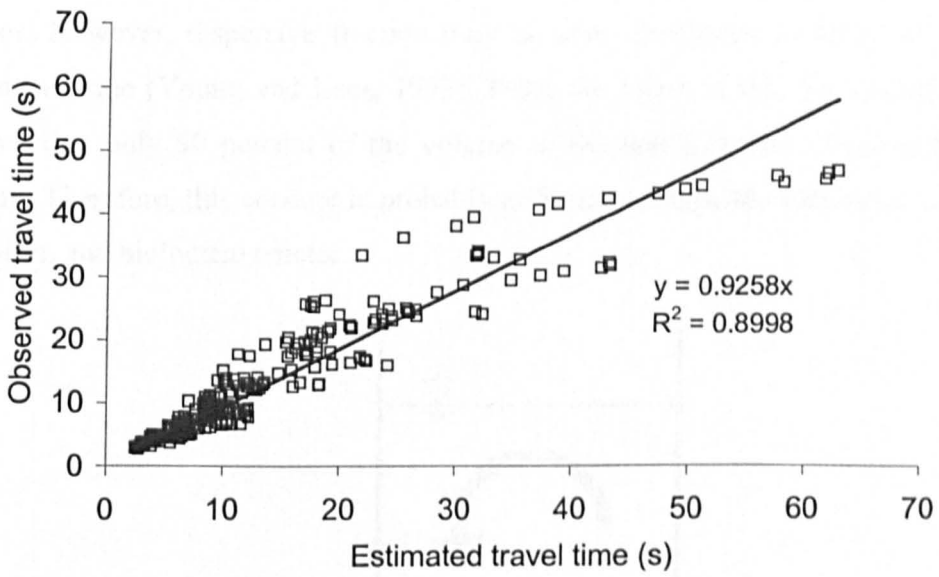
Having generalised equations for benched/unbenched manholes by means of multiple regression or dimensional analysis, the prediction of travel time could be simplified. It would be easier to be used than the equations concerned with pre- and post-surge thresholds. However, it seemed that estimated travel time from the parameters of multiple regression provided large differences from obtained travel time, especially when travel time was high as shown in Figure 6.16. Also,  $R^2$  was presented in the figure.

### 6.3 Dispersive fraction

The result of the dispersive fraction in Figure 4.13 was described with reference to the ideal reactors for mixing. It seemed that plane angle, benching and surge all affected the dispersive fraction, except flow rate. On both plane angles of  $0^\circ$  and  $30^\circ$ , benching is likely to confine jet within the manholes and make its mixing behaviour more of a plug flow reactor than a completely mixed reactor. The fraction from the benched manholes was lower than 0.5. Meanwhile, the dispersive fraction from the  $30^\circ$ -unbenched manhole was significantly greater than 0.5. Moreover, when the effect of the plane angle of  $0^\circ$  and  $30^\circ$  were compared, it showed that the dispersive fraction from the  $30^\circ$ -benched/unbenched manholes were greater than that of the  $0^\circ$ -benched/unbenched manholes.



(a) Benched manholes

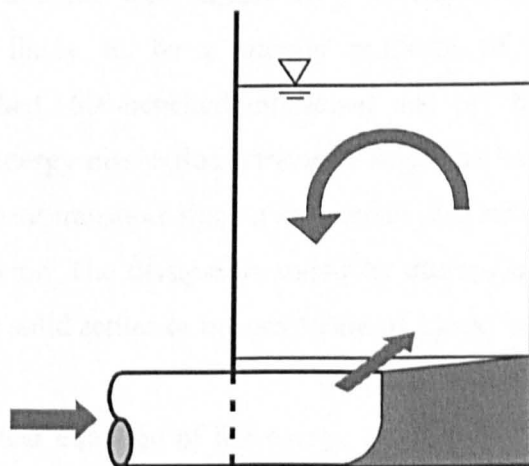


(b) Unbenched manholes

**Figure 6.16**  $R^2$  of observed travel time against estimated travel time

However, dispersive fraction from unbentched manholes was not always greater than that from bentched manholes. At some surcharge range, i.e. approximately 130 – 270 mm and 100 – 270 mm in Figure 4.13 (c) and (d) for the plane angles of  $60^\circ$  and  $90^\circ$  respectively, benching caused higher dispersive fraction than the manholes without benching. This may be because the benching at the moment worked as a baffle to provide a circulation or secondary flow in the manhole as shown in Figure 6.17. The circulation made more mixing in the bentched manholes than in the unbentched manholes. Especially, it shows very clear on the plane angle of  $90^\circ$  that the fraction from the bentched manhole was greater than that in the unbentched manhole on the surcharge range of approximately 100 – 270 mm.

But after the surcharge passed this range, dispersive fraction increased a little and remained constant at about 0.8. This may suggest that the characteristic mixing within the manhole was only 80 percent presented as a completely mixed reactor or 20 percent close to a plug flow reactor from the comparison of time dimension, i.e. residence time divided by travel time. This was the highest figure found in this experiment. In other words, it may say that a manhole can perform up to 80 percent of a completely mixed reactor. However, dispersive fraction may be also interpreted in terms of an active mixing volume (Young and Lees, 1993). From the value of 0.8, for example, it may assume that only 80 percent of the volume in the manhole was effective for solute mixing. Therefore, this concept is probably utilised to design the volume of a physical, chemical, and biological reactor.



**Figure 6.17** Provision of benching for circular flow in a manhole

## 6.4 Energy dissipation

While dispersive fraction ( $\gamma$ ) describes the relation of the mixing time and the total time for travelling along such a reactor, energy dissipation ( $G$ ) might be another parameter to present a function of the energy consumption and mixing time in the reactor since both are the products of momentum transfer. As mentioned in Chapter 2, the suitable equation of the energy dissipation for this experiment is described once again in Equation 2.56.

$$G = \sqrt{\frac{g\Delta H}{\nu T}} \quad (2.56)$$

where

$G$  = energy dissipation (1/s)

$g$  = acceleration due to gravity ( $m/s^2$ )

$\Delta H$  = head loss due to a manhole (m)

$\nu$  = kinematic viscosity of water ( $m^2/s$ )

$T$  = residence time (s).

Table 6.6 shows the average and standard deviation of energy dissipation along the observed surcharge levels at each flow rate and manhole configuration. Afterwards, the average energy dissipation is plotted against flow rate as shown in Figure 6.18. It seems that the dissipation is related linearly to the flow rate, which can be described by the linear equation and the least square ( $R^2$ ) in Table 6.7. This energy dissipation as presented was likely to be a unique property of such a manhole, e.g. 30°-benched/unbenched, 60°-benched/unbenched and 90°-benched/unbenched manholes. Therefore, this energy dissipation parameter might be beneficial to the combination of solute and sediment transport since it concerned the rate of energy distribution per unit of time in a reactor. The dissipation might be utilised in prediction of where solid is flushed or where solid settles or in conversion of a head loss to residence time.

However, the linear equation of the energy dissipation in Table 6.7 has a limit that it cannot use below 1 l/s flow rate due to the observation of the head loss term in Equation 2.56. It was collected from the experimental measurement, which was very small when



the flow rate was lower than 1 l/s and unlikely to be measured by the manometers in this experiment. This may be a reason why the linear equation does not pass the origin point. However, it represents the linear relationship of energy unit and time unit with flow rate well.

**Table 6.6** Average and standard deviation of energy dissipation along surcharge

Angles	30°unbenched		30°benched	
Q (l/s)	G (1/s)	STD	G (1/s)	STD
1	0.0463	0.0089	0.0581	0.0073
2	0.1250	0.0160	0.1669	0.0122
4	0.2929	0.0367	0.4511	0.0349
6	0.5759	0.0578	0.8009	0.0444
8	0.9169	0.0957	1.1495	0.1317
Angles	60°unbenched		60°benched	
Q (l/s)	G (1/s)	STD	G (1/s)	STD
1	0.0408	0.0057	0.0403	0.0112
2	0.1102	0.0196	0.1099	0.0194
4	0.2559	0.0307	0.2877	0.0322
6	0.4442	0.0288	0.4891	0.0283
8	0.6526	0.0259	0.7057	0.0264
Angles	90°unbenched		90°benched	
Q (l/s)	G (1/s)	STD	G (1/s)	STD
1	0.0273	0.0121	0.0288	0.0112
2	0.0904	0.0208	0.0963	0.0201
4	0.2503	0.0425	0.2521	0.0425
6	0.4089	0.0498	0.4245	0.0491
8	0.5680	0.0308	0.5887	0.0446

**Table 6.7** Linear equation and  $R^2$  for the average energy dissipation against flow rate

Manhole	Linear equation	$R^2$
30°-benched	$G = 0.1575Q - 0.1362$	0.9951
30°-unbenched	$G = 0.1231Q - 0.1258$	0.9753
60°-benched	$G = 0.0955Q - 0.0747$	0.9962
60°-unbenched	$G = 0.0871Q - 0.0649$	0.9931
90°-benched	$G = 0.0807Q - 0.0608$	0.999
90°-unbenched	$G = 0.078Q - 0.0586$	0.9994

Note      G = energy dissipation (1/s)  
               Q = flow rate (l/s)

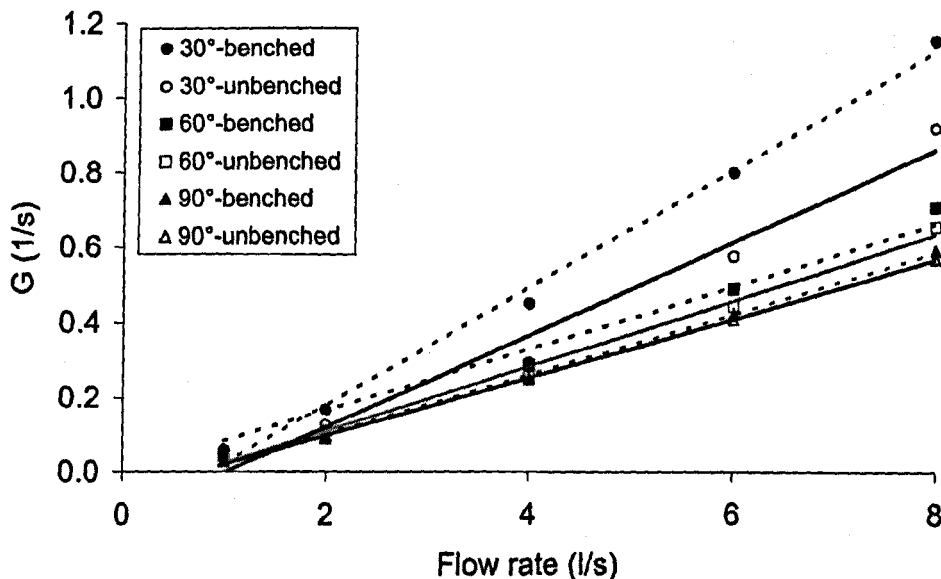


Figure 6.18 Linear relationships of average energy dissipation and flow rate

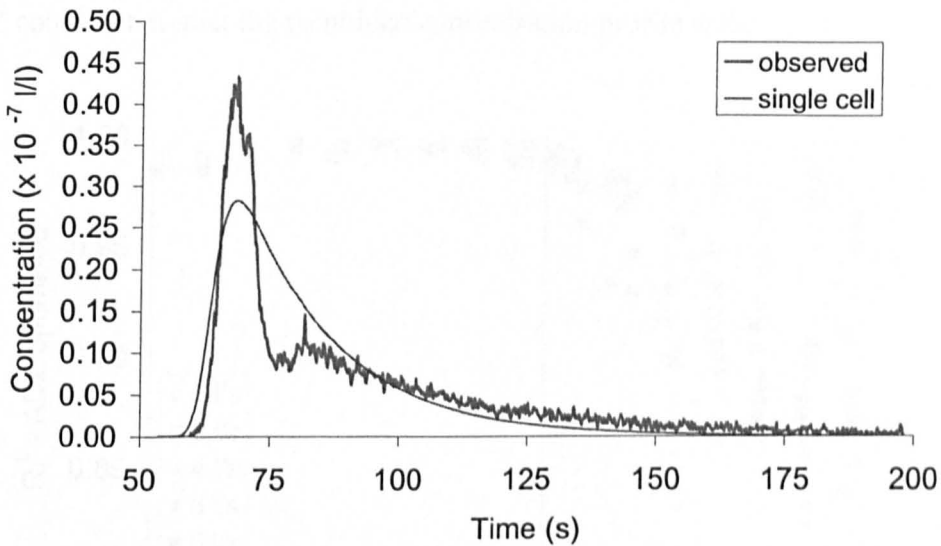
## 6.5 Cells in ADZ model

A popular technique for describing advection and dispersion in a river is a single cell ADZ model, which was presented by Beer and Young (1984) and is shown in Equation 2.43.

$$y_k = -a y_{k-1} + b u_{k-\delta} \quad (2.43)$$

where  $y_k$  = observed downstream concentration at time  $k\Delta t$ ;  $u_{k-\delta}$  = upstream concentration at time  $(k-\delta)\Delta t$ ;  $a = -e^{(-\Delta t/T)}$ ;  $b = 1 + a$ ;  $\Delta t$  = time step;  $T$  = residence time defined as travel time minus time delay ( $\bar{t} - \tau$ );  $\delta$  = nearest integer value of  $\tau/\Delta t$ ; and  $\tau$  = time delay.

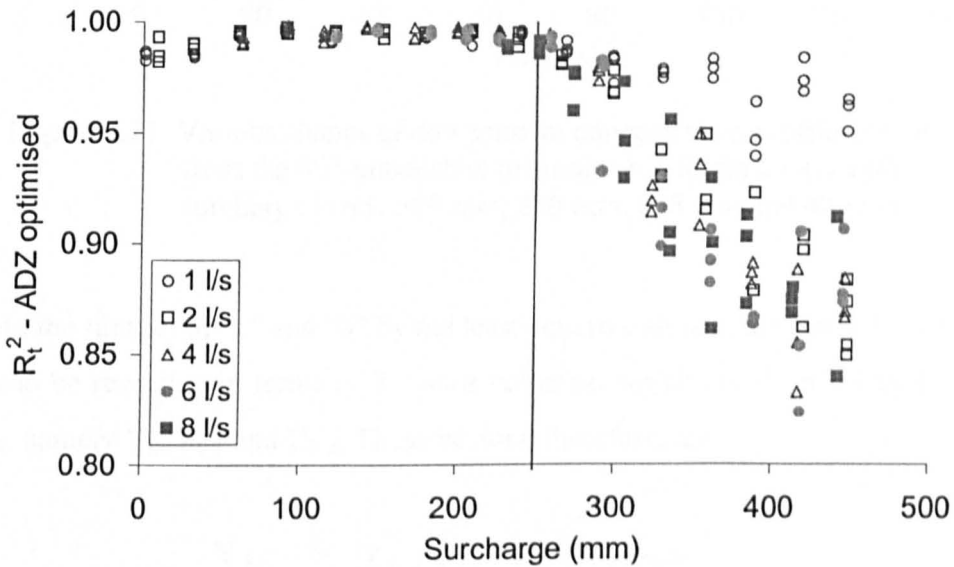
Dennis et al (1999) wrote software to evaluate the two parameters, such as time delay and travel time, in Equation 2.43 by a trial and error technique from recorded data. The prediction of the downstream concentration for step-manholes was improved and better than the standard ADZ method. However, there are some profiles that need further improvement to obtain  $R_t^2$  close to 1, the best goodness of fit, when surcharge increased.



**Figure 6.19** Prediction of downstream profile by a single cell ADZ optimised: the data from the 90°-benched manhole, 2 l/s flow rate and 425 mm surcharge

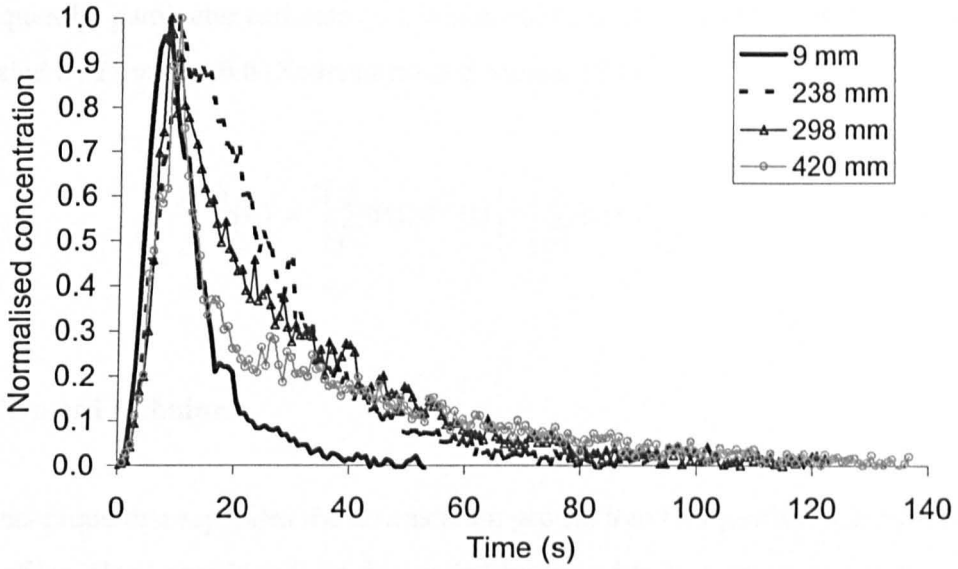
The optimised ADZ has been adopted to predict downstream profile for plane-angle-change-manholes. Like step-manholes, some of downstream profiles predicted by a single cell ADZ cannot properly fit to the observed profiles as shown in Figure 6.19. As a result, it caused a reduction in  $R_t^2$  of the prediction when surcharge increased. For example, Figure 6.20 confirmed that for the 90°-unbenched manhole, after approximately 250 mm surcharge  $R_t^2$  was declined from 1.0 at all flow rates. This was because of changes in shapes of the downstream concentration distributions when the surcharge levels increased. Figure 6.21 illustrates various shapes of the normalised concentration profiles from the 90°-unbenched manhole, at 2 l/s flow rate. It was clear that once the surcharge levels were over approximately 250 mm, the width of the peak of the concentration profile would be smaller and became similar to the width of the peak of the profile at initial surcharge, i.e. the peak's widths of 9 and 420 mm surcharge

in Figure 6.21. But the falling limbs of the profiles were different. The higher surcharge seemed to have a longer, larger falling tail than that of the initial surcharge. This greater tail may be caused by dispersion process in the manhole chamber, which worked as a dead zone to hold and leave just a little of the tracer dye at each time. Hence, at these surcharge levels, it seemed that the downstream concentration profile was an almost equal combination of advection and dispersion processes, which were represented by the narrow peak and long tail of the profile, respectively. Consequently, a single cell ADZ could not predict the combined concentration profile well.



**Figure 6.20** Relationship between surcharge and  $R_t^2$  using an optimised single cell ADZ for the 90°-unbenched manhole

To improve the prediction of the temporal downstream concentration profiles, two identical first-order models were developed. The downstream profile was divided into 2 profiles: Head and Tail profiles by using parameters estimate. The Head profile was generated to obtain both “a” and “b” parameters in Equation 2.43 by the least-squares estimate from the observed upstream and downstream data. Then, an assumed tail profile could be generated from the observed downstream profile minus the head profile. When the assumed tail profile was obtained, “a” and “b” parameters were estimated by the same optimisation method as Dennis et al (1999). In other words, the first set of “a” and “b” parameters were directly estimated from Equation 2.43 by regression of a matrix, while the second set of “a” and “b” were obtained by the optimised ADZ.



**Figure 6.21** Various shapes of downstream concentration profiles obtained from the 90°-unbenched manhole, at 2 l/s flow rate, with surcharge levels of 9 mm, 238 mm, 298 mm and 420 mm

To gain the first set of “a” and “b” by the least-square estimate, the raw data in Equation 2.43 can be rewritten in terms of 3 vector columns, which are signified by the capital letters, namely  $Y_k$ ,  $Y_{k-1}$  and  $U_{k-\delta}$ . These vectors, therefore, are

$$\begin{aligned}
 Y_k &= [y_k, y_{k+1}, y_{k+2}, \dots, y_{k+n-1}]^T \\
 Y_{k-1} &= [y_{k-1}, y_k, y_{k+1}, \dots, y_{k+n}]^T \\
 U_{k-\delta} &= [u_{k-\delta}, u_{k-\delta+1}, u_{k-\delta+2}, \dots, u_{k-\delta+n-1}]^T
 \end{aligned}$$

and

$$\Phi^T(t) = [-Y_{k-1} \ U_{k-\delta}]$$

Also, “a” and “b” parameters can be represented by  $\theta$ , which is

$$\theta = [a \ b]^T$$

Then, Equation 2.43 has a new form in matrix as Equation 6.5.

$$Y(t) = \Phi^T(t) \theta + v(t) \tag{6.5}$$

where  $v(t)$  = stochastic disturbance and will converge to zero by least-squares estimate.

Consequently, parameter estimate ( $\hat{\theta}$ ), which consists of “a” and “b” parameters, can be calculated by Equation 6.6 (Soderstorm and Stoica, 1989).

$$\hat{\theta}(n) = \left[ \sum_{t=1}^n \Phi(t) \Phi^T(t) \right]^{-1} \left[ \sum_{t=1}^n \Phi(t) Y_k \right] \quad (6.6)$$

### 6.5.1 Two-cell technique

It is a technique that separates the downstream profile into two profiles named Head and Tail profiles. Head profile will be dominated by the advective process as it comes first and contains the peak of the downstream profile. Meanwhile, Tail profile is the remaining part of the whole downstream profile, in which dispersion might be a major process. In other words, this two cell technique was to quantify the amounts of solute concentration travelling in core zone, dominated by advection process, and diffusion zone, dominated by dispersion process, in jet flow which were represented as Head and Tail profiles, respectively.

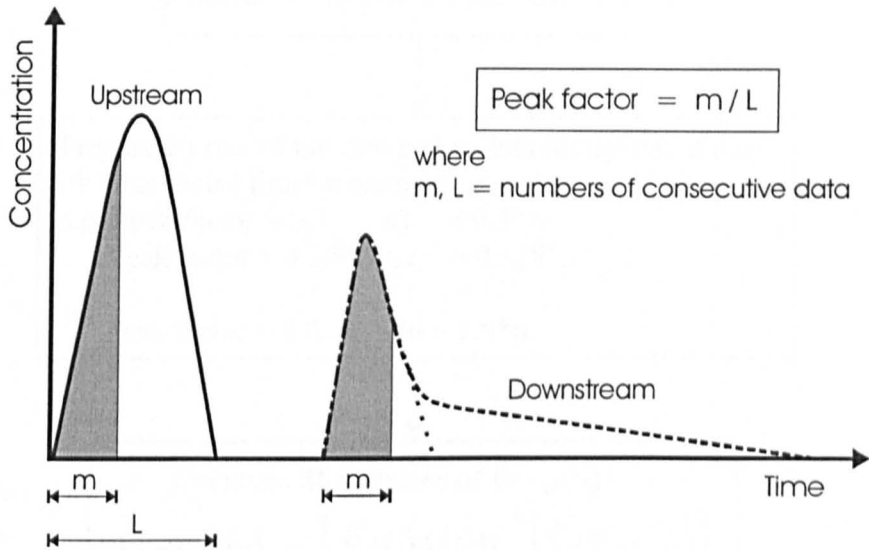
#### *Head profile*

Even though Equation 6.6 can determine the parameter of “a” and “b”, both values are not constant and depend on the range of the upstream and downstream data used for the comparison. To obtain the best of parameter estimates, the 26 elements of an array called “Peak factor” are employed. The figure of 26 was obtained from testing all the investigated data set and found that this number would help the computer to run very fast and consume suitable memories. Meanwhile, Peak factor, as shown in Figure 6.22, was set in order to find how many upstream and downstream data in a row should be compared until the parameters of “a” and “b” could be obtained.

Figure 6.23 shows the flowchart of generating Head profile. It starts from obtaining both upstream and downstream data. Then, the vectors of  $Y_k$ ,  $Y_{k-1}$  and  $U_{k-s}$  were prepared. Peak factor consisted of the value from 0.3 to 1.0, in which there were 25 equal steps increasing. For example, if Peak factor was 0.328 and the upstream data had

100 consecutive points. That means parameter estimate in Equation 6.6 would be calculated from 32 consecutive points of both upstream and downstream data.

The figure started at 0.3 was more suitable than 0.0 because from observation the Peak factor always began after 0.3. Thus, it would be effectively used computer memories to retain only a large number of constructive data generated later.



**Figure 6.22** Peak factor to obtain the best parameters of “a” and “b” for Head profile’s prediction

Until this moment, 26 parameter estimates were created from each Peak factor and ready to generate 26 possible Head profiles with Equation 2.43. Afterwards, each of these profiles was compared to the downstream data from the first point until a few points after the peak. The results of this comparison were presented in terms of  $R_t^2$ . Therefore, the best  $R_t^2$ , close to 1.0, would be selected and its parameter estimate was adopted.

However, the gain value ( $G_H = b/(1+a)$ ) should be also considered. Its value might be between 0.0 and 0.75 (or 0 to 75 % of the area under the downstream profile) so that more than 0.25 remaining should be the area ratio of Tail profile and the whole downstream profile. Figure 6.24 was an example of 26 values of Peak factor and  $R_t^2$ . It shows that the suitable Peak factor was 0.804 and  $R_t^2$  is 0.9962, which was slightly higher than its nearby points.

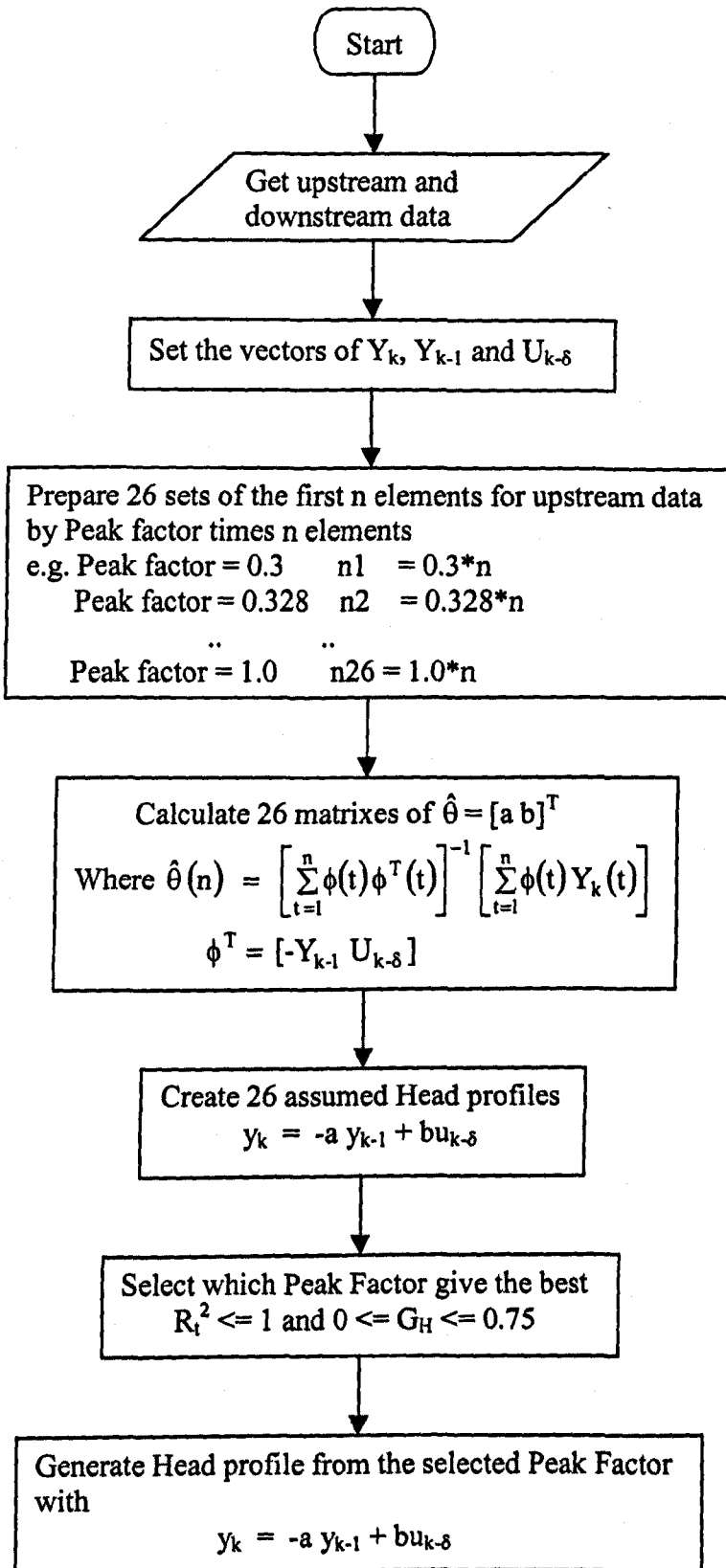


Figure 6.23 Flowchart of generating Head profile



---

***Tail profile***

By the downstream profile minus Head profile, the assumed tail profile was obtained. Then, there was a possibility of using the optimised ADZ (Dennis et al, 1999) to analyse this tail profile as it did not need the exact starting-point of the tail profile for the trial and error technique. The algorithm of generating Tail profile was also described and shown by the flowchart in Figure 6.25. The diagram started with the assumed tail profile obtained. Next, an array of 11x11 elements for time delay and residence time parameters was set. Their values were initialised by a proper range of time (e.g. they should cover the time between the starting point of the upstream profile and the last point of the downstream profile). Then, each couple of these parameter was replaced into Equation 2.43 and 121 profiles were calculated. But "b" was at the moment equal to the gain multiplied by the result of "1 + a" or written as "b" equalled  $(1-G_H)(1+a)$  where  $1-G_H = G_T$ , the gain at Tail profile. After that, each of 121 profiles were compared to the downstream profile by  $R_t^2$  equation. Their  $R_t^2$  were collected and which  $R_t^2$  was closest to 1.0 was selected. This would be the best product of the marked time delay and residence time. At this step, if the resolutions of time delay and residence time was better than 0.01 s and 0.001 s respectively, the array would be contained with the new shorter range of time than the initiation. If not, next loop from setting the array's values to the decision of the resolution began again until their resolution were achieved. Finally, the best of the parameters were employed to predict "Tail profile".

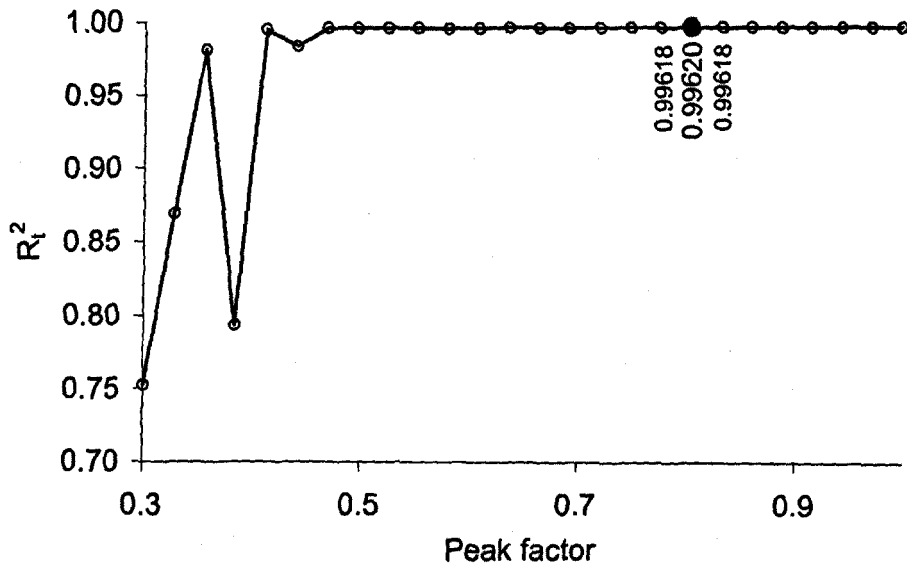


Figure 6.24 The best Peak factor obtaining the greatest  $R_t^2$  for Head profile

### *Two cells*

After both Head and Tail profiles were predicted, the whole downstream profile was estimated by addition of these two profiles. Figure 6.26 shows the predicted downstream profile by this method, which analysed the data from the 90°-benched manhole at flow rate 2 l/s and 425 mm surcharge. At Head profile, the gain was 0.487, time delay was 5.6 s and residence time was 2.1 s, and its data distribution was almost symmetrical. But at Tail profile, the distribution lacked symmetry and the values of time delay and residence time were also different from that of Head profile, i.e. 17.0 s and 29.0 s, respectively.

Besides, this estimated downstream profile was compared to the estimated profile from the single cell ADZ and shown in Figure 6.27. In this case,  $R_t^2$  obtained from the two cell ADZ was better than that of the single cell ADZ, i.e. 0.992 and 0.854, respectively.

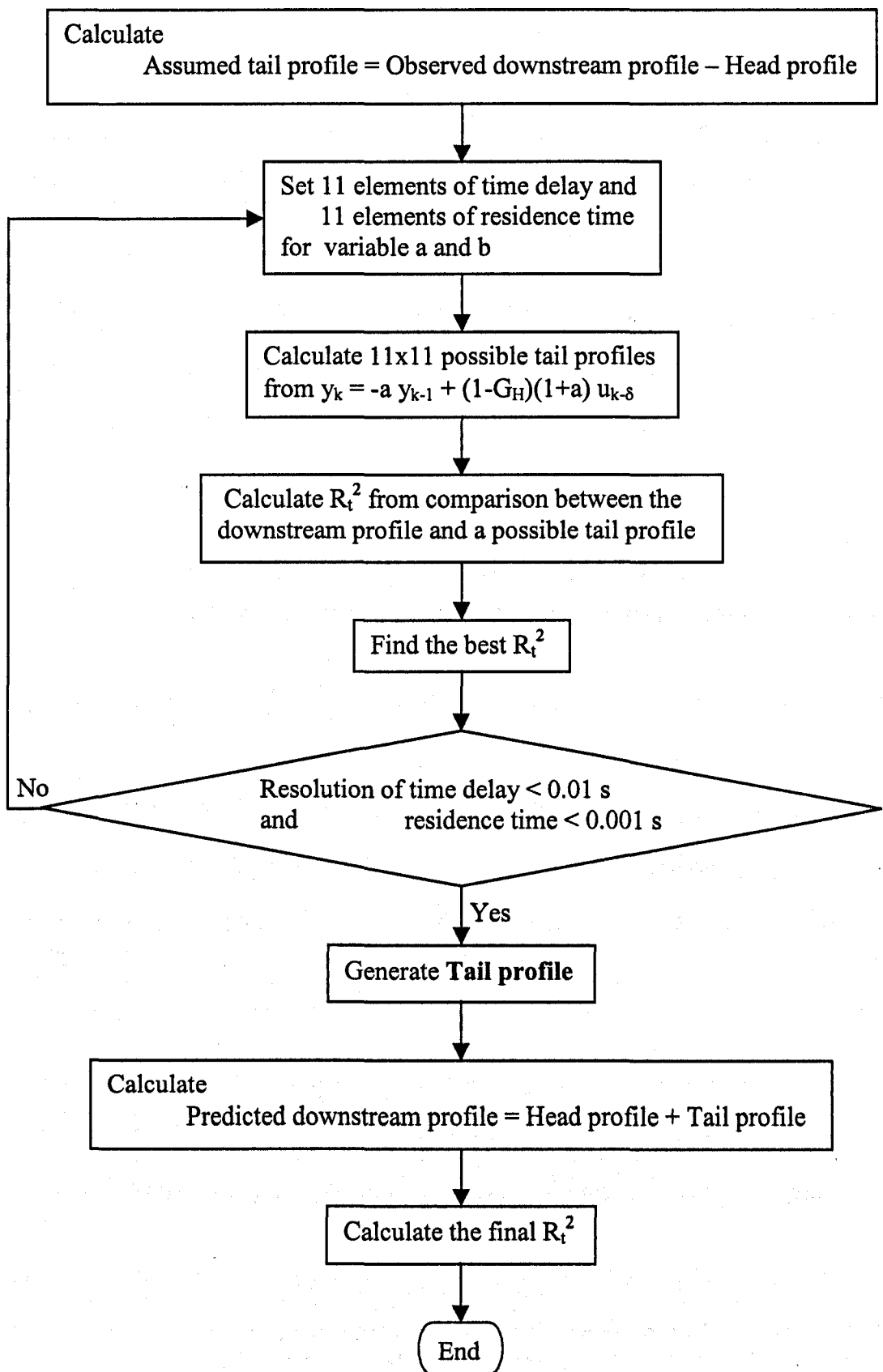
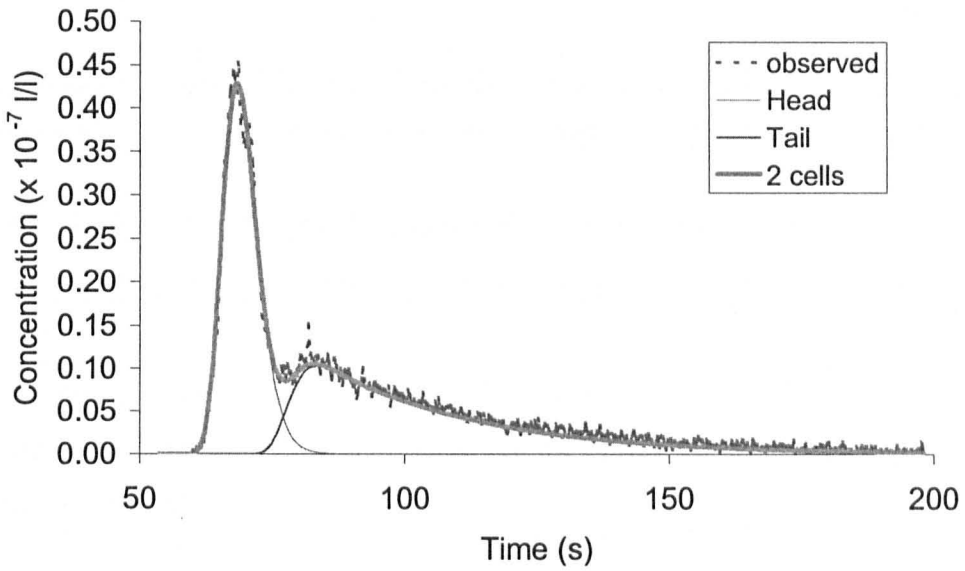
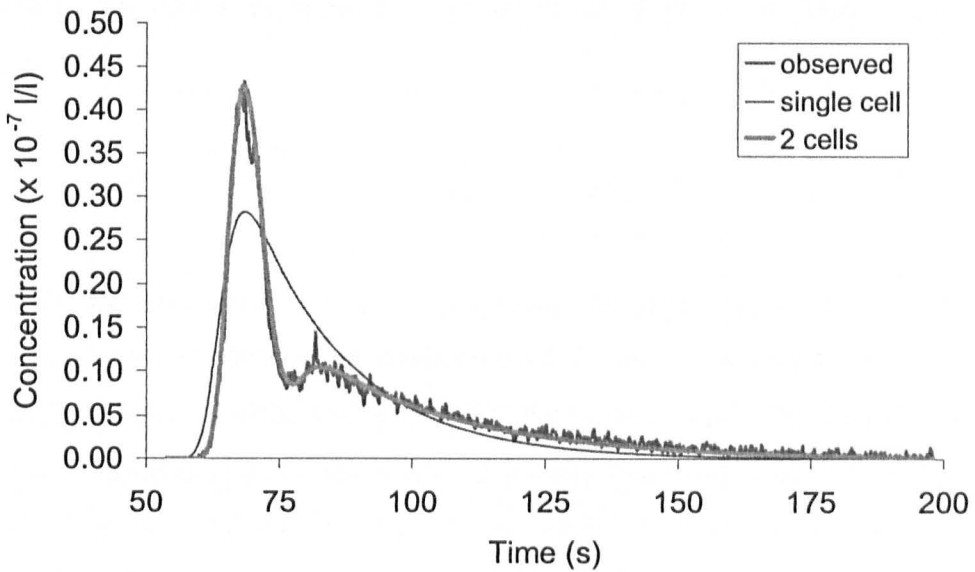


Figure 6.25 Flowchart of generating Tail profile



**Figure 6.26** Comparison of observed downstream profile and the profile of 2 cells obtained from Head profile plus Tail profile



**Figure 6.27** Comparison of prediction from 2 cells and single cell with observed downstream profile; consequently, two-cell technique was better for prediction.

**Table 6.8** Increase in  $R_t^2$  by two cell ADZ

Model	0°	30°		60°		90°	
	Benched	Benched	Unbenched	Benched	Unbenched	Benched	Unbenched
Single cell ADZ	0.9819	0.8138	0.8750	0.8050	0.7840	0.8260	0.8538
Two cell ADZ	0.9871	0.9656	0.9867	0.9855	0.9719	0.9626	0.9821

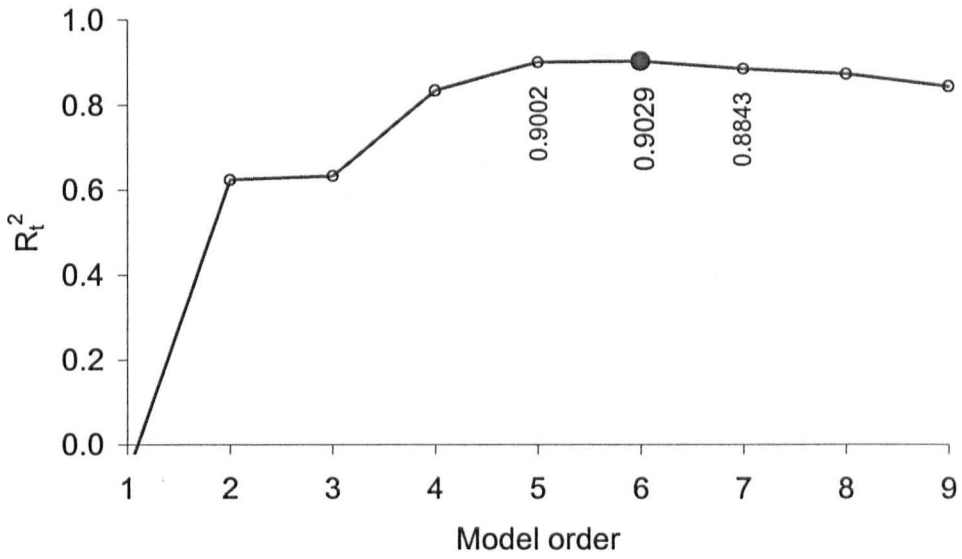
Moreover, Table 6.8 confirms the improved  $R_t^2$  when using the two cell ADZ. The minimum  $R_t^2$  analysed by the single cell ADZ for the whole manhole configurations in this study is shown and compared to the  $R_t^2$  obtained from the two cell ADZ for the same conditions. It seemed that at the 0°-benched manhole,  $R_t^2$  slightly increased since the single cell had predicted well, whereas for the others,  $R_t^2$  increased significantly by using the two cell ADZ.

### 6.5.2 Cells in series technique

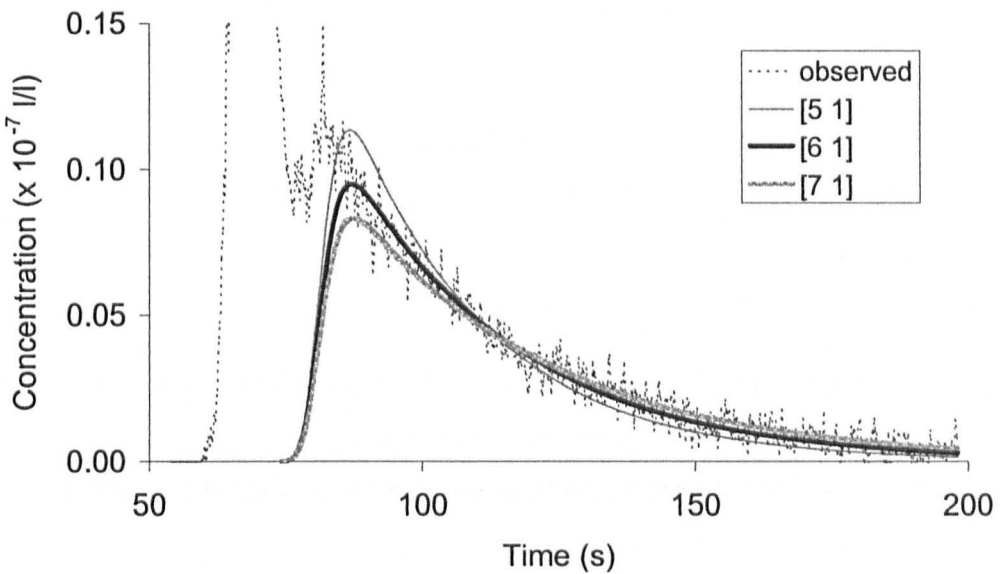
In addition to the optimised Tail profile, it may be predicted by another method. It is the serial connection of several ADZ cells. The n-serial ADZ cells in a row is adopted since it might predict the best Tail profile. The prediction by Equation 2.43 for a single cell is expanded and becomes Equation 6.7 for the series of the n single cells (Young and Lees, 1993).

$$y_k = -a_1 y_{k-1} - a_2 y_{k-2} - a_3 y_{k-3} \dots - a_n y_{k-n} + b_{u-\delta} \quad (6.7)$$

Afterwards, the simplified refined instrumental variable (SRIV) procedure (Young, 1984) was applied to achieve an evaluation of  $a_1$ ,  $a_2$ , ...,  $a_n$  and  $b$ . It is the n-order differential equation which was written in terms of z-transform (Young and Lees, 1993). For this investigation, the model order had been tested up to 9, i.e.  $n = 9$ , to obtain the best  $R_t^2$ , and the consequence of the  $R_t^2$  is shown in Figure 6.28, which indicated that the model order of 6 would provide the best prediction. Also, the comparison between the profiles predicted from model of 5, 6 and 7 is illustrated in Figure 6.29. It was clear that the 6<sup>th</sup> order predicted the Tail profile well. Moreover, when the 6<sup>th</sup> order was used with the other data sets, it was always the best model to present the Tail profiles. Therefore, Equation 6.7 could be summarised and written as the sixth-order block diagram and six single cells equivalent in Figure 6.30.



**Figure 6.28** The 6<sup>th</sup> order provided the best  $R_t^2$  for the Tail profile; data from the 90°-benched manhole at 2 l/s flow rate and 425 mm surcharge



**Figure 6.29** The best model order, [6 1], for the prediction of the Tail profile, compared to the 5<sup>th</sup> and 7<sup>th</sup> order; data from the 90°-benched manhole at 2 l/s flow rate and 425 mm surcharge

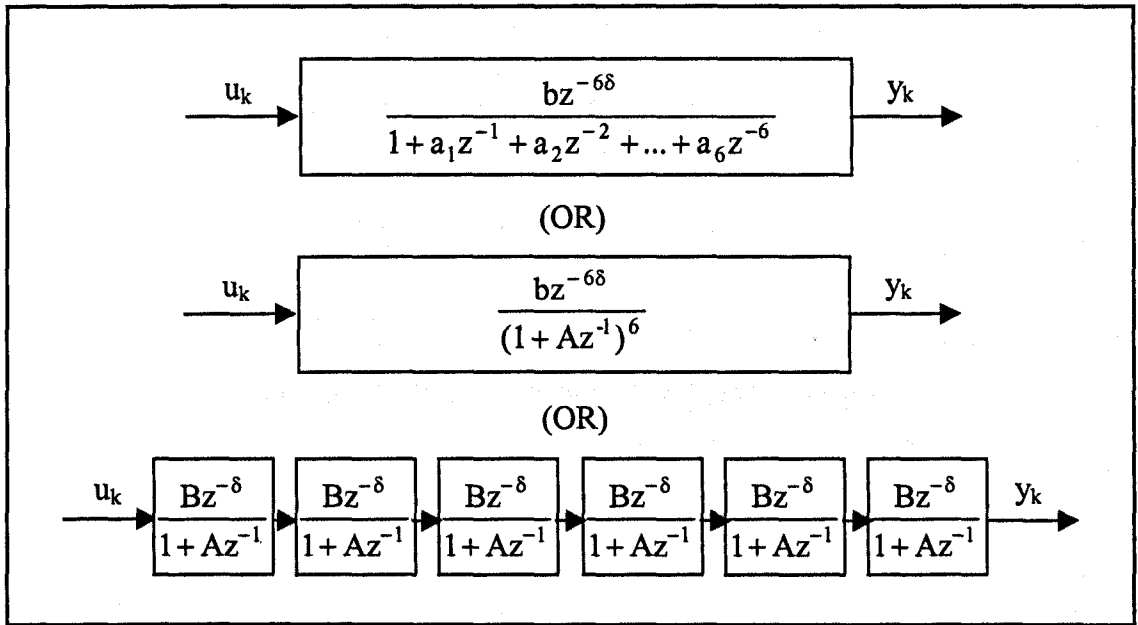


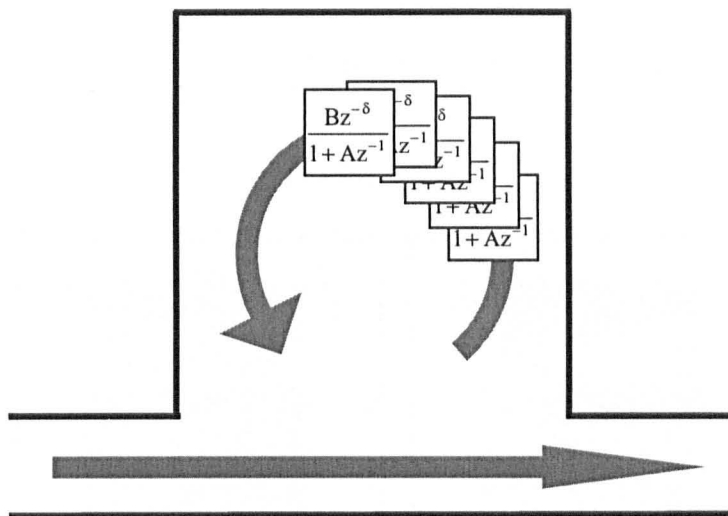
Figure 6.30 Series of sixth-order block diagram

After “A” in Figure 6.30 was precisely obtained, residence time (T) could be calculated from Equation 6.8 (Lees et al, 2000). But, this was only the residence time for a single cell; therefore, residence time (Tr) for the whole serial connection of 6 cells was 6 times T as shown in Equation 6.9.

$$T = -\Delta t / \ln (-A) \tag{6.8}$$

$$Tr = 6 * T \tag{6.9}$$

Moreover, the serial connection may be interpreted in terms of physical property. From the experiment on surcharged manholes, several times of tracer dye re-circulation were found. This might mean that each round of the re-circulation was related to a small single cell in the serial connection as shown in Figure 6.31. Furthermore, on a video of tracer dye movement in a manhole, it suggested that there are several repetitions of dye circulation occurring as presented in Figure 6.32.



**Figure 6.31** Re-circulation of tracer dye in a manhole

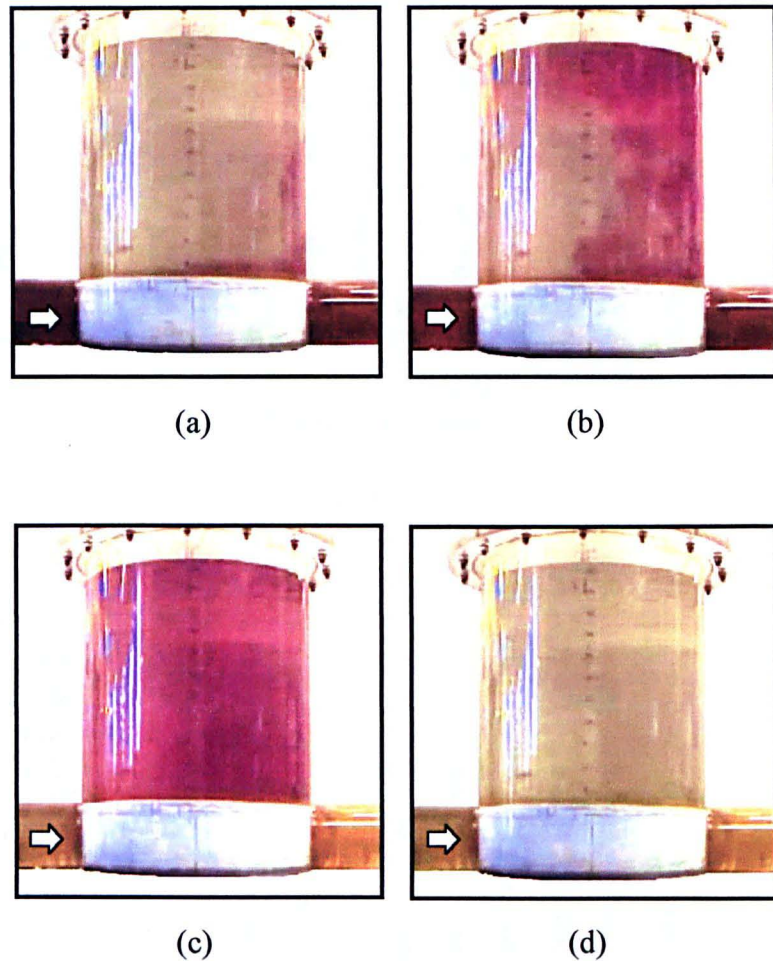
### 6.5.3 Results from analysis

Results analysed by the technique of 2 cells of the 90°-benched/unbenched manholes are presented in Figure 6.33 and 6.34. They illustrate the residence time of Head and Tail profiles, which were determined by means of the trial and error in the optimised ADZ technique.

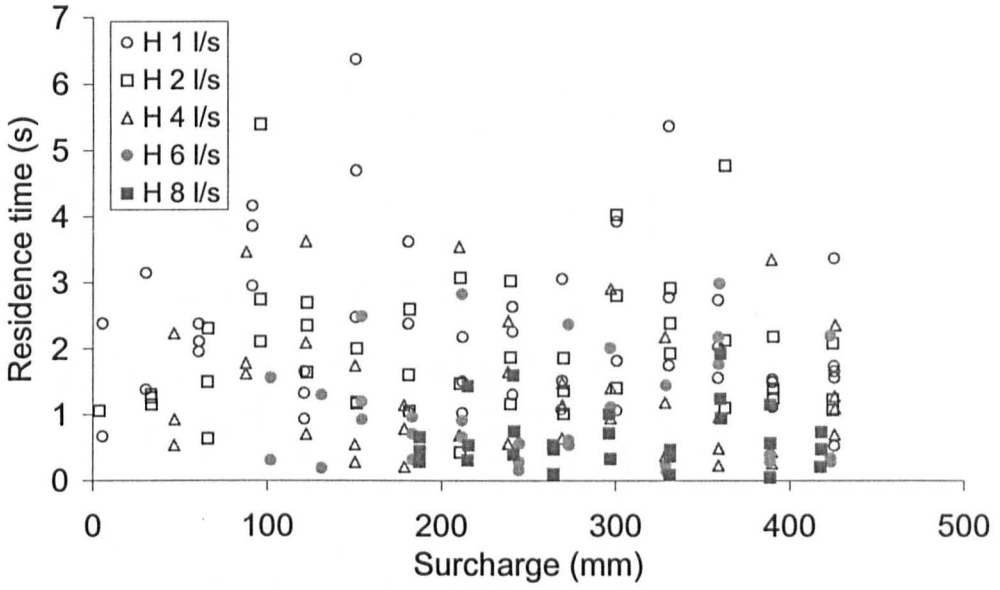
The Head profiles in Figure 6.33 (a) and 6.34 (a) had scattered residence time. It varied up to approximately 7 s and 16 s for the 90°-benched/unbenched manholes at the flow rate of 1 l/s, respectively. It seemed that the benching can reduce the variation of the residence time from 16 s to 7s on the Head profile due to its confinement.

Unlike the pattern of the residence time on the Head profiles, the Tail profiles provided residence time more related to surcharge as shown in Figure 6.33 (b) and 6.34 (b). Its relationship was similar to the residence time calculated by a single cell as shown in Chapter 4, but slightly more. For example, the average residence time of the 90°-unbenched manhole at 1 l/s flow rate was highest at 52.6 s analysed by the single cell technique, while that increased to 55.0 s, by the 2-cell technique, on the Tail profile. This might be caused by that the tail section in observed downstream distribution was more concerned by Tail profile in 2-cell technique, whereas the single cell technique averaged the residence time from the whole downstream profile.

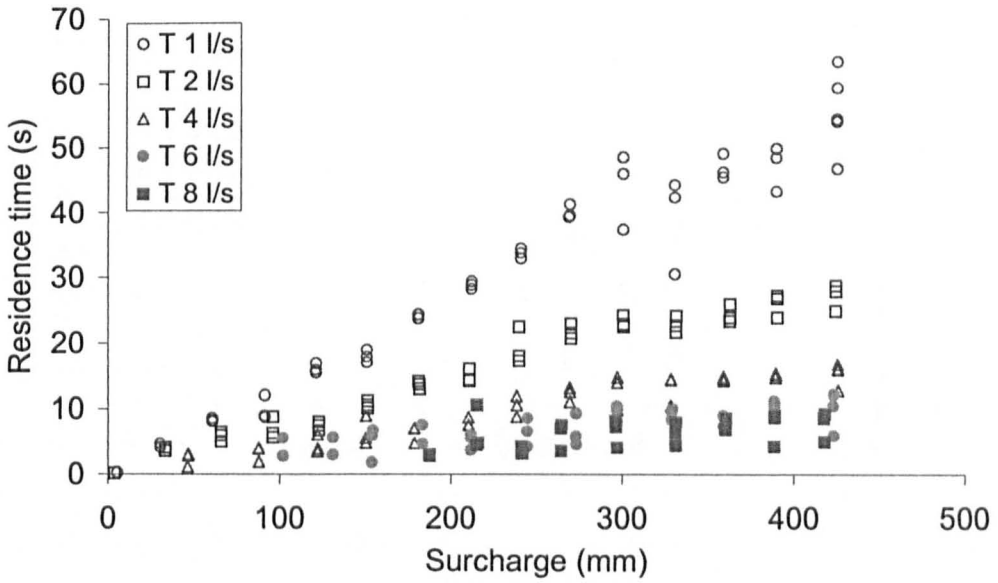




**Figure 6.32** Tracer dye distribution, represented by red, through the 388 mm diameter manhole connected with the 88 mm diameter pipe: (a) the first part of the dye travelled through the manhole along the pipe and the second part started circulating in the manhole; (b) more circulation of the dye in the manhole, while the other still flows through the pipe; (c) re-circulation of the dye for several times in the manhole, whereas the first part all has passed the pipe; and (d) both parts of the tracer dye have passed the manhole and pipe

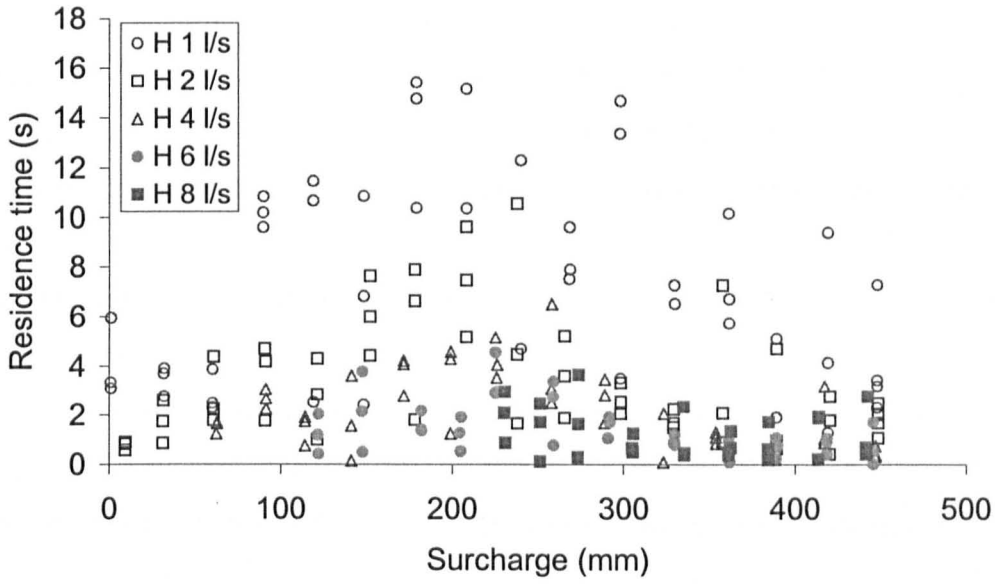


(a)

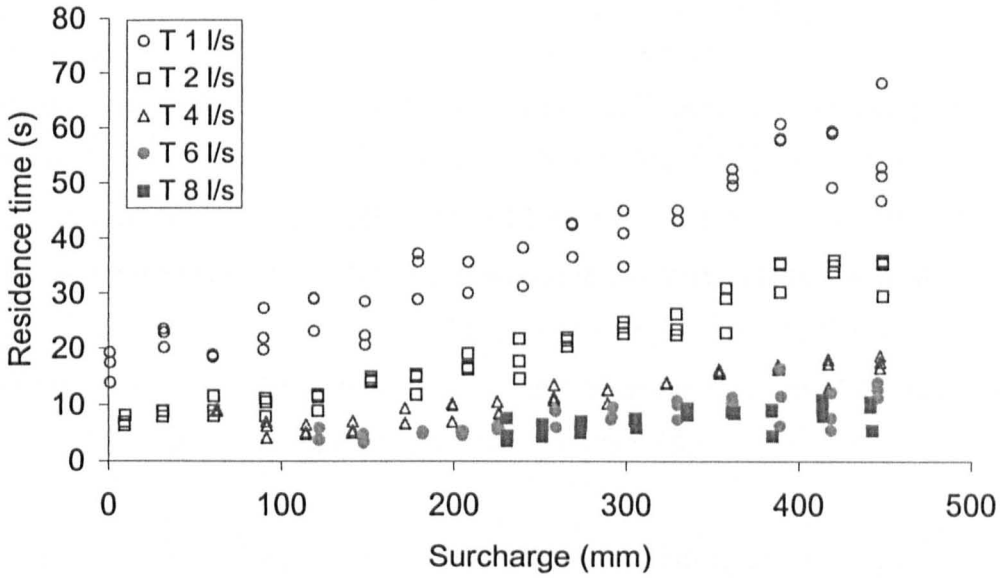


(b)

**Figure 6.33** Residence time from 2-cell technique of the 90°-benched manhole: (a) Residence time from Head profile, (b) Residence time from Tail profile



(a)



(b)

**Figure 6.34** Residence time from 2-cell technique of the 90°-unbenched manhole: (a) Residence time from Head profile, (b) Residence time from Tail profile

#### 6.5.4 Conclusions for two-cell ADZ technique

Some downstream data distributions, which were represented by almost equal combination of advection and dispersion mechanisms and the width of the peak became shrunk, cannot be properly estimated by a single cell ADZ model. Two cells analysis of the first-order model is one of solutions to predict the profile. Therefore, the downstream profile is separated into 2 profiles, namely, Head and Tail profiles. Each profile is dominated by advection and dispersion, respectively.

Head profile is generated by the two parameters, "a" and "b", obtained from the best Peak factor. They are calculated by least-square estimate from the relationship between a suitable range of upstream and downstream data. The proper Head profile should have the same peak as the downstream profile observed from the experiment so that the rest, i.e. the whole downstream profile minus the Head profile, will be easily estimated by the method for Tail profile.

When Head profile has been predicted and subtracted from the downstream profile, the assumed tail profile is obtained. To predict Tail profile, 2 optional methods are presented. The first is the ADZ optimised from a single cell, whereas the other applies the concept of several small cells connected in series. In this case, a Tail profile that was predicted by the sixth-order was well matched to the observed downstream profile when it was compared to the fifth-order and seventh-order. That seemed to be a series of small cells taking place in the manhole. Also, this phenomenon might be supported when many cycles of tracer dye were observed in the manhole.

To predict solute profiles, several small connecting cells might be a constructive model. When the downstream profile has the long, large falling limb, the single cell only does not predict the downstream profile well. Therefore, a solution should be the two first-order cells, each of which is dominated by advection and dispersion processes represented by, for example, Head and Tail profiles, respectively. However, it is much more complicated than the single cell.

---

## Chapter 7

# Future work

Having investigated solute substances mixing in a manhole, prominent mechanisms: advection and dispersion are comprehended to predict their travelling. Because the magnitudes of these two parameters corroborating together are dependent on each physical aspect of a manhole, further studies on dispersion across a manhole should be examined with other manhole configurations. Also, the data should be taken to generate and evaluate predictive equations, including the results from CFD software.

### 7.1 Multiple inlets

As Lindvall (1984) studied the head loss coefficient due to a straight pipe manhole with a 90° lateral pipe in laboratory (more detail in Chapter 2), longitudinal tracer study might be also investigated with this manhole configuration. The results from the comprehensive data help to describe the correlation between head losses and solute dispersion as well as to predict the solute dispersion across such a manhole. Moreover, its consequences will be beneficial to develop a general predictive equation for solute concentration profiles. The basis of this investigation is that every aspect of a manhole, in which the head loss coefficient was quantified, can also be tested with the tracer study in order to obtain the solute dispersion value and its relevance to the head loss.

### 7.2 Universal equation for dispersion across manholes

It will be worthwhile if all results from several different changes in manhole aspects, such as shape, diameter, elevation and direction of pipe centrelines, benching and surcharge levels, are integrated. Then, multiple regressions analyses may be used to

---

obtain a universal predictive equation for solute transport across manholes. Afterwards, the equation can be validated with the experimental data, together with its maximum error which should be presented to inform confidential levels of the equation. After that, the equation may be also contributed to an environmental software to simulate an effect of solute pollutants on receiving waters along a sewer system, including manholes.

### **7.3 Unsteady flow condition**

Since Howarth and Saul (1984) investigated the impact of time varying flow rates on the head loss coefficient of manhole and found that the coefficient may be overestimated with the steady state condition, this concept will be adopted to quantify the dispersion of pollutants in real situation of a sewer system. Studying time varying flow conditions, an actual value of solute dispersion may also be obtained. Then, its results will probably improve the ability of urban drainage software to predict pollution concentrations and to help prevent the concentration over the limited values of local environmental regulations.

### **7.4 Field velocity**

To validate the velocity in a manhole simulated by CFD, the field velocity should be measured. The ADV (Sontek, 1995) will be applied to obtain 3 dimensional velocity at a point, in which the velocity may highlight the swirling motion, in the manhole. Then, the field velocity will be compared to calibrate the calculated velocity from CFD software. This comparison might also help to better understand mixing mechanisms taking place within a manhole.

---

## Chapter 8

# Conclusions

The study of the effect of changes in pipe directions across surcharged manholes was mainly concerned with energy losses and the transport of a soluble substance within a sewer system. The energy losses were described in terms of the head loss coefficient ( $K$ ) times the velocity head ( $V^2/2g$ ). The solute transport was modelled by the aggregated dead zone (ADZ) equation in order to obtain crucial parameters, such as travel time ( $\bar{t}$ ) and dispersive fraction ( $\gamma$ ). In addition, models to predict the downstream concentration profile were also developed by means of a serial and/or parallel connection of a single cell ADZ, which was separately presented from the head loss coefficient.

The head loss coefficient for this study varied with both floor type and plane angle of the manholes. Benching at the bottom of the manhole can confine the jet flow and cause a reduction of the loss coefficient. From the results, it was clear that the head loss coefficient dramatically increased, when the plane angle changed from  $0^\circ$  to  $30^\circ$ .

Travel time was dependent on all investigated parameters, such as floor type, plane angle, flow rate and surcharge. Travel time from a few manholes was not related on surcharge or it did only on the lower range of surcharge levels. There were 2 techniques to generate predictive equations for travel time: using a surcharge threshold and multiple regression. A surcharge threshold level was introduced to divide the correlation of travel time and surcharge into 2 main sections, namely pre- and post-threshold. On the range of the pre-threshold surcharge, travel time had a linear relationship with surcharge, whereas on the post-threshold surcharge the travel time was independent of surcharge. Moreover, from the experiment, it also showed that travel time had a linear relationship with reciprocal flow rate. For the equations using the multiple regression, it

---

showed that when the manholes were benched, the effect of surcharge on travel time reduced.

From the discussion section, it seems that residence time, which equals travel time minus reach time delay, can be determined directly from the head losses as presented in terms of G-value. This may need more confirmation from other data sources until it is proven that its relationship is always predictable at the other manhole configurations. In other words, it still needs more investigations.

Dispersive fraction obtained from ADZ model was used to determine an amount of mixing in the manholes and presented in terms of partial mixing. Dispersive fraction is relative to the ideal dispersive fraction of 2 ideal mixing reactors, "plug flow" and completely mixed reactors. For the study, the dispersive fraction is highest at approximately 0.8, which means that the solute mixing in the manhole is almost complete or 80 percent of complete mixing.

Although the parameters obtained from a single cell ADZ model can be calibrated and predict the downstream profile well, there is a limit to the prediction when the profile has a high variance value at high surcharge levels. Two-cell technique of ADZ model can be used to improve the ability of the prediction. It is a connection of 2 single cells of ADZ by a series and/or parallel.

However, a single cell ADZ still seems to be more suitable than two cell technique in terms of conceptual predictive modelling due to the simplicity. The single cell technique provides a simpler calculation, whereas the two cell technique is very complicated. Even though two cell technique can increase the goodness of fit ( $R_i^2$ ) of solute downstream concentration profile, it did not present much difference in terms of residence time in this study. For example, at the flow rate of 1 l/s and 450 mm surcharge from the 90°-unbenched manhole, which provides the maximum residence time in this whole study, the average residence time was 52.6 s, while the average figure accounted for 55.0 s at Tail profile from the two cell technique in Figure 6.34 (b). This maximum difference is only 4.6 %. This is also confirmed by Rutherford (1994) that a single cell ADZ can satisfactorily model the complexities of a natural channel.



---

Finally, this study was able to quantify the magnitudes of tracer parameters and head loss coefficient due to changes in pipe direction across surcharged manholes well. Moreover, a linear correlation of the energy dissipation with flow rate for each manhole configuration was also found. It might contribute to mixing society for a conversion of a head loss to residence time. The next contribution to basic knowledge of tracer study was that the two cell technique. Even though it was very complicated to be used, it predicted the downstream profile very well, especially in terms of the peak value, the peak location and the tail distribution of the concentration profile.

---

# References

**Arao, S. and Kusuda, T. (1999)** "Effects of pipe bending angle on energy losses at two-way circular drop manholes." 8<sup>th</sup> International conference on urban drainage, Australia, Sydney, 2163-2186.

**Archer, B., Bettess, F. and Colyer, P.J. (1978)** "Head losses and air entrainment at surcharged manholes." Wallingford, UK.

**Asztely, M. and Lyngfelt, S. (1996)** "Three-dimensional modelling of energy losses in a manhole." 7<sup>th</sup> International conference on urban drainage, Hanover, Germany, 647-652.

**Balmforth, D.J., Saul, A.J. and Clifforde, I.T. (1994)** "Guide to the design of combined sewer overflow structures." Foundation for Water and Research, Report No FR0488.

**Beer, T. and Young, P.C. (1984)** "Longitudinal dispersion in natural stream." Proc. A.S.C.E., J. of Env. Eng. Div., 109, 1049-1067.

**Boxall, J.B., Shepherd, W., Guymer, I. and Fox, K. (2003)** "Changes in water quality parameters due to in-sewer processes." Water Science and Technology, Vol. 47, Part 7/8, 343-350.

**Brombach, H. (2002)** "Urban storm water practice in Germany." 9<sup>th</sup> International conference on urban drainage, Portland, Oregon, USA.

---

**Chadwick, A. and Morfett, J. (1995)** "Hydraulics in Civil and Environmental Engineering" E & FN Spon, an imprint of Chapman & Hall, 2-6 Boundary Row, London, SE1 8HN, UK.

**Chen, G.H., Leung, D.H.W and Huang, J.C. (2001)** "Removal of dissolved organic carbon in sanitary gravity sewer." ASCE, J. of Environmental Engineering, Vol.127, No.4, 295-301.

**Crank, J. (1979)** "The mathematics of diffusion" Oxford University Press, 2<sup>nd</sup> edition first published in paper back.

**Dennis, P., Guymer, I. and Antonopoulus, C. (1999)** "Optimisation of the aggregated dead zone model for solute dispersion in surcharged manholes." 8<sup>th</sup> International conference on urban drainage, Sydney, Australia, 763-770.

**Dennis, P.M. (2000)** "Longitudinal dispersion due to surcharged manhole." PhD. Thesis, University of Sheffield, Sheffield, UK.

**DETR (1997)** "The urban wastewater treatment (England and Wales) regulations 1994." Working document for Dischargers and Legislators, A guide note issued by the Department of the Environment, Transport and the Regions and the Welsh Office.

**DoE (1994)** "The surface waters (river ecosystem) (classification) regulation." Statutory instrument, Department of the Environment.

**Escritt, L.B. (1984)** "Sewerage and sewage treatment: international practice." W.D. Haworth, eds., Wiley, Chichester, England.

**Fisher, H.B. (1966)** "Longitudinal dispersion in laboratory and natural streams." Technical report KH-R-12, W.M. Keck Laboratory of Hyd. and Wat. Resources, California Institute of Technology, Pasadena.

---

**Flo++** A CFD software developed at the Potchefstroom University for CHE, South Africa.

**Fluent (1998)** "User manual: modelling turbulent flow." Fluent Inc.

**Fluent (1999)** "Gambit user's guide." Fluent Inc.

**Foundation for Water Research (1998)** "Urban pollution management (UPM) manual: a planning guide for the management of urban wastewater discharges during wet weather." 2<sup>nd</sup> edition, ISBN: M0011147SH

**Green, M.J., Beven, K.J., Buckley, K. and Young, P.C. (1994)** "Pollution prediction with uncertainty." Mixing and transport in the environment: a memorial volume for Catherine M. Allen (1954-1991), K.J. Beven, P.C. Chatwin, and J.H. Millbank, eds., John Wiley & Sons, Chichester, England.

**Guymer, I. and O'Brien, R. (2000)** "Longitudinal dispersion due surcharged manhole." ASCE, J. of Hydraulic Engineering, 126 (2).

**Guymer, I., Dennis, P., O'Brien, R. and Saiyudthong, C. (accepted 2002)** "Diameter and surcharge effects on solute transport across surcharged manhole." ASCE, J. of Hydraulic Engineering.

**Haarhoff, J. and Walt, J.J. (2001)** "Towards optimal design parameters for around-the-end hydraulic flocculators." J. Water SRT-Aqua50, 149-160.

**Herath, S.K., Jayasurita, L.N.N. and Hussey, C.J. (1999)** "Modelling wastewater quality in sewerage systems." 8<sup>th</sup> International conference of urban drainage, Sydney, Australia, 179-186.

**Howarth, D.A. and Saul, A.J. (1984)** "Energy loss coefficient at manholes." Proc. 3<sup>rd</sup> Int. Conf. on Urban Storm Drainage, Goteborg, 127-136.

---

**Kusuda, T. and Arao, S. (1996)** "Energy losses at circular drop manholes." 7<sup>th</sup> International conference on urban drainage, Hanover, Germany, 85-90.

**Lees, M.J., Camacho, L.A. and Chapra, S. (2000)** "On the relationship of transient storage and aggregated dead zone models of longitudinal solute transport in streams." Water Resource Research, Vol.36, No.1, 213-224.

**Lindvall, G. (1984)** "Head losses at surcharged manholes with a main pipe and a 90° lateral" Proceeding of the 3<sup>rd</sup> International Conference on Urban Storm Drainage, Goteborg, Sweden, 137-146.

**Mangelson, K.A. and Watters, G.Z. (1972)** "Treatment efficiency of waste stabilization ponds." ASCE, J. of Sanit. Engin. Div., SA2, 407-425.

**Marsalek, J. (1984)** "Head losses as sewer junction manholes." ASCE, J. Hyd. Eng., Vol.110, No.8, p.p.1150-1154.

**O'Brien, R.T. (2000)** "Dispersion due to surcharged manholes." PhD. Thesis, University of Sheffield, Sheffield, UK.

**Pedersen, F.B. and Mark, O. (1990)** "Head losses in storm sewer manholes: submerged jet theory." J. Hyd. Eng., ASCE, 116(11), 1317-1328.

**Qasim, S.R. (1985)** "Wastewater treatment plants: planning, design, and operation" CBS College Publishing, New York, USA.

**Reed, E.C. (1983)** "Design and analysis of urban storm drainage: the Wallingford procedure" Hydraulics Research Limited, Howbery Park, Crowmarsh, Wallingford, Oxfordshir, Vol.1, Principles, methods and practice.

**Rutherford, J.C. (1994)** "River mixing." John Wiley and Sons Ltd, Chichester, UK.

**Saiyudthong, C. and Guymer, I. (2002)** "Effect of changes in pipe direction across manholes on dispersion." 9<sup>th</sup> International conference on urban drainage, Portland, Oregon, USA, 693-704.

**Sarker, M.A. (2000)** "Application of CFD to model local features in a river: free surface flow over broad-crested weir and modification of Crump weir for fish passage." PhD thesis, Cranfield University, UK.

**Smart, P.L. and Laidlaw, I.M.S. (1977)** "An evaluation of some fluorescent dyes for water tracing." Water resources research, vol. 13., no.1.

**Soderstrom, T. and Stoica, P. (1989)** "System identification." Prentice Hall, London.

**Sontek (1995)** "ADV software." Ver. 2.3 reference manual, USA.

**Taylor, G.I. (1953)** "Dispersion of soluble matter in solvent flowing slowly through a tube." Proc. R. Soc. London Ser. A, 219, 186-203.

**Taylor, G.I. (1954)** "The dispersion of matter in turbulent flow through a pipe." Proc. R. Soc. London Ser. A, 223, 446-468.

**Versteeg, H.K. and Malalasekera, W. (1995)** "An introduction to computational fluid dynamics: the finite volume method." Longman Scientific and Technical, John Wiley & Sons, England.

**Wallis, S.G. (1994)** "Simulation of solute transport in open channel flow." Mixing and transport in the environment: a memorial volume for Catherine M. Allen (1954-1991), K.J. Beven, P.C. Chatwin, and J.H. Millbank, eds., John Wiley & Sons, Chichester, England, 89-111.

**Wallis, S.G., Guymer, I. and Bilgi, A. (1989)** "A practical engineering approach to modelling longitudinal dispersion." Proceeding of international conference on hydraulic

---

and environmental modelling of coastal, estuarine and river waters, Bradford, England, 19-21 September, 291-300.

**Wood, M.G., Howes, T., Keller, J. and Johns, M.R. (1998)** "Two dimensional computational fluid dynamic models for waste stabilization ponds." *Wat. Res.*, Vol.32, No.3, 958-963.

**Young, P., Jakeman, A. and McMurtrie, R. (1980)** "An instrumental variable method for model order identification." *Automatica*, Vol.16, 281-294.

**Young, G.K., Stein, S.M., Pearson, D.R. and Atayee, A.T. (1999)** "User's manual for HYDRAIN: integrated drainage design computer system" GK Y and Associates, Inc., 5411-E Backlick Rd, Springfield, Virginia, USA, Vol.3, Hydra-Storm drains.

**Young, P.C. (2002)** "Data-based mechanistic and top-down modelling." *The international environmental modelling and software society (iEMSs)*, Vol.1, Lugano.

**Young, P.C. and Lees, M. (1993)** "The active mixing volume: a new concept in modelling environmental systems." *Statistics for the environment*, V. Barnett, and K.F. Turkman, eds., John Wiley & Sons, Chichester, England, 3 – 43.